Critical Current in Ferromagnet/Superconductor Hybrid Structures

Dissertation
zur Erlangung des Doktorgrades der Naturwissenschaften
(Dr. rer. nat.)
der naturwissenschaftlichen Fakultät II – Physik
der Universität Regensburg

vorgelegt von
Wilfried Meindl
aus Dingolfing

Oktober 2007

Die Arbeit wurde von Prof. Dr. Ch. Strunk angeleitet.
Das Promotionsgesuch wurde am 22. Oktober 2007 eingereicht.
Das Kolloquium fand am 25. Januar 2008 statt.

Prüfungsausschuss:	Vorsitzende:	Prof. Dr. M. Grifoni
	1. Gutachter:	Prof. Dr. Ch. Strunk
	2. Gutachter:	Prof. Dr. Ch. Back
	weiterer Prüfer:	Prof. Dr. J. Zweck

Contents

Introduction

Superconductivity and ferromagnetism are usually regarded as contrary phenomena. This is surely true for singlet superconductivity, where electrons with opposite spins combine to form Cooper pairs. But other forms of superconductivity are suspected to exist and partly experimental facts have been discovered, which affirm this conjecture.

One prominent alternate form is triplet superconductivity. Here the pairs consist of electrons with equal spin. Keizer et al. [KGK$^+$06] observed triplet supercurrent in a Josephson junction consisting of the superconductor NbTiN and the halfmetallic strong ferromagnet CrO_2. Due to the nature of the ferromagnet to align spins parallel, only the triplet component can survive in this material. The proximity effect responsible for the "'leakage" of superconductivity into non superconducting areas was observed to have a much longer range for the triplet than for the singlet component as was predicted by Bergeret et al. [BVE01][BVE02][BVE05]. In fact, the length scale over which this supercurrent can penetrate into the ferromagnet should be comparable to the one in normal metals.

Diluted ferromagnets, like PdFe, which is the subject of interest in this work, allow the coexistence of ferromagnetism and singlet superconductivity over a much longer distance than strong ferromagnets. Their tendency to break singlet pairs is considerably weaker. Diluted ferromagnets were already successfully applied in experiments involving π Josephson junctions [KAL$^+$02][Kon02][GAB$^+$03]. The phase change of the superconducting condensate which emerges over the ferromagnet can be used to induce a spontaneous current in a SQUID structure, which then traps *half* a flux quantum.

Long range effects involving spin polarized currents and spin imbalance should be observable. First experiments to create magnetic currents in ferromagnet/paramagnet systems were performed by Johnson and Silsbee in 1985 [JS85]. The spinpolarized current was injected at a ferromagnet/paramagnet interface, the polarizer, and then detected at a distance away with a spin analyzer. Already in 1971 it was discovered by Tedrov and Meservey that the tunneling current at a ferromagnet/superconductor interface is spin polarized [TM71][TM73][MT94]. The injection of a spin polarized current in a niobium film was observed by Johnson in 1994.

All those former investigations show that a rich field of physics is opened by combining superconductivity with ferromagnetism, which this work addresses. On hybrid structures of niobium and an alloy of palladium with iron, magnetoresistance measurements were performed, which were further refined by observing the differential resistance in varying magnetic fields. The initial magnetoresistance oscillations produced a rich pattern in the differential resistance plots. A step towards the interpretation of these results was done by modifying the flux through the sample and by probing different contact configurations.

The matter of this work is presented as follows in two parts. The first part covers the diluted ferromagnet $Pd_{1-x}Fe_x$. In chapter 1, the foundations of ferromagnetism as it appears in $Pd_{1-x}Fe_x$ is presented. The preparation and the characterization of the diluted ferromagnetic films by anomalous Hall effect and SQUID measurements is described in chapter 2. Then, in part II, the foundations of superconductivity and its related phenomena are given. Chapter 4 is devoted to the sample preparation by the PES technique. Also the measurement setups for magnetoresistance and differential resistance are sketched here. In the large chapter 5, the results of the mesurements on the hybrid superconductor/ferromagnet structures are presented. Starting with the magnetoresistance oscillations, it then moves on to the differential resistance patterns and closes with the investigation of different contact configurations and the experiments on flux variation. Chapter 6 sheds some light on the results of chapter 5 by connecting them and giving an interpretation of some aspects. The findings are further affirmed by control experiments described in chapter 7. Chapter 8 gives an overview of the results and discusses possible future investigations on this matter.

Part I

Diluted Ferromagnets

1 Ferromagnetism

Superconductivity and ferromagnetism are antagonistic phenomena. While superconductivity tends to align the spins of electrons in a Cooper pair opposite to each other, ferromagnetism favors a parallel alignment of magnetic moments implicating equally oriented spins. Both these different effects are generated by interactions between the electrons. On the one hand, a weak attractive force mediated by phonons acts in a superconductor, on the other hand, the exchange interaction is responsible for ferromagnetism to appear.

In this chapter the basics of ferromagnetic materials will be presented. Beginning with theoretical aspects of ferromagnets, we will pass on to dilute ferromagnetism in palladium-iron alloys, which were chosen for the experiments in this work. Compared to strong ferromagnets, their ability to break Cooper pairs is weaker, as the exchange energy, which rules the magnetic behavior, is smaller. This characteristic energy is linked to the Curie temperature in the Curie-Weiss model of ferromagnetism. As the exchange energy diminishes, also the Curie temperature sinks. For certain alloys, it may even lie in the range of superconducting transition temperatures, making it eventually possible to simultaneously bring the energy gap in superconductors and the exchange energy characteristic of ferromagnets to a comparable magnitude. Thus a competition between both energies is established, resulting in interesting effects.

1.1 Magnetic Moments

All magnetic phenomena are associated with magnetic moments. These magnetic moments can either act more or less independently from each other, which results in paramagnetism and diamagnetism, or their actions are linked like, in ferro- and antiferromagnetism considered in this section. The ideas presented here and in the following sections are taken mainly from [Lév00], [Blu01] and [AM76].

In classical magnetostatics magnetic fields arise because of macroscopically circulating charge currents. In quantum mechanics the magnetic moments are associated solely with angular momenta, like the spins of electrons, nuclei, whole atoms and ions. Also uncharged particles may possess a magnetic dipole moment, e. g. the neutron with spin 1/2.

As is shown by quantum mechanics, the spatial components of a spin s can only take on the $2s + 1$ values $m_s\hbar$ with $m_s = -s, -s + 1, \ldots, s - 1, s$. As an example, we will look at the electron, for which $s = 1/2$. So the only possible values along a chosen axis are $m_s = \pm 1/2$ designated as "spin up" or $|\uparrow\rangle$ for the positive and "spin down" or $|\downarrow\rangle$ for the negative sign. The magnetic moment connected with the spin has components

$-g\mu_B m_s$ along a spatial axis and a magnitude of $\sqrt{s(s+1)}\mu_B m_s$. g, the *Landé factor* or simply *g-factor*, is a dimensionless constant amounting to 2 for electrons. The quantum mechanical unit of magnetic moment is the *Bohr magneton* $\mu_B = e\hbar/2m_e$. Due to its negative charge $-e$ the magnetic moment of an electron is always antiparallel to its spin.

1.2 Magnetostatics

The magnetization $\mathbf{M}$ is defined as magnetic moments per unit volume. It is the mean of all the microscopic magnetic moments in a solid and therefore a macroscopically measurable quantity. Together with the magnetic field $\mathbf{H}$ caused by macroscopically flowing currents, it describes the *magnetic induction*

$$\mathbf{B} = \mu_0(\mathbf{H} + \mathbf{M})\,. \tag{1.1}$$

The magnetic moments react to an external field $\mathbf{H}$. Thus, in the case of linear media, the magnetization will change according to the formula

$$\mathbf{M} = \chi\mathbf{H}\,. \tag{1.2}$$

χ is the dimensionless *magnetic susceptibility*, characterizing the response of the magnetization to an external field. Now we can write

$$\mathbf{B} = \mu_0(\mathbf{H} + \chi\mathbf{H}) = \mu_0\mu_r\mathbf{H}\,, \tag{1.3}$$

where $\mu_r = 1 + \chi$ is the *relative permeability*. In the general case, eq. (1.2) and eq. (1.3) are not valid. This is especially true if hysteresis and spontaneous magnetization play a role, like in ferromagnetic materials.

1.3 Exchange

The interaction of the magnetic dipole moments in a solid is much too weak to result in ferromagnetic ordering. This may be shown by the estimation of its energy $\mu_0\mu_B^2/a_0^2 \approx 1\,\mathrm{K}$, where μ_0 is the vacuum permeability, the Bohr magneton μ_B stands for the magnetic moment of one dipole and a_B is the Bohr radius, is approximately one atomic distance. Ferromagnetism, however, can be observed up to temperatures of more than 1000 K, e. g. 1093 K for iron and 1428 K for cobalt. An electrostatic interaction called *exchange* is the mechanism by which the spins in a material get aligned.

Just consider a system of two electrons. Being fermions, they obey the Pauli principle: two identical fermions may not occupy the same quantum mechanical state simultaneously. In consequence, this means for our system of electrons that the combined wave function must be antisymmetric. As it is the product of a spatial and a spin part, there are two possibilities. First, the spatial part is symmetric and the spin function is antisymmetric, which means that the two spins are aligned antiparallel. Second, the spatial part is antisymmetric, which then requires a symmetric spin part, i. e. parallel spins.

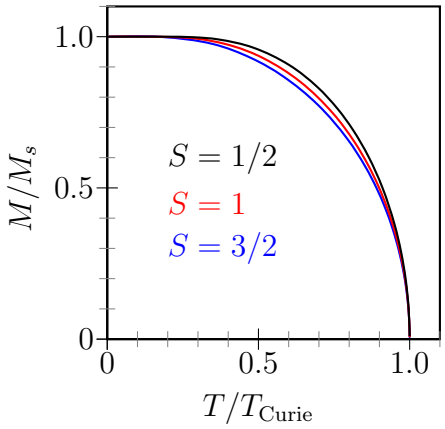

Figure 1.1: *Magnetization depending on temperature as derived in the Weiss model of ferromagnetism for a ferromagnetic system of particles with spin* 1/2 *(upper curve), spin* 1 *(middle curve) and spin* 3/2 *(lower curve).*

The *exchange energy* is the energy difference between the states characterized by parallel and antiparallel spin orientation. Still, this is an electrostatic effect and not based on the interaction of the magnetic moments associated with the spins. The relative distances at which the electrons are found are different for the symmetric and asymmetric spatial parts of the wave function. Taking into account the distance dependent repulsion of the electrons, the two states must have different energies.

The generalization of this two electron model to many electrons was accomplished in the *Heisenberg model* with the Hamiltonian

$$\hat{\mathcal{H}} = -2 \sum_{i>j} J_{ij} \hat{\mathbf{S}}_i \hat{\mathbf{S}}_j \,. \tag{1.4}$$

Here the sum of the exchange energy J_{ij} of all the possible electron pairings is built, the operator $\hat{\mathbf{S}}_i$ represents the spin orientation of a single electron.

The Heisenberg model can be used in many cases, although the exchange mechanism may be different in detail, just to mention itinerant exchange or the RKKY interaction [RK54][Kas56][Yos57] belonging to the ample field of indirect exchange in contrast to direct exchange described here.

1.4 Weiss Model

In ferromagnets the exchange energy leads to a spontaneous alignment of the magnetic moments in the same direction. A spin feels the exchange caused by all the other surrounding spins. This can be expressed as an internal magnetic field, which is called the *molecular field*.

With this approximation the, ferromagnet can be seen as a paramagnet, where the magnetic moments do not undergo exchange interaction. Exchange is embraced by adding to an external field $\mathbf{B}$ an additional internal field $\mathbf{B}_{\text{mf}}$. As the molecular field is

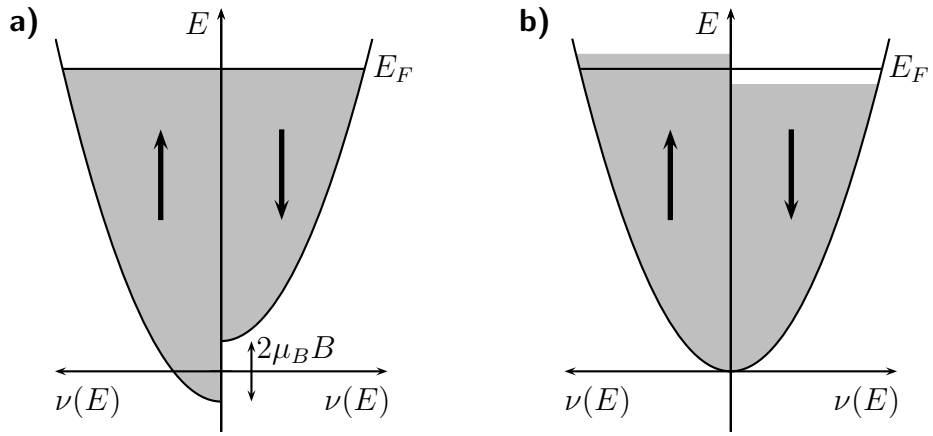

Figure 1.2: *a) Spin split bands of a free electron gas in a magnetic field B. b) Spontaneous splitting of energy bands in a metal.*

proportional to the magnetization of the material, which is a macroscopic quantity, one arrives now at a macroscopic view. This is the *Weiss model of ferromagnetism.*

Within this theory, the dependence of magnetization on temperature can be explained, as displayed in fig. 1.1. The magnetization $\mathbf{M}_s$ at 0 K is the saturation value. If the temperature increases, thermal fluctuations start to decrease the magnetization by misaligning the magnetic moments. At the *Curie temperature* T_{Curie} and higher, no net magnetization of the material will be observable.

1.5 Magnetism In Palladium

Pure palladium is not ferromagnetic. But it has a remarkable property: a greatly enhanced magnetic susceptibility. Together with platinum, palladium is considered almost ferromagnetic. This means, that a small change of its electronic structure, for instance by adding ferromagnetic impurities, suffices to produce a ferromagnet. So both metals almost fulfill the *Stoner criterion* for ferromagnetism, which will be explained in the following.

1.5.1 Itinerant Magnetism And Stoner Enhancement

As an approximation, the conduction electrons in a metal may be treated as a free electron gas. The density of states $\nu(E)$ for a three dimensional system is then proportional to $\sqrt{E}$. This situation is depicted in fig. 1.2a. If a magnetic field B is applied, then the density of states for spin-up electrons and for spin-down electrons will be split by twice the *Zeeman energy* $g\mu_B m_s B$. With $m_s = 1/2$ and $g = 2$ the total energy difference is $2\mu_B B$. The number of electrons at the Fermi level with spin up is $n_\uparrow$ and $n_\downarrow$ for spin down. In the case of different occupation numbers for the spin orientations, a nonzero magnetization $M = \mu_B(n_\uparrow - n_\downarrow)$ will appear. The response strength of this system to an external field is measured by the *Pauli susceptibility* χ_P.

The Stoner criterion for the spontaneous splitting of the energy bands is based on the competition of the Zeeman energy and the kinetic energy. As can be seen in fig. 1.2b, the energy of the system is increased by flipping the spins of some electrons from down to up, which then only can occupy a state lying higher in kinetic energy than before. On the other hand, if the spin's magnetic moment is now oriented parallel to the molecular field, then the energy is decreased by the Zeeman term $\mu_B \mathbf{B}_{\mathrm{mf}} = \mu_B \lambda \mathbf{M}$. The *Stoner criterion*

$$I\nu(E_F) \geq 1\,, \tag{1.5}$$

determines, if the energy increase by the kinetic energy or the decrease by the Zeeman term dominates [Sto38]. $I = \mu_0 \mu_B^2 \lambda$ is a measure of the exchange interaction causing the molecular field. This condition can be satisfied by a very large density of states $\nu(E_F)$ at the Fermi level or by a large molecular field. Palladium just does not satisfy eq. (1.5) although $\nu(E_F)$ is very large. The susceptibility nevertheless is increased to

$$\chi = \frac{\chi_P}{1 - I\nu(E_F)}\,. \tag{1.6}$$

This effect is called *Stoner enhancement* and the expression $(1 - I\nu(E_F))^{-1}$ the *Stoner factor*.

1.5.2 Alloys Of Palladium With Ferromagnetic Materials

For palladium, the Stoner factor is 10 as obtained from a comparison of band structure calculations with susceptibility measurements [Nie75]. Therefore the magnetic moments in palladium can be very easily polarized. A magnetic impurity like e. g. an iron atom will surround itself with a cloud of magnetic moments in the palladium matrix. This results in an increase of the magnetic moment per iron atom from $2.2\mu_B$ in bulk iron to approximately $10\mu_B$ if it is dissolved in palladium. A spin of $S \approx 2$ can be allotted to these polarization clusters. Depending on the distance between the impurity atoms the polarization clouds may overlap, leading to an indirect interaction of the distant magnetic moments at the impurity sites [Nie75]. Ferromagnetic ordering is then said to be established by *localized* magnetic moments, as they have a fixed position at the iron atoms.

A second model assumes the *itinerant* picture of the preceding section [Kim66]. Because of the high Stoner factor, palladium is on the verge of ferromagnetism. The presence of impurities may suffice to shift the balance between kinetic and Zeeman energy in such a way that the conduction band gets ferromagnetic. This would imply that the ordering of the magnetic moments of the impurities does not play a crucial role. In general, a mixture of both models is to be expected, which in the case of alloys also depends on the concentrations of their constituents.

2 Preparation And Characterization Of Palladium-Iron

We have seen that the exchange energy plays a crucial role for many of the magnetic properties. In section 3.3, the proximity effect will be introduced for normal metals and ferromagnets. In the magnetic case, another characteristic quantity, the energy gap of a superconductor is set into concurrency with the exchange energy. Their mutual strength determines the interplay of ferromagnetism and superconductivity, as on the one hand, the exchange energy tends to break superconductivity, and, on the other hand, superconductivity may penetrate into a ferromagnet.

There is the possibility of altering the exchange energy of palladium-iron by adjusting the iron concentration, so that the properties of such a combined system may be controlled. In this chapter the production and characterization of the diluted ferromagnet are presented.

2.1 Anomalous Hall Effect

It has been observed that many ferromagnetic materials show a Hall voltage even if no magnetic field is applied. As one might suppose, the magnetization of the sample causes this *anomalous* component of the Hall voltage, which adds to the normal Hall effect. This offers the possibility of examining the magnetic behavior of thin films and at the same time their electrical parameters may be measured.

2.1.1 Skew Scattering And Side Jump

The total Hall resistivity of a ferromagnetic sample can be written

$$\rho_{xy} = A_0 B_z + \mu_0 A_S M_z \,. \tag{2.1}$$

A_0 is the normal Hall coefficient and A_S characterizes the anomalous Hall effect. B_z and M_z are the magnetic field and the magnetization of the sample perpendicular to the sample plane, respectively.

To describe the emergence of the anomalous Hall component, a microscopic theory has been developed in which spin orbit coupling leads to a spin dependent scattering of electrons at impurities. This is described by two processes shown in fig. 2.1. In this pictures introduced by Smit and Berger [Smi55][Smi58][Ber70], the electron with a certain spin direction scatters at a central potential at the location of an impurity. Spin orbit coupling is responsible for the probabilities of scattering to the left and to the right

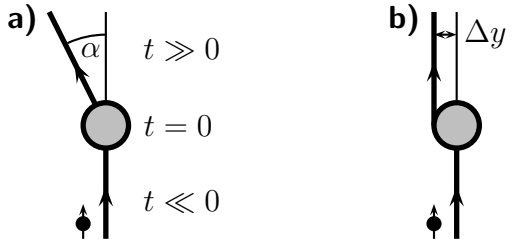

Figure 2.1: *Scattering processes in the anomalous Hall effect of an electron at a central potential in the presence of spin-orbit coupling. a) Skew scattering. The probability that the electron is scattered on one side is bigger than for scattering on the other one, depending on its spin. b) Side jump. The trajectory of the electron is shifted by a distance of typically* $\Delta y \approx 10^{-10}$.

not being equal, as they depend on the spin direction of the electron. Therefore, the wave packet of an electron changes its direction, giving rise to the so called *skew scattering*. The scattering potential may also lead to a displacement of the wave function. This is called *side jump* effect. Both processes depend on the concentration of impurities in the metal and therefore on its longitudinal resistance R. In general, the anomalous component of the Hall resistance R_H can be written as

$$R_A = \alpha R + \beta R^2 \tag{2.2}$$

with some constants α and β, where the term linear in R is caused by skew scattering and the quadratic term comes from side jump [CW80].

2.1.2 Samples And Measurement

A typical sample is shown in fig. 2.2a. The Hall structure is formed by optical lithography and lift-off technique. Four contacts at the side of the current path allow the measurement of the longitudinal voltage V and the transverse Hall voltage V_H. The thin $Pd_{1-x}Fe_x$ film is evaporated on top of an oxidized p-doped monocrystalline silicon substrate. The thickness of the insulating oxide layer was 300 nm. Typical film thicknesses of the deposited layers were 20 nm and 15 nm. Thinner layers result in higher Hall voltages corresponding to $R_H = \rho_{xy}/d$ for the Hall resistance derived from (2.1), where d is the thickness of the metal film. On the other hand, the magnetic properties may change with d as has been demonstrated for $Pd_{1-x}Fe_x$ by Schöck in [SSvL00]. Therefore mostly a layer thickness of 20 nm was chosen which yielded a good Hall signal and which was used in experiments with superconductor/ferromagnet heterostructures.

The alloy was produced by evaporating palladium and iron from separate home built effusion cells in an ultra high vacuum system (base pressure $5 \cdot 10^{-11}$ mbar). The relation between the ratio of the deposition rates of palladium and iron, r_{Pd} and r_{Fe}, and the atomic iron concentration x in the film is given by the formula

$$\frac{r_{Pd}}{r_{Fe}} = \frac{1}{C}\left(\frac{1}{x} - 1\right) \quad \text{with} \quad C = \frac{\rho_{Pd}}{\rho_{Fe}}\frac{M_{Fe}}{M_{Pd}} = 0.8444\,. \tag{2.3}$$

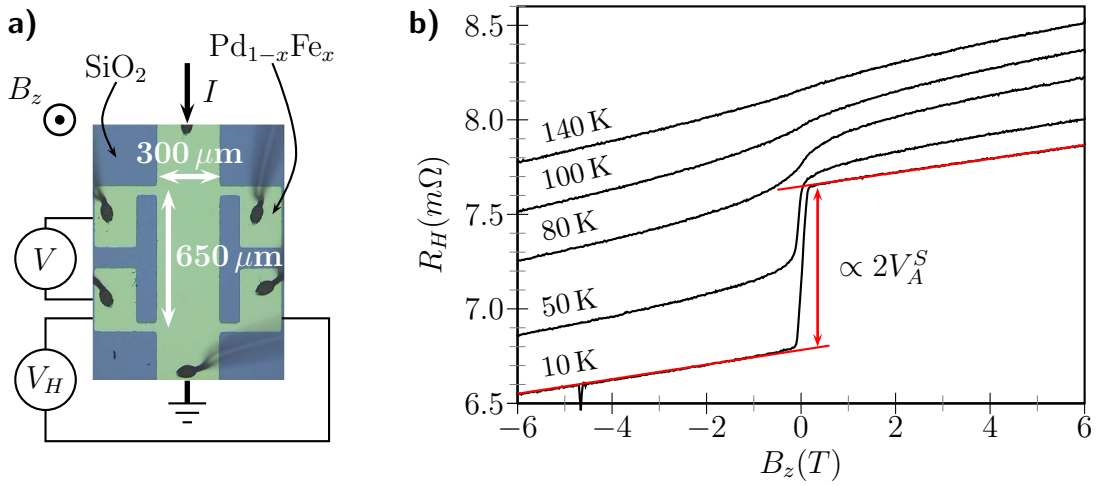

Figure 2.2: *a) Sample for determining the magnetic and electrical properties by the measurement of the transverse Hall voltage V_H and the longitudinal voltage V. The picture was taken in an optical microscope. b) Typical measurement of the Hall resistance. The iron concentration of the $Pd_{1-x}Fe_x$ film is $x = 2.5$ %. The contribution of the anomalous Hall effect to the Hall voltage and hence a measure of the magnetization of the sample can be determined from the jump around 0 T indicated by the arrow. The normal Hall coefficient is given by the slope of the curves at high fields.*

ρ_{Pd} and ρ_{Fe} are the densities and M_{Pd} and M_{Fe} the atomic masses of both elements. So for an iron concentration of 5 %, the ratio is $r_{Pd}/r_{Fe} = 22.5$. Auger spectroscopy on a nominal 7 % sample showed that the real iron concentration was 7.8 % and thus confirm our determination of the deposition rates within error limits which will be discussed together with the results of the Hall measurements. The Auger measurements were carried out by Dr. Johann Vancea at the University of Regensburg.

The samples were then cooled down in a ^{4}He cryostat with a variable temperature insert and a magnet system capable of generating a field up to 12 T. Both the longitudinal voltage V and the Hall voltage V_H in dependence of magnetic field were recorded for various temperatures using lock-in technique.

For a thin film of 20 nm of $Pd_{97.5}Fe_{2.5}$ typical Hall curves are shown in fig. 2.2b. The jump around 0 T in the Hall resistance is due to the anomalous Hall effect displaying the magnetization change in the thin film while sweeping the field applied perpendicular to the sample plane.

The Hall curves in 2.2b exhibit an offset which grows with temperature. They normally should lie point symmetrically about zero magnetic field and zero resistance. A slight misalignment of the Hall contacts leads to the contribution of a longitudinal component to the transverse voltage V_H which includes both the normal and the anomalous Hall voltage. The longitudinal voltage V typically is three orders of magnitude higher than V_H.

At high positive and negative magnetic fields the V_H–I curves become straight lines. Their slope corresponds to the normal Hall coefficient. Straight lines fitted to the graph

in these ranges are extrapolated to zero magnetic field. At that point, the gap between them is twice the contribution of the anomalous Hall effect to the Hall voltage V_H. This voltage is the value at the saturation of magnetization and is designated with V_A^S, c. f. eq. (2.1). By this procedure the unwanted contribution of the longitudinal voltage to V_H drops out. Following eq. (2.2), a quantity proportional to the saturation magnetization can be derived from V_A^S or the corresponding resistance R_A^S, respectively. For pure skew scattering it is R_A/R and for pure side shift R_A/R^2. This value plotted against temperature displays the behavior of the magnetization. As depicted in fig. 2.4 the form is indeed similar to the temperature dependence predicted in the Weiss model. From these graphs the Curie temperatures can be determined.

An Arrot plot of the Hall curves would provide another method of finding the Curie temperature. It consists of plotting $(R_A/R^a)^2$ against $B/(R_A/R^a)$ for various temperatures and finding the straight line crossing the origin. The temperature associated with that line is the Curie temperature. This approach, which is described in e. g. [Ohn98], requires to eliminate from the data shown in fig. 2.2 both the offset stemming from the contribution of the longitudinal voltage and the contribution of the normal Hall effect in order to obtain $R_A(B)$. The method is not applicable here because it requires the exponent a, which is related to the scattering process, to be known rather exactly.

For PdNi, which is quite similar to PdFe, it has been found that skew scattering is the dominating contribution at low nickel concentrations up to 8 %. The theory of skew scattering assumes localized magnetic impurities. For PdNi alloys with a higher nickel content than 8 % and for all PdFe alloys this is not true, as band ferromagnetism dominates here [CW80].

2.1.3 Results And Discussion

The graphs of the anomalous Hall component in fig. 2.3 were measured with the help of Thorsten Schmidt who did this as a scientific project during his studies at the University of Regensburg. To be able to compare the behavior for different concentrations and layer thicknesses better, the anomalous Hall voltages were normalized to their maximum value.

The iron concentrations range from 1.9 % to 10 %. We put more emphasis on the lower concentrations as we tried initially to keep the Curie temperature as low as possible. During evaporation of the $Pd_{1-x}Fe_x$ films both the iron rate and the palladium rate have to be controlled. This is possible up to an estimated error of 1 % of iron content.

The curves in fig. 2.3 show the progression of the anomalous hall voltage with iron concentration. At 10 % the magnetization must persist almost up to room temperature, whereas it decreases much faster for concentrations below 5 %. This corresponds to the behavior described in [Nie75], where for the concentration domain between 1.7 % and 5.11 % Curie temperatures between 85 K and 160 K are quoted.

To confirm this further, a quantity proportional to magnetization has to be found. As skew scattering can be ruled out as the dominating cause for the anomalous Hall effect in $Pd_{1-x}Fe_x$, see [CW80], $V_A(T)/V(T)^2$ was assumed to be the correct term, which is plotted in 2.4. A comparison with fig. 1.1 shows that the curves with an iron concentration of more than 2 % have nearly the same characteristics as predicted by the

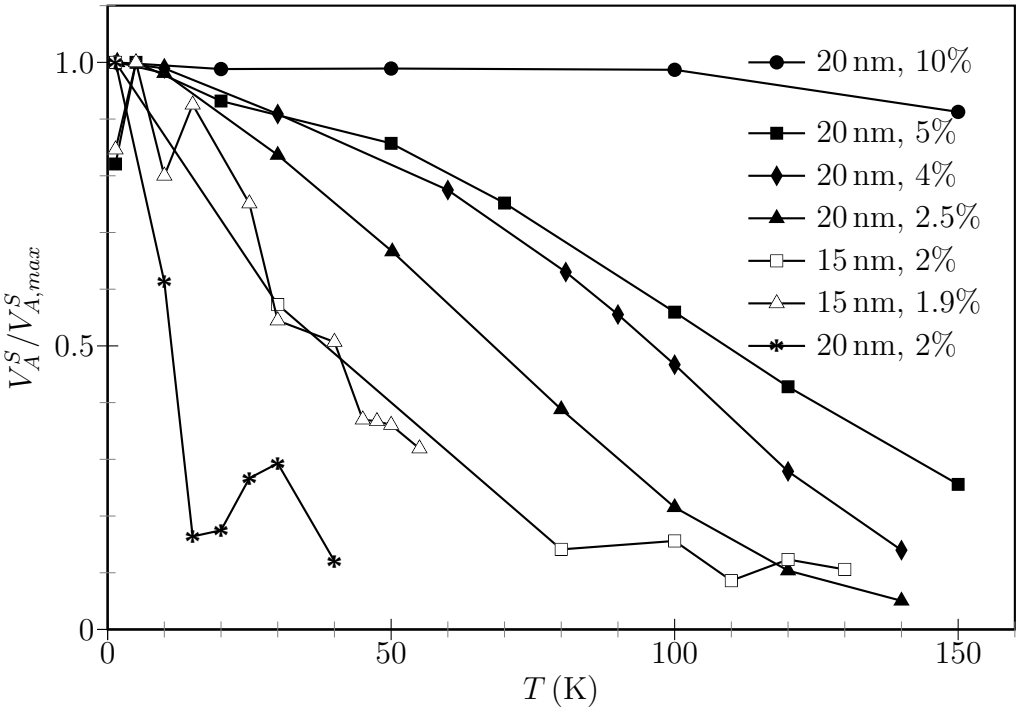

Figure 2.3: *Saturation value of the anomalous Hall voltage normalized to its maximum values for various iron concentrations and thicknesses of* 20 *nm and* 15 *nm.*

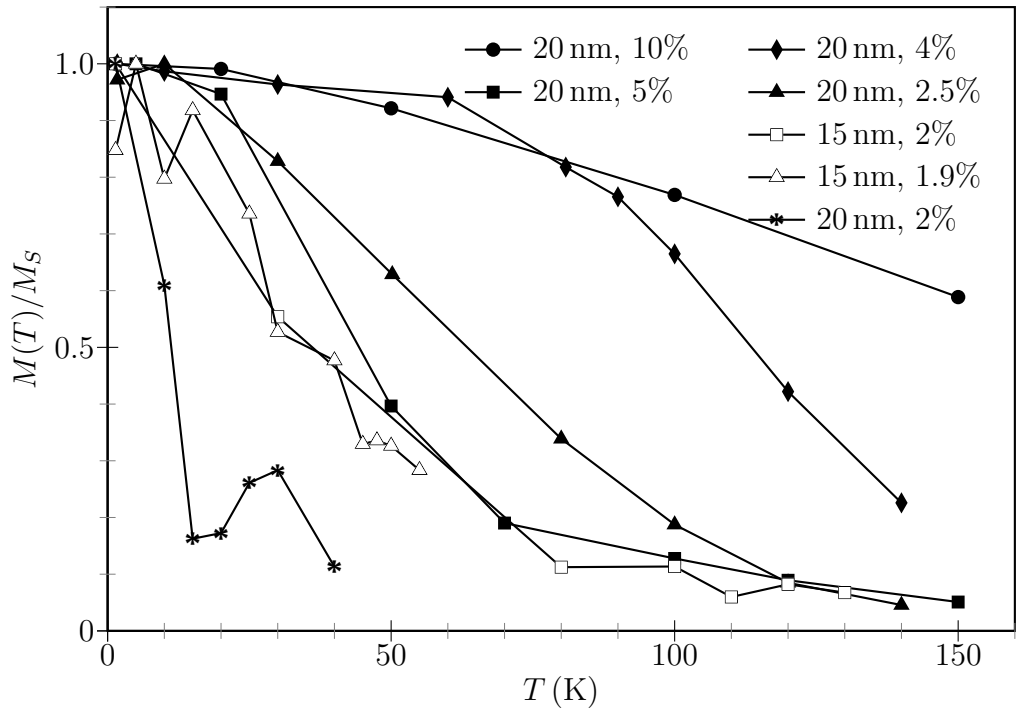

Figure 2.4: *Magnetization of the $Pd_{1-x}Fe_x$ films. The graphs are normalized to the saturation values at low temperatures. $M(T)$ was determined by assuming side jump. The legend displays the layer thicknesses and the iron concentrations of the films.*

iron concentration at. %	layer thickness nm	Curie temperature K	normal Hall coefficient $10^{-11}\,\mathrm{m}^3/\mathrm{As}$	square resistance Ω
1.9	15	80	0.80	13.9
2.0	15	95	0.85	12.4
2.0	20	17	0.70	9.7
2.5	20	115	4.56	24.7
4.0	20	155	9.30	10.4
5.0	20	185	10.3	14.3
10.0	20	315	13.1	21.6

Table 2.1: *Summarizing table of Curie temperatures, normal Hall constants and square resistances determined from Hall effect measurements.*

Weiss model of ferromagnetism. The magnetization curve asymptotically approaches the saturation value at low temperatures. For low concentrations this feature is missing or at least only very weakly developed.The big temperature steps might be responsible for this plateau not being visible. However, ferromagnetic ordering persists down to an iron concentration of 0.01 % according to [BAS+92]. The non vanishing tail at higher temperatures is ascribed to the generally smooth ferromagnetic transition in diluted ferromagnets [Nie75] and to inhomogeneities within the films.

The Curie temperature is determined from fig. 2.4 by elongating the tangents at the inflexion points to the abscissa where the magnetization is zero. At this crossing point the Curie temperature is found. Table 2.1 gives an overview. The value for 2.0 % and 20 nm deviates strongly from the general trend. This is ascribed to a deteriorated bond contact during the measurement. T_{Curie} for 5.0 % and 20 nm was obtained using the same method for the curve in fig. 2.3 for the anomalous Hall voltage.

The graphical representation of the Curie temperature depending on concentration is shown in fig. 2.5a. The data for 20 nm can be fitted to a straight line $T_{\mathrm{Curie}}(x) = a + bx$ with $a = 49.4\,\mathrm{K}$ and $b = 26.6\,\mathrm{K/at.\,\%}$. In [Nie75] it is stated that for low concentrations T_{Curie} is proportional to the square of the iron concentration x^2, whilst for higher values the proportionality is direct. So in $Pd_{1-x}Fe_x$ with 2 % of iron the alloy is already in the linear regime.

T. Kontos [Kon02] found a linear dependence between Curie temperature and film thickness for $Pd_{1-x}Ni_x$. In contrast, measurements by Monika Kitzinger on $Pd_{93}Fe_7$ [Kit07] showed that for this material the dependence between the thickness d and the Curie temperature T_{Curie} is given by

$$T_{\mathrm{Curie}}(d) = T_{\mathrm{Curie}}(\infty)\left(1 - \frac{\xi_0}{d}\right), \tag{2.4}$$

where $T_{Curie}(\infty) = (180.6 \pm 11.0)\,\mathrm{K}$ and the correlation length $\xi_0 = (2.7 \pm 0.41)\,\mathrm{K}$. Accordingly, the Curie temperatures of the 15 nm samples lie below the fit line of the 20 nm data points in fig. 2.5. An estimation of the Curie temperature by eq. (2.4) amounts to a reduction of around 5 %.

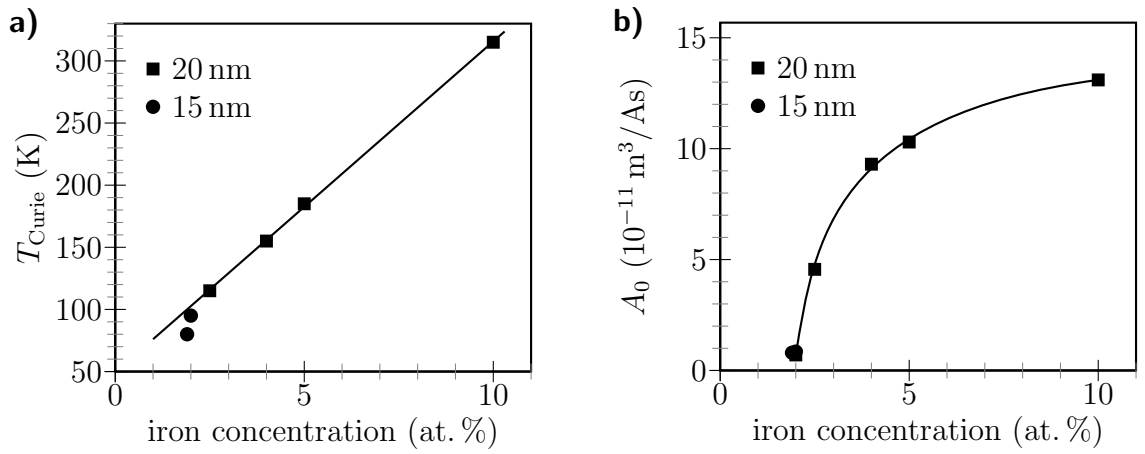

Figure 2.5: *a) Curie temperature of $Pd_{1-x}Fe_x$ films depending on the iron concentration. The straight line is a linear fit to the data for* 20 *nm. The Curie temperature of the* 15 *nm data was not taken into account for the fit. b) Normal Hall coefficient. The continuous line serves as a guide to the eye.*

Table 2.1 and fig. 2.5b also contain the normal Hall constant A_0. It changes considerably in the range of iron concentrations given by the samples. For pure palladium and layer thicknesses greater than 13 nm the Hall constant is negative [PLP69]. For bulk $Pd_{1-x}Fe_x$ the value of the Hall constant was found to be around $-7 \times 10^{-11}\,\mathrm{m}^3/\mathrm{As}$ in the concentration and temperature ranges also considered here [Pla66]. Following the results of the measurements, the iron content effects a positive Hall constant in $Pd_{1-x}Fe_x$ thin films also for thicknesses of 15 nm and 20 nm.

The square resistances given also in tab. 2.1 were determined from the average of the longitudinal resistance of one magnetic sweep. All values were obtained at 1.4 K or 1.7 K.

2.2 SQUID

As a comparison and to affirm the values obtained by the anomalous Hall effect a few samples were also measured in a SQUID. They were done by Matthias Sperl at the group of Prof. Dr. Günther Bayreuther for magnetism and magnetoelectronics at the University of Regensburg. Fig. 2.6 shows the measurements performed on two $Pd_{1-x}Fe_x$ films. As the layer thicknesses and iron concentrations nominally were the same it is surprising to find such a big deviation between the Curie temperatures in fig. 2.6a. But as can be seen in fig. 2.5, it depends linearly on the iron concentration with a proportionality factor of 26 K/at. % iron content. The difference between the two curves in fig. 2.6 confirms the conjecture that in this range the constitution of the alloy during evaporation can be ascertained only up to 1 % of iron content.

Fig. 2.6 shows a typical hysteresis curve for a continuous film (sample 1). The magnetic field was applied in plane. This figure only shows a cut-out of the measurement. The magnetic field was driven up to plus and minus one Tesla, i. e. to a point far out in the

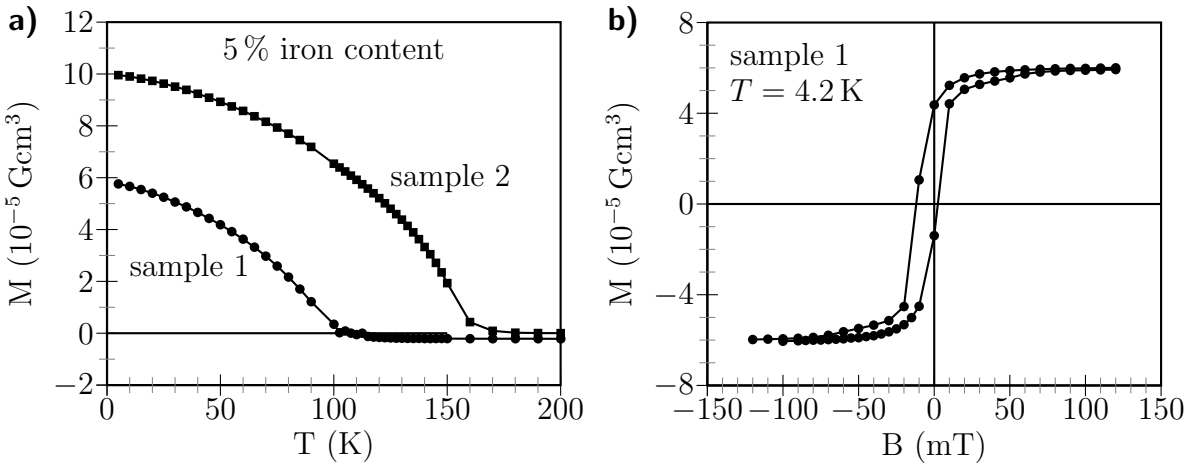

Figure 2.6: *Squid measurements of two* 20 *nm* $Pd_{1-x}Fe_x$ *continuous films with* 5 *% iron content. a) Measurement of the temperature dependent magnetization for both samples. b) Hysteretic behavior of sample 1*

saturation regime of magnetization. The hysteretic switching of magnetization takes place at fields of ±10 mT.

Part II

Niobium/Palladium-Iron Hybrid Structures

3 Foundations

In this chapter, the theoretical basics used for the setup of the experiments on superconductor-ferromagnet hybrid structures and the discussion of their results is given. An introduction to superconductivity and to some effects related to it can naturally be only quite shallow in the frame of this writing. The reader can find more information in the references given herein.

After a short overview over BCS and Ginzburg-Landau theory, the proximity effect governing the spread of superconductivity in non-superconducting material is treated. Then the Josephson effect is introduced, which is followed by a survey of macroscopic quantum interference effects, which can be observed in the field of superconductivity. In the nonlocal measurement setup, which is used in the experimental part, charge imbalance effects can be observed, which are presented in the last section of this chapter.

3.1 Superconductivity

The metals in the periodic table can be divided into two kinds: the ones which get superconducting at low temperatures, the so called *conventional superconductors* and the ones, who are said to stay *normal*. Close to a temperature of 0 K, the electron states of a normal metal are occupied up to a certain limiting energy, which is called the *Fermi energy* E_F. This *normal* ground state of the electron sea is unstable against an attractive force between the electrons. The electrons pair up, driving the system into a new ground state with lower energy. This was shown by Cooper in 1956 [Coo56].

The collective wave function of such a pair must be antisymmetric, as has been pointed out already in section 1.3, allowing the combination of electrons of opposite spin if the spatial part is symmetric *(singlet superconductivity)* or of parallel spin *(triplet superconductivity)* for an asymmetric spatial part. In many superconducting systems, Cooper pairs with antiparallel electron spins are preferred. The pairing of electron spins results in an integral spin, which makes the Cooper pairs bosons. As the Pauli principle is not effective for them, they can all occupy a single state, called the *superconducting ground state*.

Only electrons in a tiny range around the Fermi energy are involved in the formation of this state, as the potential $U_{\mathbf{k}\mathbf{k}'}$ of the attractive force scatters the electrons from a state with wave vector $\mathbf{k}$ to a state with wave vector $\mathbf{k}'$. In conventional superconductors the interaction potential $U_{\mathbf{k}\mathbf{k}'}$ is attributed to phonons so that the characteristic energy range $\hbar\omega_D$ is determined by the *Debye frequency*. Typically, the Fermi temperature is $T_F = E_F/k_B \approx 10^5\,K$ and the Debye temperature is $\theta_D = \hbar\omega_D/k_B \approx 10^2$ in metals, where k_B is the Boltzmann constant. If the electrons form a pair, their total energy $2E_F$

is lowered by an amount which is approximately given by

$$E \approx 2E_F - 2\hbar\omega_D \exp(-\frac{2}{n_\mathrm{n}(0)V}) \,. \tag{3.1}$$

Here $n_\mathrm{n}(0)$ is the density of electrons at the Fermi level and V is the volume of the system. A note has to be made that this "binding" can exist only relative to the Fermi level. The sea of still unpaired electrons is vital for this process. There is a limit for the range of this attractive force: the mean distance over which electrons can be paired up is the *BCS coherence length* ξ_0.

In order to find the superconducting ground state, Bardeen, Cooper and Schrieffer[1] in 1957 used a superposition of all possible occupied and unoccupied combinations of Cooper pair states in the form

$$\Psi_{BCS} = \prod_{k<k_F} \left(u_\mathbf{k} + v_\mathbf{k} a^\dagger_{\mathbf{k},\uparrow} a_{-\mathbf{k},\downarrow} \right) |0\rangle \tag{3.2}$$

as ansatz [BCS57]. $a^\dagger$ and a are the usual electron creation and destruction operators of electrons, which operate on the vacuum state $|0\rangle$. The product $a^\dagger_{\mathbf{k},\uparrow} a_{-\mathbf{k},\downarrow}$ creates the Cooper pair, which consists of two electrons with opposite spins and opposite wave vectors.

Two newly introduced complex factors hold the information of a pair state characterized by the electronic wave vector $\mathbf{k}$ being unoccupied ($u_\mathbf{k}$) or occupied ($v_\mathbf{k}$). $u_\mathbf{k}$ and $v_\mathbf{k}$ are not independent of each other, as they obey the normalization relation $|u_\mathbf{k}|^2 + |v_\mathbf{k}|^2 = 1$. Not unlike in a Bose-Einstein condensate, where the ground state wave function is spread over the whole system, the superconducting ground state wave function macroscopically extends over the whole superconductor.

After approximating the system Hamiltonian by a mean field approach and minimizing the ground state energy with respect to the $u_\mathbf{k}$ and $v_\mathbf{k}$, one finds

$$|u_\mathbf{k}|^2 = \frac{1}{2}\left(1 + \frac{\xi(\mathbf{k})}{|E_\mathbf{k}|}\right) \quad \text{and} \quad |v_\mathbf{k}|^2 = \frac{1}{2}\left(1 - \frac{\xi(\mathbf{k})}{|E_\mathbf{k}|}\right) . \tag{3.3}$$

$\xi(\mathbf{k})$ measures the energy of the electrons with respect to the Fermi level E_F. The eigenstates of the superconducting Hamiltonian are not electrons and holes but *quasi-particles* which are their linear superpositions. The eigenvalues of the Hamiltonian, which correspond to the energies of the quasi-particles, are given by

$$E_\mathbf{k} = \pm\sqrt{\xi_\mathbf{k}^2 + |\Delta|^2} \,. \tag{3.4}$$

As can be seen from this formula, no states exist for quasi-particles in an interval from $E_F - \Delta$ to $E_F + \Delta$. Thus Δ is also called the *gap function*, which is given by the expression

$$\Delta = U \sum_\mathbf{k} u^*_\mathbf{k} v_\mathbf{k} [1 - 2f(\xi(\mathbf{k}))] \,. \tag{3.5}$$

[1] Hence the name BCS theory

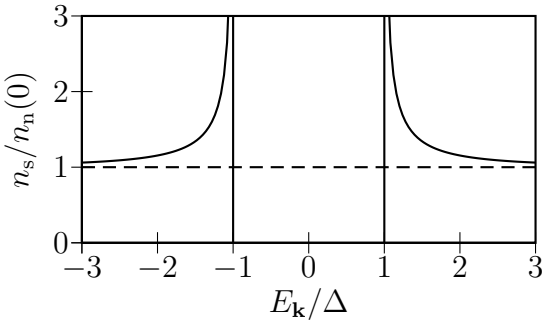

Figure 3.1: *Density of states of the quasi-particles (solid) in a superconductor normalized by the density of states of the electrons (dashed) at the Fermi energy in the normal state. The energy E is measured in units of the gap Δ.*

(Here, as an approximation, the interaction potential U is assumed to be constant and nonzero for electron energies only in a region $\hbar\omega_D$ around the Fermi level.) The expression under the sum is actually the thermal average of the pair operator

$$\langle a^\dagger_{\mathbf{k},\uparrow} a^\dagger_{-\mathbf{k},\downarrow} \rangle = u^*_{\mathbf{k}} v_{\mathbf{k}} [1 - 2f(\xi(\mathbf{k}))] \,. \tag{3.6}$$

It denotes the mean occupation of one pair state and is called the *pair amplitude*. Hence, besides describing the energy gap in the quasi-particle spectrum, (3.5) is a measure of the ability of the system to create pairs, which gave it the other name *pair potential*. $2|\Delta|$ is the energy needed to break up a Cooper pair. As the temperature approaches the critical value T_C, Δ goes to zero as $\Delta = 3.07 k_B T \sqrt{1 - (T/Tc)}$. The number 3.07 is peculiar to BCS theory, by quite well confirmed by experimental measurements as shown in table 3.1.

The density of states of the quasi-particles n_s can easily be derived. The transformation diagonalizing the superconducting Hamiltonian is unitary and therefore a bijective projection, i. e., to the electron with wave vector $\mathbf{k}$ and spin σ corresponds one and only one quasi-particle with the same wave vector and spin. Thus, also the number of states is preserved. This allows us to write $n_\mathrm{s}(E_\mathbf{k})\mathrm{d}E_\mathbf{k} = n_\mathrm{n}(\xi_\mathbf{k})\mathrm{d}\xi_\mathbf{k}$, where n_n is the density of states of the electrons in the normal conducting state. Referring to eq. (3.4) and taking into account that we are just looking at a small region around the Fermi energy in which $n_\mathrm{n}(\xi_\mathbf{k}) \approx n_\mathrm{n}(0)$, this yields

$$\frac{n_\mathrm{s}(E_\mathbf{k})}{n_\mathrm{n}(0)} \approx \frac{n_\mathrm{s}(E_\mathbf{k})}{n_\mathrm{n}(\xi_\mathbf{k})} = \frac{\mathrm{d}\xi_\mathbf{k}}{\mathrm{d}E_\mathbf{k}} = \begin{cases} \frac{E_\mathbf{k}}{\sqrt{E_\mathbf{k}^2 - \Delta^2}} & \text{if} \quad E_\mathbf{k} > \Delta \,, \\ 0 & \text{if} \quad E_\mathbf{k} < \Delta \,. \end{cases} \tag{3.7}$$

The graphical representation of this expression is shown in fig. 3.1. Directly at the energy gap, the quasi-particle DOS diverges. Far away from the gap, it asymptotically approaches the value of the electron DOS of the normal conducting state. This mirrors the fact, that the quasi-particles far above and far below the gap become more and more pure electrons and holes.

So, in summary, there is a ground state occupied by the superconducting condensate of the bosonic Cooper pairs. The pairs consist of electrons with opposite spins and wave

vectors. These electrons have energies close to the Fermi energy. The excited states are found at a distance at least $\pm|\Delta|$ away from the Fermi energy and can only be occupied by quasi-particles, which are fermionic linear superpositions of an electron and a hole. This is in stark contrast to the Bose-Einstein condensate, where excited states are also occupied by bosons.

Apart from the microscopic BCS theory just presented along general lines, a macroscopic theory had been developed earlier in 1950 by Ginzburg and Landau [GL50], based on thermodynamic reasoning. They minimized the Gibbs free energy with respect to the *order parameter* $\psi(\mathbf{r})$. This parameter, like its name suggests, is used to describe the degree of superconducting ordering during a phase transition and characteristically vanishes above a certain temperature T_C. The approach of Ginzburg and Landau resulted in a system of equations, where the first *Ginzburg-Landau Equation* looks like a Schrödinger equation for $\psi(\mathbf{r})$. Thus $\psi(\mathbf{r})$ behaves like a macroscopic quantum mechanical wave function It can be related to the Cooper pair density n_S and a phase $\varphi(\mathbf{r})$ in the following way:

$$\psi(\mathbf{r}) = \sqrt{n_S} e^{-i\varphi(\mathbf{r})}\,, \tag{3.8}$$

so that $\psi^*\psi = n_S$. Already in 1959 Gorkov showed that $\psi(\mathbf{r})$ is related to the gap function Δ of BCS theory [Gor59]. Close to T_C they are proportional: $\psi(\mathbf{r}) \propto \Delta$.

In the framework of the Ginzburg-Landau theory, critical fields B_c and critical currents I_c of various superconductor structures can be calculated. Both quantities are connected, as a current creates a magnetic field, which breaks the Cooper pairs. If this field gets so strong that the critical field is reached, superconductivity breaks down. The other view is also valid, as external magnetic fields excite shielding currents due to the diamagnetism of the superconductor, and so the critical current of the structure may be exceeded. The exact relation between these quantities depends on the geometry of the structure.

A very important concept in connection with superconductors is the penetration depth λ(T). Due to the screening currents mentioned already, a magnetic field is exponentially shielded from the interior of the superconductor with this characteristic length $\lambda(T)$. By electrodynamic reasoning a quantity called the *London penetration depth* can be derived:

$$\lambda_L = \sqrt{\frac{2m_e c^2}{4\pi n_s (2e)^2}}\,. \tag{3.9}$$

Here n_s is the total density of Cooper pairs with mass $2m_e$ and charge $2e$. The penetration depth of a superconductor is always greater than λ_L, and can be given analytically for the two limiting cases of a pure and dirty superconductor.

The purity of a superconductor is characterized by the ratio l/ξ_0. The expression for the electron *mean free path* $l = \tau v_F$ contains the time τ between two collisions and the velocity of a conduction electron at the Fermi level v_F. The BCS coherence length is $\xi_0 = \hbar v_F/\pi\Delta(0)$, with the energy gap at 0 K in the denominator. In the clean limit ($l \gg \xi_0$), the penetration depth is

$$\lambda(T) = 0.71\lambda_L \sqrt{\frac{1}{1-\frac{T}{T_C}}} \tag{3.10}$$

superconductor	T_c (K)	$B_c(0)$ (mT)	$\lambda(0)$ (nm)	ξ_0 (nm)	$\frac{2\Delta(0)}{k_B T_c}$	$\Delta(0)$ (meV)
Aluminum	1.14	10.5	16	1500	3.46	0.17
Indium	3.14	29.3	25	400	3.57	0.53
Tin	3.72	30.9	28	300	3.59	0.58
Tantalum	4.48	83	35	93	3.6	0.7
Lead	7.19	80.3	37	83	4.42	1.37
Niobium	9.25	198	45	28	3.74	1.53

Table 3.1: *The most important parameters of some classic superconductors [MGK96]. The penetration depth $\lambda(0)$ is given for the clean limit.*

and in the dirty limit ($l \ll \xi_0$)

$$\lambda(T) = 0.67\lambda_L \sqrt{\frac{\xi_0}{l}} \sqrt{\frac{1}{1-\frac{T}{T_C}}}\,. \tag{3.11}$$

An overview over the most important parameters of some classic superconductors is given in table 3.1.

3.2 Quasi-Particle Tunneling

Many interesting effects arise in quantum mechanics because of tunneling of particles, especially the tunneling of electrons is used to good effect in many electronic devices. Both Cooper pairs and quasi-particles are also able to tunnel through regions where superconductivity breaks down. Such regions may consist of e. g. insulators, normal metals and constrictions in the superconductor which are smaller than the superconducting coherence length ξ_0.

The tunneling of quasi-particles proceeds much in the same way like that of electrons. The difference is that the energy gap has to be taken into account. Fig. 3.2 shows the characteristics of N/I/N, N/I/S and S/I/S structures. The symbols mean N – normal conductor, I – insulator and S – superconductor. Whilst Ohmic behavior is expected for an N/I/N contact, the N/I/S tunnel current sets in only after eU is greater than the gap energy Δ. If $|eU| < \Delta$ and $T = 0\,K$ then, depending on the sign of eU, either the Fermi energy of the normal metal lies inside the gap of the superconductor, so that no states are available for tunneling, or the quasi-particles which occupy only states below $E_F - \Delta$ in the superconductor could only tunnel to states already taken by electrons in the normal conductor. At $T = 0\,\mathrm{K}$, the superconducting differential conductance of the N/I/S contact is proportional to the normal differential conductance and to the ratio of the densities of states, c. f. eq. (3.7), by

$$G_{\mathrm{NIS}}(U) = G_{\mathrm{NIN}} \frac{n_{\mathrm{s}}(eU)}{n_{\mathrm{n}}(0)}\,, \tag{3.12}$$

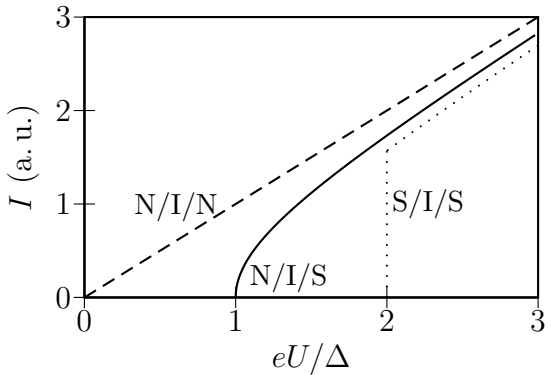

Figure 3.2: *I–V characteristic at 0 K of an insulating barrier sandwiched between two normal metals (N/I/N – dashed), a normal metal and a superconductor (N/I/S – solid) and between two superconductors (S/I/S – dotted). The voltage is measured in units of the superconducting gap energy* Δ.

thereof the current-voltage characteristic can be obtained by the integration $I(U) = \int_0^U G_{\mathrm{NIS}}(U')dU'$. The other way round, the measurement of $I(U)$ and a subsequent differentiation recovers directly the density of states. At finite temperatures $T > 0\,K$, the I-U-characteristic smears out, and tunneling is possible also at $|eU| < \Delta$ as now quasi-particle states above the gap are occupied and the occupation at the Fermi level is broadened in the normal metal and no longer a step.

As the last case, an S/I/S junction is shown in fig. 3.2. If, to simplify matters, both superconductors have the same energy gap, tunneling of quasi-particles sets in at $|eU| > 2\Delta$. The lower edge of the gap on one side has to be aligned with the upper edge on the other side. The quasi-particle density of states is infinite directly at the gap edges. Therefore a discontinuous jump appears at 2Δ. This picture is valid for the idealistic case of $T = 0\,\mathrm{K}$. At nonzero temperature all the kinks in the curves for N/I/S and S/I/S tunneling get smoothed out due to thermal broadening.

If the gaps are not equal, then tunneling can, to a limited extent, occur already below $\Delta_1 + \Delta_2$.

3.3 Proximity Effect

At the contact interface between a superconductor and a normal metal, the pair potential eq. (3.5) drops to zero, as the potential of the attractive force vanishes in the normal metal. However, the Cooper pair density cannot abruptly disappear. The length scale over which such macroscopic quantities are allowed to change significantly is given by the *Ginzburg-Landau coherence length* ξ_{GL}, a property of the macroscopic order parameter, which varies from 3 nm to 1000 nm for pure conventional superconductors. This quantity is not to be confused with the BCS coherence length ξ_0 which determines the range over which the pairing force is effective. Another fundamental difference is the fact that while ξ_0 is almost constant with respect to temperature, ξ_{GL} is temperature dependent with a

divergence at the transition temperature T_C:

$$\xi_{GL}(T) = \frac{\xi_{GL}(0)}{\sqrt{1 - T/T_C}} \,. \tag{3.13}$$

At $T = 0\,\mathrm{K}$, $\xi_{GL}(T)$ is equal to $0.86\sqrt{\xi_0 \ell}$, with ℓ being the mean free path of the electrons.

The Cooper pair density decreases exponentially in the normal metal

$$n_\mathrm{s} = \psi(d)^* \psi(d) \propto e^{-d/\xi_\mathrm{N}} \,. \tag{3.14}$$

ξ_N is the *normal metal coherence length*. In the clean or ballistic limit it is given by fundamental quantities:

$$\xi_\mathrm{N,clean} = \xi_\mathrm{N}^0 = \frac{\hbar v_F}{2\pi k_B T} \,. \tag{3.15}$$

If the mean free path of the electron motion is smaller than this coherence length, i. e. $l < \xi_\mathrm{N}^0$, then we are in the diffusive limit and

$$\xi_\mathrm{N,diff} = \sqrt{\frac{\xi_\mathrm{N}^0 l}{3}} = \sqrt{\frac{\hbar D_N}{2\pi k_B T}} \tag{3.16}$$

with the diffusion constant of the normal metal $D_N = v_F l/3$ and the Fermi velocity v_F [Kog82].

The intrusion of Cooper pairs into the normal metal induces a *pseudo gap*. This leaking of the superconducting properties into the normal metal enhances its conductivity. Inversely, the effect of the normal metal is felt in the superconductor leading to a reduction of the gap at the S/N interface. This process is called *inverse proximity effect*.

The considerations for nonmagnetic normal metals stay valid also for ferromagnetic metals. However, the pair breaking effect of the thermal energy $k_B T$ is augmented by the exchange energy E_{Ex}, which tends to align spins parallel. In the temperature range of conventional superconductors, it is even the dominating effect. In the dilute ferromagnet $\mathrm{Pd_{95}Fe_5}$ the Curie temperature is $T_\mathrm{Curie} \approx 150\,\mathrm{K}$ while for niobium the superconducting critical temperature is $T_\mathrm{C} \approx 9.25\,\mathrm{K}$. So the exchange energy exceeds the thermal energy in the material system used in this work by a factor of 10 to 20. This has an effect on the coherence length, which is reduced to a few nanometers in ferromagnets and is represented in the diffusive limit and a weak ferromagnet by [ROR+01]

$$\xi_\mathrm{F,diff} = \sqrt{\frac{\hbar D_F}{2(\pi k_B T + \mathrm{i} E_{Ex})}} \,, \tag{3.17}$$

where D_F is the diffusion constant of the ferromagnet. Additionally, the imaginary component leads to an oscillatory behavior of the order parameter inside the ferromagnet, which is used to realize π-contacts. In the clean limit, the order parameter oscillates too, but decays at a length scale of the mean free path l [BVE02].

3.4 Josephson Effect

This effect describes the tunneling of Cooper pairs from one superconducting electrode to another, which are separated by a weak link, like thin insulating barriers, normal metals which become weakly superconducting by the proximity effect, or constrictions which suppress superconductivity because of their small dimensions.

B. D. Josephson derived two equations for the current and phase of such a junction [Jos62], [Jos65]. The first one predicts the supercurrent through the junction in the zero voltage case

$$I_s = I_c \sin\gamma \,. \tag{3.18}$$

The second equation describes the behavior of the relative phase γ between the two superconductors if a voltage V is applied across the junction.

$$\mathrm{d}\gamma/\mathrm{d}t = 2eV/\hbar \,. \tag{3.19}$$

For instance, a constant voltage would result in a continuously growing phase, which again gives an alternating current following eq. (3.18). Here $\gamma = \Delta\phi - (2\pi/\Phi_0)\int \mathbf{A}\mathrm{d}\mathbf{s}$ is the *gauge-invariant phase difference*, which takes the additional phase into consideration which an electromagnetic vector potential yields.

3.5 Fluxoid Quantization

In a superconducting ring, the macroscopic wave function of the superconducting ground state $\psi(\mathbf{r}) = |\psi(\mathbf{r})|e^{-i\varphi(r)}$ must be single valued. After completing one loop, the phase may have changed only by an integral multiple of 2π:

$$\Delta\varphi = \oint \nabla\varphi(\mathbf{r})\mathrm{d}\mathbf{r} = n \cdot 2\pi \,. \tag{3.20}$$

A magnetic field $\mathbf{B} = \nabla \times \mathbf{A}$, which permeates the area bounded by the closed path, may lead to an additional pick up of phase, which is the well known *Aharonov-Bohm effect*, expressed by

$$\varphi_{AB} = \frac{2\pi}{\Phi_0}\oint \mathbf{A}(\mathbf{r})\mathrm{d}\mathbf{r} = \frac{\Phi}{\Phi_0} \,. \tag{3.21}$$

The superconducting flux quantum is given by $\Phi_0 = hc/(2e) = 2.07 \times 10^{-15}\,\mathrm{Wb}$.

Another contribution to the phase comes from the circulating current $\mathbf{J}_s$ in the superconductor, which, due to its diamagnetic behavior, is stimulated by the external magnetic field B. This phase is given by

$$\varphi_s = \frac{m}{eh}\oint \frac{\mathbf{J_s}}{|\psi(\mathbf{r})|^2}\mathrm{d}\mathbf{r} = \frac{\Phi_s}{\Phi_0} \,, \tag{3.22}$$

where m and e are the electron mass and charge, respectively.

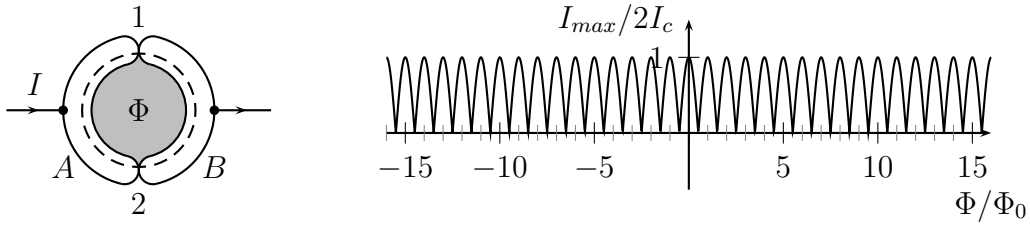

Figure 3.3: *SQUID structure and interference pattern of Josephson tunneling. The SQUID is formed by the superconductors A and B which are separated by the weak links* 1 *and* 2*. The dashed circle indicates the integration path for determining the flux* Φ *interspersing the light gray area. On the right, the typical interference pattern representing the maximum current* I_m *through the SQUID is displayed. Adapted from [Tin96] and [BP82].*

The complete phase change is the sum of both, $\Delta\varphi = \varphi_{AB} + \varphi_s$, from which the formula for *fluxoid quantization* is derived as

$$n\Phi_0 = \Phi + \Phi_s \,. \tag{3.23}$$

The quantity $\Phi + \Phi_s$ is the *fluxoid.*

As the superconducting current $\mathbf{J}_s$ only flows in a small region inside the ring, there is the possibility of moving the integration path deep inside the superconductor where $\mathbf{J}_s = 0$, provided it is thick enough. This leaves us with the simple formula for flux quantization

$$\Phi = n\Phi_0 \,, \tag{3.24}$$

stating that the magnetic flux through a normal region enclosed by superconducting material is a multiple of the superconducting flux quantum.

3.6 Quantum Interference

If two weak links are placed in a superconducting ring, a SQUID geometry as shown in fig. 3.3 is created. The phase differences γ_1 and γ_2 of the weak links 1 and 2 which separate the superconducting electrodes A and B contribute to the total phase taken around the contour indicated by a dashed line. By the same arguments as in sec. 3.5 a relation between the flux and the phases across the weak links is obtained as $\Delta\gamma = \gamma_1 - \gamma_2 = 2\pi(\Phi/\Phi_0 - n)$, with n selected such that $0 \leq \Delta\gamma \leq 2\pi$. The maximum supercurrent I_m that the SQUID can sustain is then given by calculating the maximum of the sum of the supercurrents through the weak links $I_s = I_{s1} + I_{s2}$, which, if both weak links support the same maximum supercurrent I_c, yields

$$I_m = 2I_c \left| \cos\left(\pi \frac{\Phi}{\Phi_0}\right) \right| \,. \tag{3.25}$$

This interference pattern is shown on the upper right hand side of fig. 3.3.

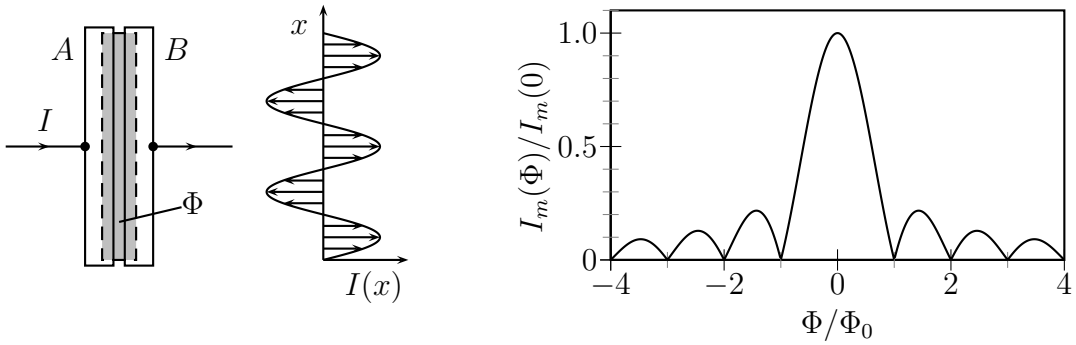

Figure 3.4: *Extended weak link, supercurrent distribution and interference pattern. The light gray area is the area of the weak link, where the flux* Φ *can penetrate into the superconductor. The figure in the middle shows the local current distribution in the junction. The right picture is the maximum supercurrent through the junction depending on the penetrating flux. The curve has the same form as a Fraunhofer diffraction pattern. Adapted from [Tin96].*

Up to now the weak links were considered small enough to have a unique phase all over. For extended Josephson junctions the penetrating flux causes a spatial variation of the phase. This is depicted in fig. 3.4. The flux Φ through the junction goes through an area that is composed of the area of the weak link and the area which extends the penetration depth λ into the superconductor. This flux creates a sinusoidal variation of the phase, which is transferred to the local current over the weak link. If the flux is an integral multiple of the flux quantum Φ_0, then the sinus completes a full cycle and the currents over the junction add up to zero. The maximum current is reached if the flux is and integral multiple plus one half of the flux quantum. The effective current flowing is limited by the critical current of the junction. The currents which cancel out still flow locally over the junction, reducing in this way the current that can effectively cross the junction. This behavior of the observed maximum supercurrent is described by the formula

$$\frac{I_m(\Phi)}{I_m(0)} = \frac{\sin(\pi\Phi/\Phi_0)}{\pi\Phi/\Phi_0}\,, \tag{3.26}$$

whose graphical representation yields the *Fraunhofer pattern* given in the rightmost plot of fig. 3.4.

3.7 Charge Imbalance

In thermal equilibrium, the quasi-particle states are occupied according to the Fermi function $f_0(E_\mathbf{k}/k_BT) = (1 + exp(E_\mathbf{k}/k_BT))^{-1}$, where $E_\mathbf{k}$ is the quasi-particle energy defined in eq. (3.4). If the system is driven out of equilibrium, e. g. by injecting quasi-particles or destroying pairs by irradiation with photons, then a new dynamic equilibrium is set up with a new occupation of states $f_\mathbf{k}$. This is achieved by balancing the perturbations with relaxation and diffusion.

Favourably, physical quantities are described in terms of the deviation from equilibrium $\delta f_{\mathbf{k}} = f_{\mathbf{k}} - f_0(E_{\mathbf{k}}/k_B T)$. These deviations are classified in *even or energy mode* and *odd or charge mode* [SS75].

Even mode deviations are caused by charge neutral perturbations of the system, e. g. phonons and photons, which normally lead to the same redistribution of both more hole-like and more electron-like quasi-particle states. Such perturbations are able both to diminish or enhance the superconducting gap Δ.

Odd mode deviations, also called *charge imbalance*, are characterized by a nonzero net charge density Q^*. They are caused by charged perturbations, like electron or hole injection, and the conversion of normal current into supercurrent.

In equilibrium, the BCS quasi-particle charge is

$$q_{\mathbf{k}} \equiv (u_{\mathbf{k}}^2 - v_{\mathbf{k}}^2) = \frac{\xi_{\mathbf{k}}}{E_{\mathbf{k}}} = \frac{\xi_{\mathbf{k}}}{\sqrt{\xi_{\mathbf{k}}^2 + \Delta^2}} \,. \tag{3.27}$$

The contribution of the quasi-particles to the total charge Q^* of the systems is determined by the occupation of states $f_{\mathbf{k}}$ (V being the volume of the system) [Gra81]:

$$Q^* = \frac{2}{V} \sum_{\mathbf{k}} q_{\mathbf{k}} f_{\mathbf{k}} \,. \tag{3.28}$$

In thermal equilibrium, $f_{\mathbf{k}}$ is the Fermi function which is even in $\mathbf{k}$. As $q_{\mathbf{k}}$ is odd in $\mathbf{k}$, the total quasi-particle charge is 0.

The nonequilibrium case can be understood by considering an experiment carried out by J. Clarke in 1972 [Cla72]. There, the equilibrium is disturbed by injecting electrons from a normal contact into a superconductor. The voltage U used for injection plays a crucial role. If $eU = \Delta$, then the quasi-particle excitation caused by the electron lies close to the gap, so that the charge contribution is $q_{\mathbf{k}} = 0$. If the voltage is chosen in a way that $eU \gg \Delta$ then the quasi-particle carries a charge almost equal to 1 and contributes fully to the disequilibrium Q^*.

If eU lies inside the gap, then the conversion of normal to supercurrent proceeds by *Andreev reflection* [And64]. This process is illustrated in fig. 3.5. An electron incident at the interface from the normal metal cannot simply enter the superconductor, as there are no states available inside the gap. Instead, it is converted into a Cooper pair at the interface and a hole is reflected back on the normal side. Thus, the charge transferred is 2e which doubles the conductivity compared to the normal case.

The nonequilibrium charge accumulation Q^* leads to an odd occupation between hole-like and electron quasi-particle states, as can be seen in fig. 3.6b. To provide for overall charge neutrality, the number of electrons in the superconducting condensate must change. If electron-like quasi-particles are injected, pairs must be removed, if hole-like quasi-particles are injected, pairs are accumulated in the injection region. Therefore the pair electrochemical potential μ_p is lowered or increased, respectively. The change in the quasi-particle electrochemical potential μ_n is counteracted exactly by the change of the pair electrochemical potential μ_p. The difference in electrochemical potentials can

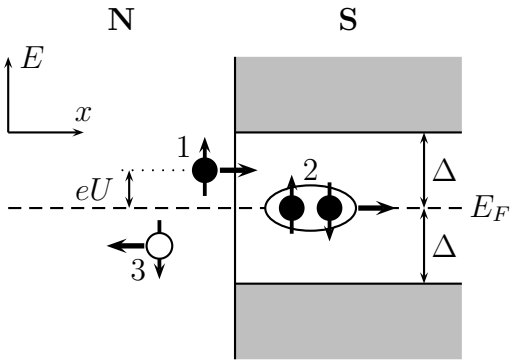

Figure 3.5: *Schematic picture of Andreev reflection. An electron (1) incident from the normal side of the N/S interface with an energy $eU < \Delta$ enters the superconductor pairing up (2) with another electron. A hole (3) with opposite energy relative to the Fermi energy E_F and opposite spin is reflected back in the normal metal (conservation of energy and angular momentum). The charge that contributes to the current is $2e$.*

be sensed by measuring the voltage that develops between the superconductor and the normal metal.

At a distance x away from the injection region, the charge accumulation Q^* fades out due to diffusion as $Q^*(x) = Q^*(0)\exp(-x/\Lambda_{Q^*})$, with the diffusion length $\Lambda_{Q^*} = \sqrt{D\tau_{Q^*}}$, the diffusion constant $D = 1/3v_F\ell$, and the decay time $\tau_{Q^*} = (4/\pi)(k_BT_C/\Delta)\tau_{\text{in}}(0)$ [SS75], where $\tau_{\text{in}}(0)$ is the inelastic relaxation rate of a normal state electron (hole) at the Fermi level and ℓ its mean free path. Contacting the superconductor within the decay length Λ_{Q^*} with a superconducting probe will enable us to measure μ_p, contacting it, on the other hand, with a normal probe will result in a determination of μ_n. The small distances require microfabrication techniques.

There is another way to measure the effect of charge imbalance which does not rely on mesoscopic structures. The charge imbalance in the superconductor is balanced by inelastic scattering processes which reduce the energy of the quasi-particles until they are all wrapped up in the superconducting condensate. This process is dissipative, resulting in a resistance that by far exceeds the value of the same system being above the critical temperature of the superconductor, i. e. when both metals are normal conducting. A formula for the resistance close to T_C is given in [HPT74]

$$\frac{R(T)}{R(0)} = \eta\left(\frac{\Delta(0)}{\Delta(T)}\right)^{\frac{2}{3}}\coth\left(\frac{\Delta(T)}{2k_BT}\right), \tag{3.29}$$

where $\eta \approx 0.83$. For typical BCS values $\Delta(0) = 1.764k_BT_C$, $\Delta(T)/\Delta(0) \approx 1.74(1-t)^{1/2}$ and $t = T/T_C$ this is plotted in fig. 3.7. The resistance diverges for $T = T_C$. Here, the superconducting gap starts to open up, but it is still so small, that many electrons from the normal metal enter the superconductor as quasiparticles and decay dissipatively to Cooper pairs. As the gap gets bigger with decreasing temperature, less and less

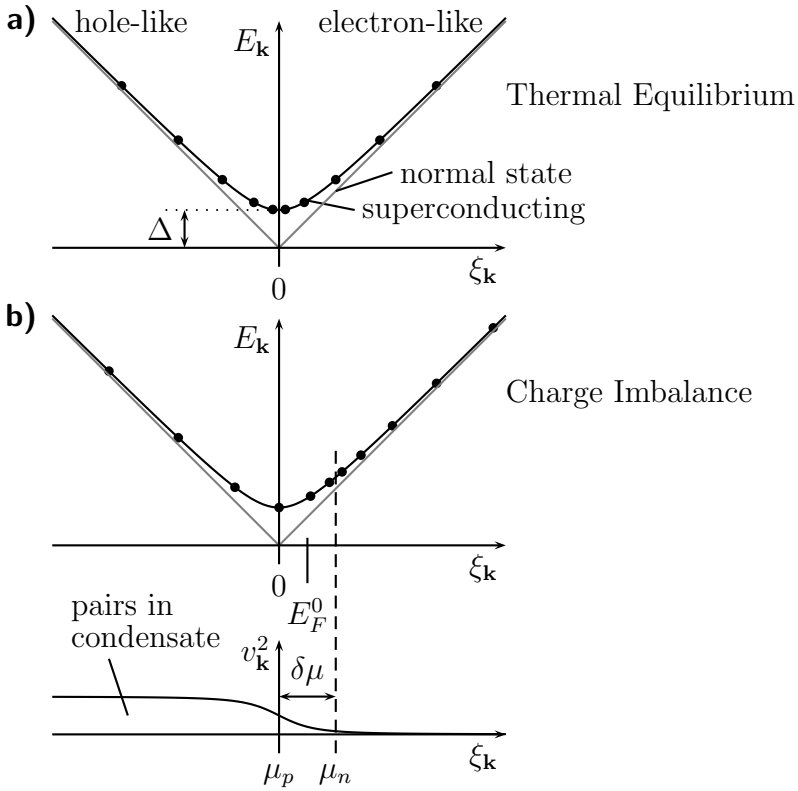

Figure 3.6: *Charge or branch imbalance. In all graphs, the ordinate expresses the wave vector in terms of electron and hole energy relative to the Fermi energy.* $\xi_{\mathbf{k}} = 0$ *corresponds to the Fermi energy. The abscissa is the energy of the particles. a) The superconducting system in equilibrium. The straight gray lines show the dispersion of the electrons and holes in the normal state. An energy gap* Δ *opens up for the quasi-particles in the superconducting state. The occupation of the quasi-particles is the same on the hole-like and the electron-like side. b) Distortion of the equilibrium by a charged perturbation. Electron-like quasi-particles are injected. The occupation on the electron-like branch is then higher than on the hole-like branch. The electrochemical potentials of quasi-particles* μ_n *and pairs* μ_p *are shifted the same distance away from the equilibrium values* E_F^0 *resulting in a difference* $\delta\mu$*. [Tin96]*

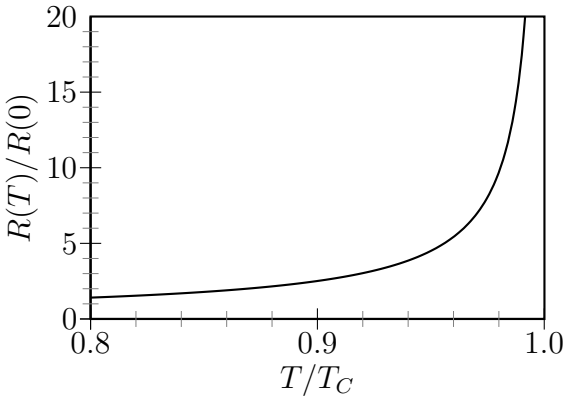

Figure 3.7: *Temperature dependent resistance of an N/S interface below T_C caused by charge imbalance.*

quasi-particles are injected into the superconductor and this process is more and more suppressed, decreasing also the dissipation and hence the resistance. The conversion of the normal current now proceeds by Andreev reflection creating pairs directly.

4 Sample Fabrication And Measurement Setup

Although the samples in this work essentially have the form of palladium-iron bridges between two superconductors, most measurements were performed on the bilayer of niobium and the palladium-iron extension of the bridge under it. The dimensions of typically some hundred nanometers require microfabrication techniques, which were achieved by electron beam lithography. As superconductivity in niobium is sensitive to contamination, it was structured and deposited using a mask suspended above the substrate. Therefore the *PES technique* was adapted to this process.

The samples were cooled down in a ^{3}He cryostat. Different measurement techniques were applied having their respective advantages and disadvantages. The three setups are presented in this chapter for measuring magnetoresistance, differential resistance and I-V characteristics.

4.1 Sample Types And Their Preparation

The measurements were performed on two types of samples. Fig. 4.1 shows the two designs. Design 1 only possesses six niobium probes, whereas design 2 also allows to contact the $Pd_{95}Fe_5$ layer.

Both structures were fabricated on top of an oxidized silicon substrate. The thickness of the insulating silicon dioxide on top of the p-doped monocrystalline silicon was 300 nm. Before starting the lithography, the surface of the layer was cleaned in smooth oxygen plasma. This is vital for the adhesion of the polyether sulfone resist (PES) in a later stage of processing. Then alignment markers, leads and bonding pads were defined by electron beam lithography (EBL), deposition of gold and lift-off. The thickness of the gold film was 30 nm, sitting on top of 5 nm titanium, which served as adhesion layer. These small thicknesses were chosen to avoid the rupture of the niobium and palladium-iron films at the edges of these gold leads. The titanium layer was not allowed to be thicker than 7 nm, otherwise the adhesion effect was lost.

In the next step, the fine palladium-iron structures were made again by EBL and lift-off. For design 1 samples, palladium stripes with dimensions 4000 nm by 200 nm were produced. The length and width in design 2 samples were 9000 nm and 200 nm, respectively. Here, the additional palladium-iron leads extended to the gold leads. Before evaporating palladium iron, the sample was exposed to an argon plasma, removing the adsorbates from the gold surface. The evaporation of palladium-iron was done in an ultra high vacuum system from two effusion cells as described in sec. 2.1.2.

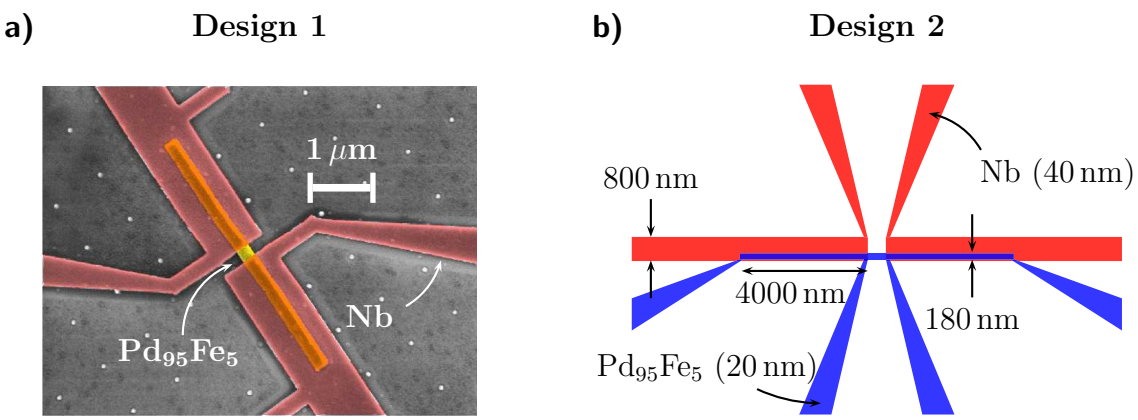

Figure 4.1: *Sample types. The niobium is evaporated always on top of the $Pd_{95}Fe_5$ structure. The layer thicknesses of niobium and palladium-iron were 40 nm and 20 nm respectively in both designs. The pure $Pd_{95}Fe_5$ bridges between the niobium stripes were 200 nm, 400 nm, 600 nm and 800 nm long. b) Electron beam micrograph of design 1 with two niobium current contacts (broad niobium stripes) and four niobium voltage probes. b) Extended design with four niobium and four $Pd_{95}Fe_5$ probes.*

The evaporation of niobium by electron beam evaporation puts high stress on the resist. For good superconducting properties it is important to avoid the inclusion of impurities in the niobium layer. To cope with both these problems, a technique similar to [DCC+00] and [HSSS02] of structuring niobium through a mask was used. By this process, the contact between niobium and any other material besides the substrate is avoided. As an illustration see fig. 4.2. This method was established by Andreas Bauer and Markus Gaass at the University of Regensburg [Bau05],[Ben04]. First a supporting layer of 700 nm to 800 nm polyether sulfone (PES) was spun on the substrate with the prefabricated gold leads and the $Pd_{95}Fe_5$ structures. Then the mask layer consisting of 60 nm Si_3N_4 was deposited by plasma enhanced vapor deposition. On top of the Si_3N_4, the EBL resist (PMMA) was applied. After exposing and developing this electron beam sensitive layer, the uncovered areas of the Si_3N_4 were etched by reactive ion etching in a directed CHF_3 plasma, followed by a pure and undirected oxygen plasma to etch the now uncovered PES underneath the Si_3N_4 layer. This results in a sharply defined silicon nitride mask, of which the edges are free standing due to the undercut etched in the PES layer. After the deposition of niobium by electron beam evaporation, the substrate was cleaved, yielding four equal pieces 4 mm by 4 mm big and then the PES layer together with the silicon nitride mask layer was removed by lift-off in n-methyl-2-pyrollidone (NMP). Each piece contained four finished structures ready to be glued into a chip carrier and to be contacted by bonding. The mask evaporation is illustrated in fig. 4.2. The detailed recipes and accurate data can be found in appendix A.

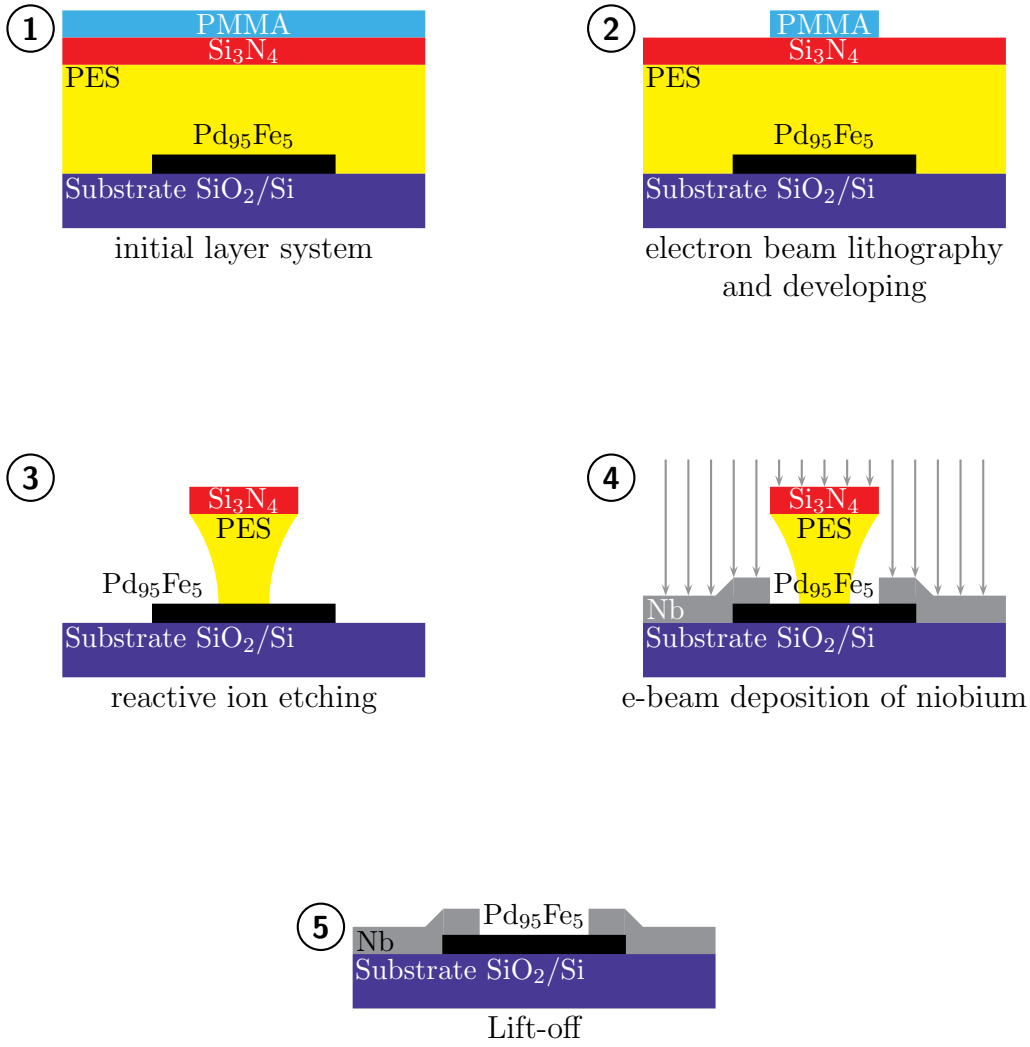

Figure 4.2: *The integral steps of the PES/Si_3N_4 shadow mask technique.*

4.2 Measurement Setup

The measurements were performed in a top loading ^{3}He-Cryostat Oxford Heliox VL, which was set up during this work. The base temperature of the system was 280 mK. At the start of the leads at the inset from outside, the measurement lines were filtered at room temperature by π-filters. Close to the sample holder, copper powder filters provided additional radio frequency filtering of the voltage lines implemented with coaxial cables between the π-filters and the copper powder filters. Also the current lines passed copper powder filters. The radio frequency filtering supplied by both kinds of filters was necessary to inhibit the heating of the electron system in the sample and to reduce noise.

The sample holder was equipped with a rotation mechanism, allowing stepless tilting of the sample relative to the magnetic field. The superconducting magnet was capable of producing fields up to 12 T.

4.2.1 Differential Resistance

All measurements were done in a 4-point layout. As can be seen in fig. 4.3a, a small oscillating signal (37 Hz) from one of the lock-in amplifiers was fed into the current lines. On top of this, a dc ramp was added by a Yokogawa 7561 power supply. The current in the circuit was determined by a large series resistance of 100 kΩ or 1 MΩ dominating the sample resistance of typically a few 100 Ω. The oscillating component was chosen to be 0.1 μA while the dc component could reach up to 50 μA during the measurements.

This combined ac and ramp current was usually run to ground or to a lock-in amplifier in current mode for control. The voltage signal taken from the voltage probes was fed to two Arstec LI-75 A voltage preamplifiers which output the difference of the two input signals amplified by a factor of 100. The ac component was then sensed by lock-in amplifiers (Stanford Research 830) and recorded by the measurement program *Measure XP* on a personal computer. This program also took control of sweeping the temperature, the magnetic field or V_{dc}.

A facility to run batch jobs was built in, which provided the possibility to measure the dependence of a quantity on two parameters. For instance, V_{dc} and consequently the dc current through the sample could be swept continuously at different magnetic fields, which was increased step by step for every sweep. In this way, color coded plots of differential conductance depending on current and magnetic field could be obtained.

4.2.2 Magnetoresistance

A variation of the above setup was used to measure the magnetoresistance of the samples. The magnetic field was swept and the voltage drop at the sample was sensed by a lock-in technique. An oscillating voltage, which was also provided by the lock-in amplifier, was converted to an oscillating current by a high series resistance of 100 kΩ or 1 MΩ.

The voltage from the probe sensed by the lock-in amplifier consisted of a small component oscillating with magnetic field and an offset not impaired by the magnetic field. In order to increase the sensitivity of the measurement, this offset was compensated. To this end, an appropriate voltage was branched off directly from the oscillator output of the lock-in amplifier by an adjustable voltage divider, as is shown in fig. 4.3b. This voltage was subtracted from the signal coming from the sample by a lock-in amplifier, leaving over only the oscillating component, which then could be measured at an increased sensitivity.

While finding the compensation voltage, there are two things to observe. First, the mean amplitude of the noise of the total signal (offset included) must not be much larger than the signal with the offset subtracted. Otherwise the sensitivity cannot be increased to the optimum value at the lock-in, because this noise cannot be compensated. Second, the phase of the complete signal must be very small, preferably below ±1 °. A big phase, coming from inductances and capacitances in the circuit, would increase the out of phase part. This part can again not be compensated with the signal from the voltage divider, which is in phase. The out of phase signal would then dominate the oscillating part of the sample signal, again hindering the increase of sensitivity. Usually the magnitude of

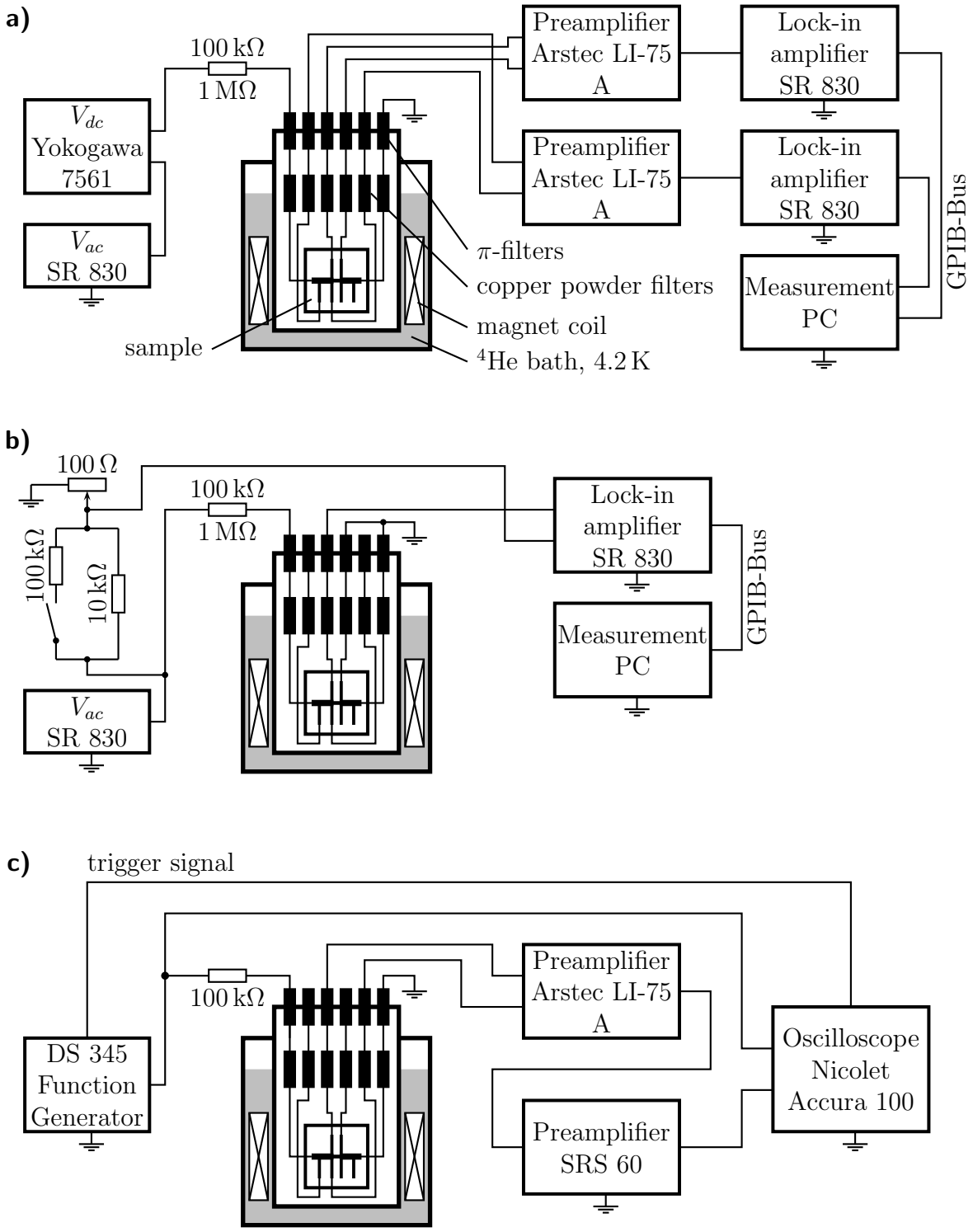

Figure 4.3: *Experimentation setups for the measurement of a) differential resistance, b) magnetoresistance, and c) I-V characteristics. The reference signals which connect the oscillator and the lock-in amplifiers are not shown for reasons of clarity.*

the out of phase signal is on the order of the compensated in-phase signal.

4.2.3 I-V Characteristics

A very fast way of obtaining the image plots of the I-V characteristic of the sample depending magnetic field is shown in fig. 4.3. The storage oscilloscope Accura 100 by Nicolet and the function generator SRS 60 by Stanford Research Systems constituted the integral parts of the setup. The voltage ramps produced by the function generator were converted to current ramps by a series resistor of $100\,\Omega$ and guided to the sample and, after flowing through the sample, finally to ground. The voltage ramp was directly fed to the oscilloscope to have a measure of the current through the sample. The voltage drop measured at the sample was then processed by two preamplifiers. The first, the Arstec LI-75 A, provided a low-noise enhancement of the signal by a factor of 100. The second one, the SRS 60 by Stanford Research Systems, had the additional ability of high and low pass frequency filtering, thereby reducing the noise of the signal.

The amplified and filtered signal was then conducted to one signal input of the Accura 100. At each start of a current ramp, the function generator gave a trigger pulse to the oscilloscope, which then started recording the current and voltage. The data obtained during the measurement of several, typically 10, ramps was averaged to increase the signal to noise ratio and then stored in a file. To take one averaged curve in this setup takes a few milliseconds. The minimal interval between the acquirement of one I-V characteristic was one second. During this process other parameters, like the magnetic field or temperature can be swept continuously.

The measurement program which coordinates the interplay of the function generator, the oscilloscope, and the sweep devices was developed by Florian Otto at the University of Regensburg. At the cost of having more noisy data, the measurement time for an image plot is reduced to one to two hours, compared to ten to twenty hours needed for one plot by recording the differential resistance with the method described in section 4.2.1.

5 Results Of The Measurements

Measurements of samples of niobium and the diluted ferromagnet showed pronounced magnetoresistance oscillations. These were further investigated by looking at the differential resistance depending on current and magnetic field, where effects could be found which explain the magnetoresistance oscillations. The location of the origin of the differential resistance was then tested by investigating various contact configurations. A sample with only nonmagnetic material was measured to affirm, that a ferromagnetic layer is vital for producing this behavior.

5.1 Samples: Overview

There are two types of samples as already described in sec. 4.1. Samples of design 1 only provide Niobium leads. In the next chapters the samples 606-2, 606-6 and 610 are of this type. They do not provide as much possibilities for measurement, as do the design 2 samples, which provide also leads to the $Pd_{95}Fe_5$ layer. The facility to vary the contact configuration and mix Niobium and palladium-iron leads proved important for narrowing down the origin of magnetoresistance and also to see charge imbalance.

Exactly the same method was used to produce both types of samples (c. f. appendix A). Also the layer thicknesses and the composition of the diluted ferromagnet was the same within the limits of preparation (see sec. 2.1.2).

5.2 Critical Temperatures

The results of the measurements of the critical temperature is shown in fig. 5.1. They were performed using a simple lock-in technique in 4-point geometry. Different amplitudes for the alternating current were chosen. The graphs show the resistance of the samples versus temperature. The current was sent along one broad niobium contact, over the $Pd_{95}Fe_5$ bridge and to ground over the other broad niobium contact. The voltage drop was measured at the probes closer to the bridge. For sample 902A also a nonlocal configuration was examined.

5.2.1 Design 1

Both design 1 samples show steps in the $R(T)$ curves, which are attributed to regions of niobium with different critical temperatures, as can be seen in fig. 5.1a and 5.1b. These are due to different geometries and to the proximity of niobium to palladium-iron. Starting with high and going down to low temperatures, the first step lies clearly at

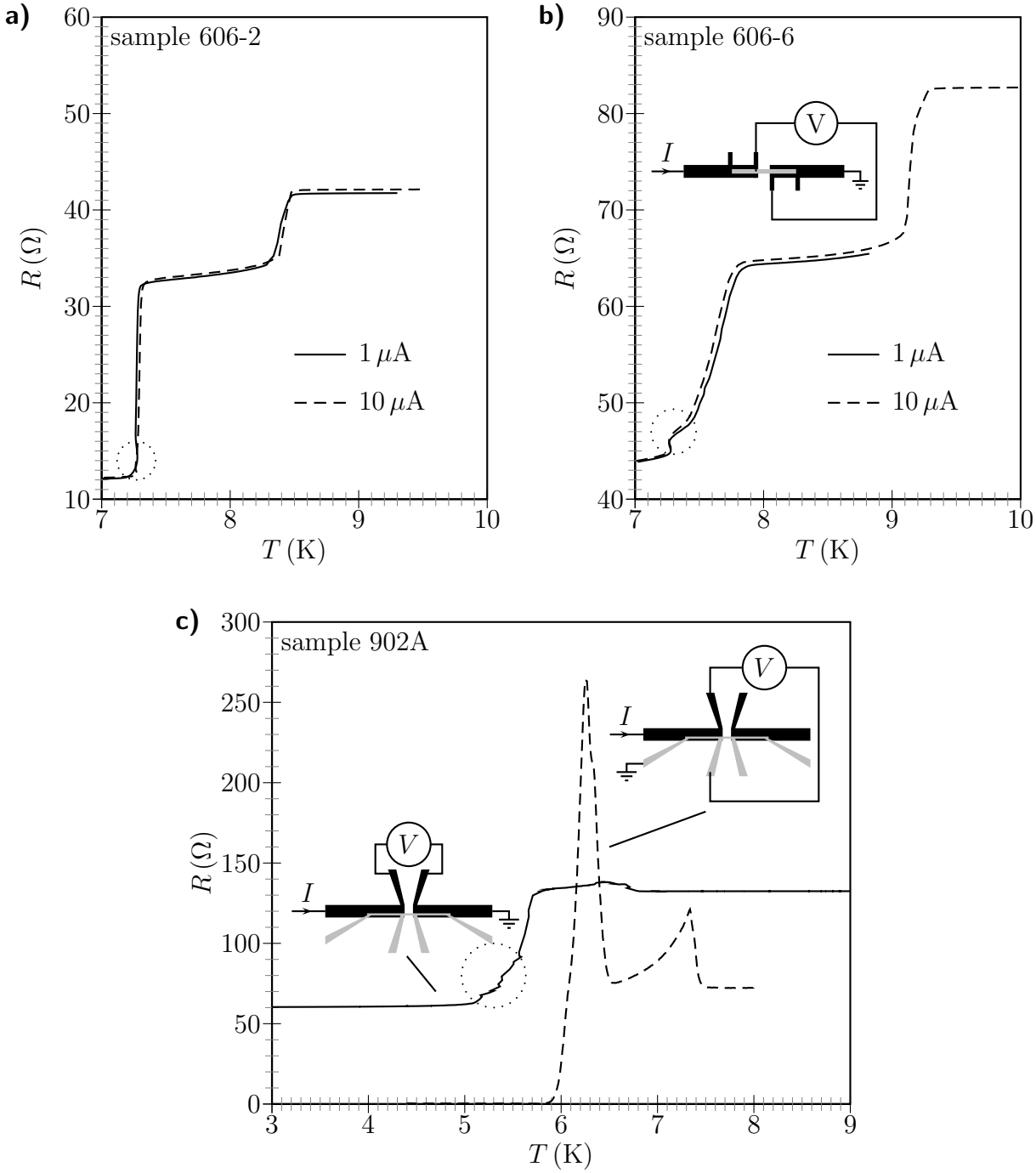

Figure 5.1: *Resistance depending on temperature. a) 606-2 (200 nm bridge), b) 606-6 (600 nm bridge) with design 1 and c) 902A with design 2. The contact configuration for the samples 606-2 and 606-6 is sketched in graph b). Sample 902A was measured with an alternating current of 1 μA in 2 contact configurations: in a nonlocal configuration (dashed) and in bridge configuration (solid). For the samples 606-2 and 606-6 the dotted circle indicates an irregularity due to a thermometer recalibration. for 902A the circle indicates a region of unstable temperature.*

different positions for the two samples: at 8.4 K for the 200 nm sample and at 9.1 K for the 600 nm sample. The second jump ends at 7.25 K for both samples, being sharp for 606-2 and smooth for 606-6. The irregularities at the foot of this jump, indicated by a dotted circle, should be disregarded. They result from a recalibration of the sample thermometer and a subsequent adjustment of the already measured data. The recalibration curve showed a step at exactly that point. The reason for this is not clear.

The residual resistance at 7 K and below must be attributed to the palladium-iron bridges. Being 43.8 Ω for the 600 nm sample and 15.7 Ω for the 200 nm sample, the resistance ratio of 3.5 : 1 corresponds approximately to the ratio of the bridge lengths of 600 nm : 200 nm. Together with the width of the bridges of 180 nm, the resistance of one square of $Pd_{95}Fe_5$ can be determined as 15.7 Ω for 606-2 and as 18.3 Ω for 606-6. This coincides with the results found in table 2.1.

5.2.2 Design 2

Fig. 5.1c displays the behavior of sample 902A. The black curve is measured in the same contact configuration same as the 606 samples. The bridge is included in the current path, hence the name *bridge configuration*. The second kind of measurement involved a nonlocal contact configuration where the voltage is not measured along the current path.

A time span of two weeks lies between the recording times of these two curves. The nonlocal configuration was measured first. The in between the measurements the sample was stored in liquid nitrogen. The additional warming up and cooling up cycles may explain the difference in the critical temperatures.

The resistance of the bridge configuration shows a drop around $T = 5.6\,\mathrm{K}$ which is identified with the superconducting critical temperature. A distinct feature before this resistance jump is the slight increase from 132 Ω to 137 Ω around $6.7\,K$. It can be supposed that this effect is based on charge imbalance. Usually, charge imbalance is observed in nonlocal measurements [BWvL04], which for this sample are represented by the dashed curve. The resistance shows very sharp and high spikes, the highest reaching a value of three times the normal state resistance. The peak at 7.3 K shows the typical declining resistance towards lower temperatures, which was described in eq. (3.29) and fig. 3.7.

Compared to the nonlocal setup, the range in which the charge imbalance effects are observed is shifted towards lower temperatures in the bridge configuration. Nevertheless, the distance of the peaks is 1 K in the nonlocal configuration and the range in which the resistance is increased over the normal resistance value extends from 5.8 K to 6.6 K in the bridge configuration, covering a temperature span of 0.8 K. This similar range may hint at charge imbalance being responsible also for the enhanced resistance in the bridge setup.

5.3 Magnetoresistance

The next question that arises is, how the resistance behaves in a changing magnetic field. Therefore measurements were performed using the setup in fig. 4.3b). With the compensation circuit the residual resistance was eliminated so that the sensitivity could be increased, this constant offset was then added again to the measured values so that the real resistance is given in the graphs. The amplitude of the alternating current was $10\,\mu$A during all measurements for the various samples. It oscillated at an frequency of 37.14 Hz. The niobium contacts closer to the bridge were the voltage probes, both for the 606 and the 902 series.

The curves were recorded at different temperatures always starting at the highest value. As the samples 606-2 and 606-6 were situated on the same chip carrier, they were installed simultaneously in the cryostat. Therefore the conditions during the measurement and in particular the angle enclosed with the magnetic field was guaranteed to be the same, making the fluxes through the samples comparable.

5.3.1 Design 1

Magnetic Field In-Plane

First the samples were measurement with the magnetic field applied in-plane, in the direction designated in the inset in 5.2b. The temperature range was chosen relatively close below the resistance steps at 7.25 K in fig. 5.1.

Fig. 5.2 shows the resulting magnetoresistance curves for both samples. For reasons of clarity, only a representative selection of curves is shown. Both graphs have many features in common. The oscillations are not (or only weakly) developed at high temperatures. Within a relatively small temperature span, the amplitude of the oscillations increases and then subsides again at low temperatures. The oscillation periods are 51 mT for sample 600-2 and 65 mT for sample 600-6 at the same angle relative to the magnetic field. It is assumed that the sample plane encloses an unknown nonzero angle with the magnetic field, which during these measurements could not be corrected, as the rotation mechanism for the sample holder was not yet mounted. From the sample geometries one can determine the area of the $Nb/Pd_{95}Fe_5$ bilayers on one side of the pure palladium-iron bridge. The palladium-iron stripe had a total length of $4\,\mu$m and a width of 200 nm. Considering the respective lengths of the bridges, the areas of the bilayers were $0.68\,\mu m^2$ and $0.76\,\mu m^2$. If one supposes that the oscillations are caused by quantum interference effects involving the areas of the bilayers, then the ratio of the oscillation periods of both samples should be the same as the ratio of these areas. The radio of the periods is 0.8 and the ratio of the areas is 0.9. The agreement is not very good, yet it yields the right tendency that the sample with the smaller bilayer area has the higher oscillation period.

Superimposed on the small oscillations there seems to be a larger structure modulating their amplitude and shifting them vertically up and down. In later measurements of differential resistance it will be clarified, that these structures are also quasi periodic.

The complete development of increasing and vanishing oscillations is represented for

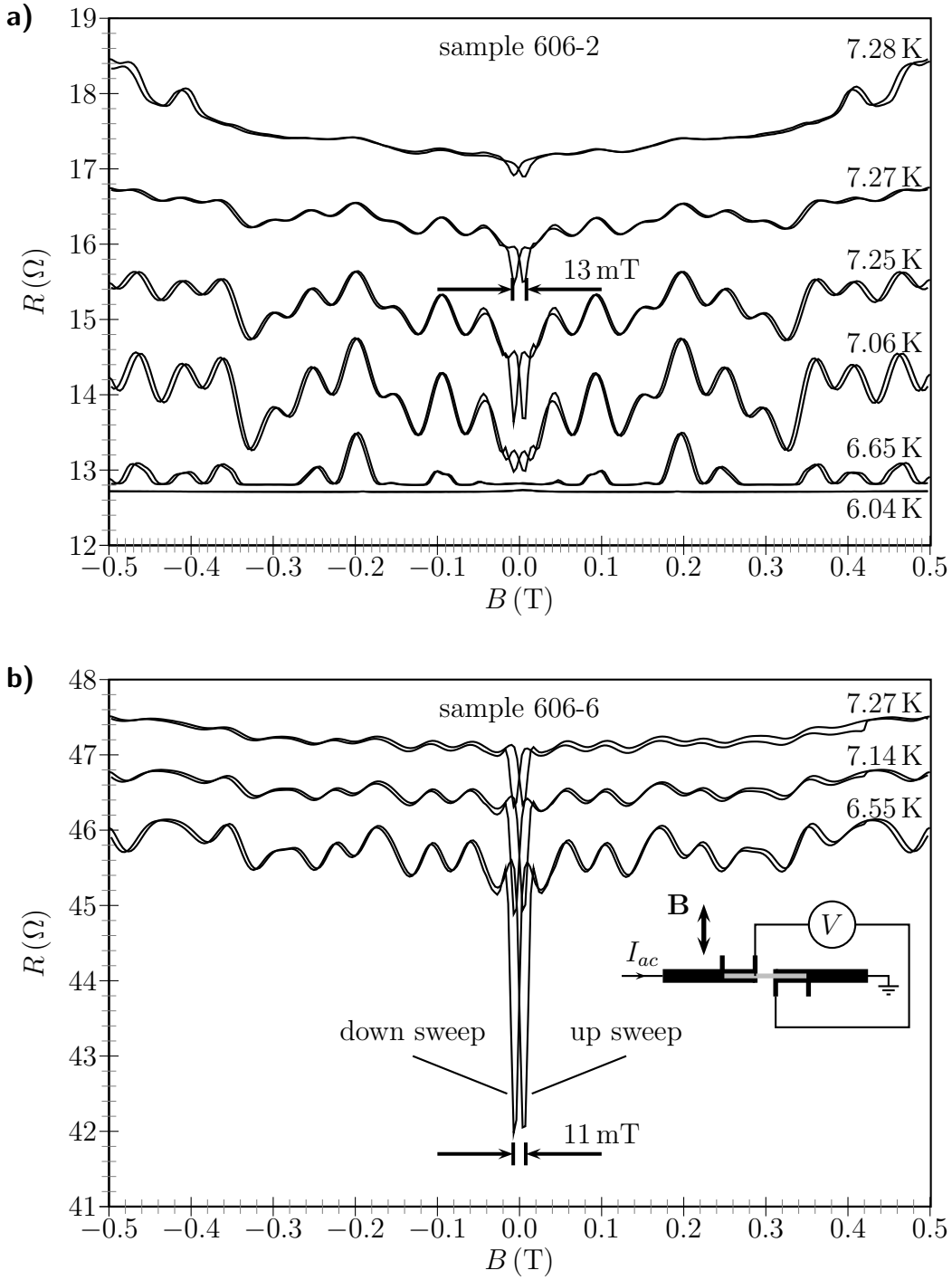

Figure 5.2: *Magnetoresistance oscillations of the samples a) 606-2 (*200 *nm bridge) and b) 606-6 (*600 *nm bridge). The contact configuration together with the in-plane direction of the magnetic field for both samples is sketched as an inset in graph b). For each temperature up and down sweep are plotted. The up sweeps are generally shifted slightly towards higher, the down sweeps to lower magnetic field. The arrows indicate the distance between the central dips.*

sample 600-2. Sample 600-6 in contrast shows very strong central dips with a distance of 11 mT. They are more weakly developed in sample 600-2 where they are 13 mT apart. They appear hysteretically and symmetrically about $B = 0\,\mathrm{T}$. For a sweep from negative to positive magnetic field the dip appears at positive field values, while for the reverse sweep direction it lies on the negative side.

Perpendicular Magnetic Field

The magnetic flux through the sample in parallel orientation is not certain, as the effective flux density is $B_{\mathrm{eff}} = B_0/\sin\alpha$, where α is the angle enclosed by the magnetic field B_0 produced by the coils in the cryostat and the sample plane. It changes considerably for small deviations from the absolute parallel alignment ($\alpha = 0°$). In the perpendicular orientation ($\alpha = 90°$), the variation of the flux with changing the angle is very small. So the uncertainty in the angle is less relevant.

Fig. 5.3 shows the curves obtained in this measurement. Because of the higher flux through the sample compared to the in-plane alignment of the magnetic field, superconductivity is more easily suppressed. This is indicated by the rise of resistance on the high field sides of the curves. Like in the temperature sweep in fig. 5.1, where two resistance jumps were observed, also here one can see the indication of various transition areas, as the slope of the curves changes. At even higher fields, the resistance is almost constant and barely rises anymore. This is visible in the curves for the temperatures of 8.87 K and 7.62 K. Here two plateaus appear for fields higher than 610 mT and 650 mT, respectively, and the same happens for negative magnetic fields. It was confirmed in the experiment that the resistance plateaus extend to higher fields of some Teslas. So all the niobium can be assumed to be normal conducting after the plateau has been reached.

The oscillations at the central area of the curves start to appear only below a certain temperature and increase subsequently in amplitude. The same behavior was observed for the magnetic field in in-plane orientation. The oscillations are very irregular. Nevertheless, they are exactly mirrored about the axis $B = 0\,\mathrm{T}$, if the overlay of the curves for the up and down sweep directions are plotted. What appears on the right hand side of the up sweep appears in reverse sequence on the left hand side of the down sweep and vice versa. This means that, though the oscillations look quite irregular, they are reproducible. A background modulation as observed in the more regular curves in fig. 5.2 cannot clearly be observed here.

5.3.2 Design 2

High Current

With samples of design 2 (c. f. fig. 4.1b), the palladium-iron bridge can be contacted with separate electrodes. Therefore more contact configurations are available. The magnetoresistance measurements shown in fig. 5.4 where performed with two different current paths. For fig. 5.4a it starts at the broad niobium stripes, then crosses the $Pd_{95}Fe_5$ bridge. On the other side of the bridge, the interface is crossed in the reverse

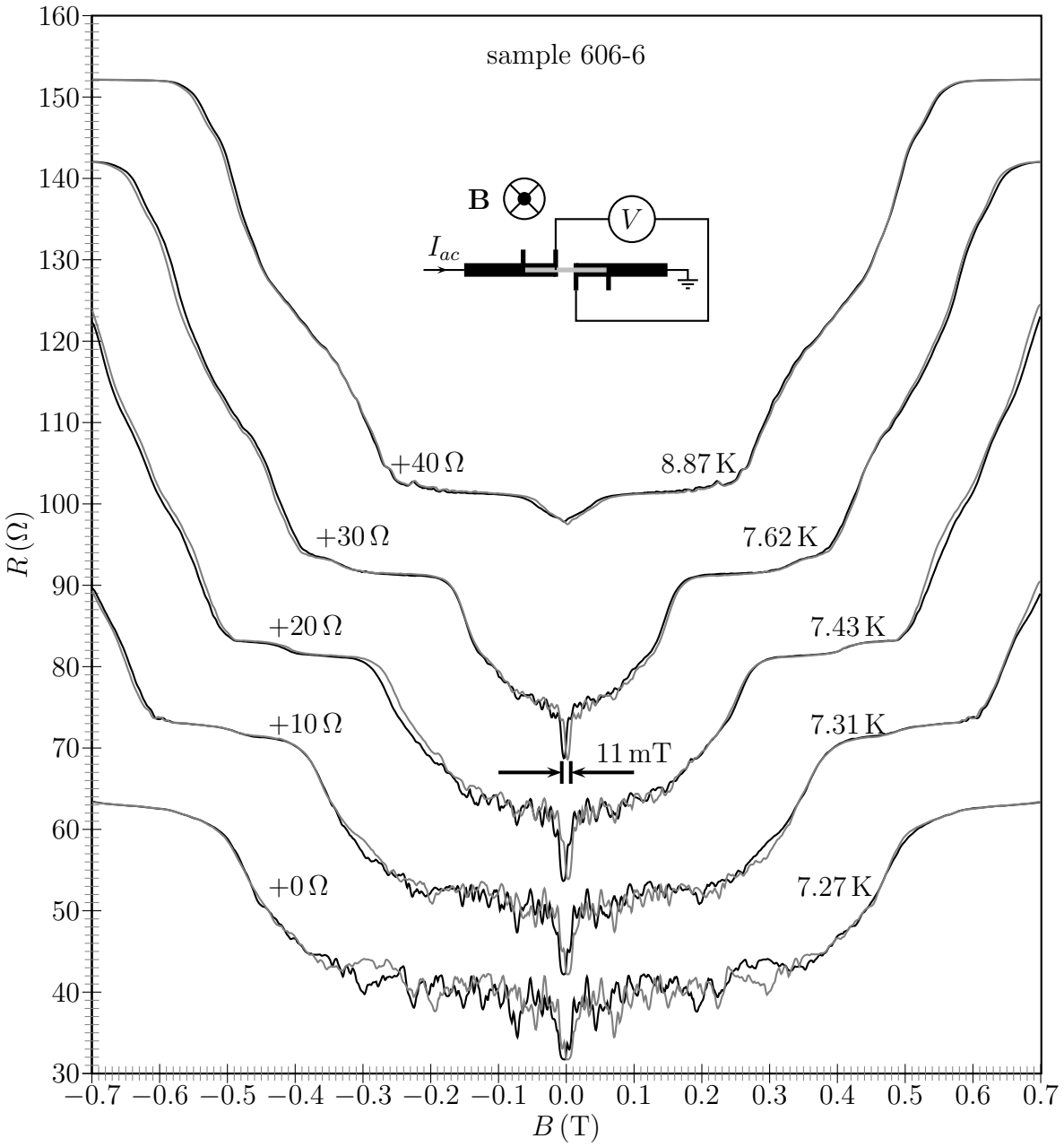

Figure 5.3: *Magnetoresistance oscillations of the sample 606-6. The magnetic field is oriented perpendicular to the sample surface. The curves are shifted in resistance relative to their real positions as indicated on the left side. Both up and down sweeps are plotted for each temperature. The up sweep is plotted in black color, the down sweep is gray. The contact configuration together with the orientation of the magnetic field is shown in the inset.*

direction from palladium-iron back to niobium. This current path is comparable to the one of design 1 one samples. In contrast, the measurement in fig. 5.4b was performed with the current entering right at a palladium iron contact, crossing the palladium iron

bridge and going to ground over a palladium iron lead.

The amplitudes of the oscillations of around 1 Ω are on the same order of magnitude for the sample 902A like for the samples 606-2 and 606-6. In fig. 5.4a the background modulation stands out well, whereas the oscillations are not very pronounced. The central dips around $B = 0\,\mathrm{T}$ are 13 mT apart. Again, there is a mirror symmetry about $B = 0\,\mathrm{T}$. It is broken for 4.2 K and 4.6 K at fields of $-0.4\,\mathrm{T}$ and below and 0.4 T and above. A reason for these deviations may be found in domain switching in the ferromagnetic material while the magnetic field is swept. Further evidence for this is found in the little but abrupt jumps of the resistance curves when such an irregularity ends.

Due to temporary problems with the inset of the cryostat, the temperature could unfortunately not be lowered below 4.2 K, in order to test the complete vanishing of the oscillations like in fig. 5.2a. In fig. 5.4b the oscillations start to subside for the two lowest temperatures, but do not disappear completely. Contrary to the curves in the other graph, the oscillations are here more distinct. The resistances observed in this contact configuration are for the same temperatures higher than in the previous configuration.

The period of the oscillations is 31 mT. This was determined by dividing the measurement range of the magnetic field by the number of local minima in the curves. Only the curves in fig. 5.4b were considered, as the oscillations there are more pronounced. Another remarkable feature of 5.4b is the absence of pronounced central dips. Only a distortion of the oscillation pattern is visible in this range.

Low Current

In the previous magnetoresistance measurements the alternating current had and amplitude of 10 μA. Here now the results for 1 μA and a temperature of 4.2 K are presented. At this low current, the oscillations vanish. Instead of the hysteretic dips, broader peaks at $B = 0\,\mathrm{T}$ developed, see fig. 5.5. The behavior is the same for both contact configurations. In the upper graph marked with "Nb contacts", a spike appears at -80 mT for the up sweep and at 80 mT for the down sweep. In the lower graph titled "$Pd_{95}Fe_5$", these spikes are absent. Already in fig. 5.4 the upper graph a) showed more irregularities. So this contact configuration seems to be more sensitive to the domain switching which was there supposed to be the reason for the breaking of the symmetry at the outer parts of the curves.

The resistance during this sweep cycle slowly sank. This is explained by a slight temperature drift. The difference between the initial resistance at $-0.6\,\mathrm{T}$ and the final resistance is 20 mΩ. This corresponds to temperature which was at the end of the sweep cycle by an estimated 10 mK lower than at the beginning.

Degradation

Fig. 5.6 shows the comparison of magnetoresistance measurements done at the same sample with an interval of one week. The solid curve is taken from fig. 5.4a. It is the up

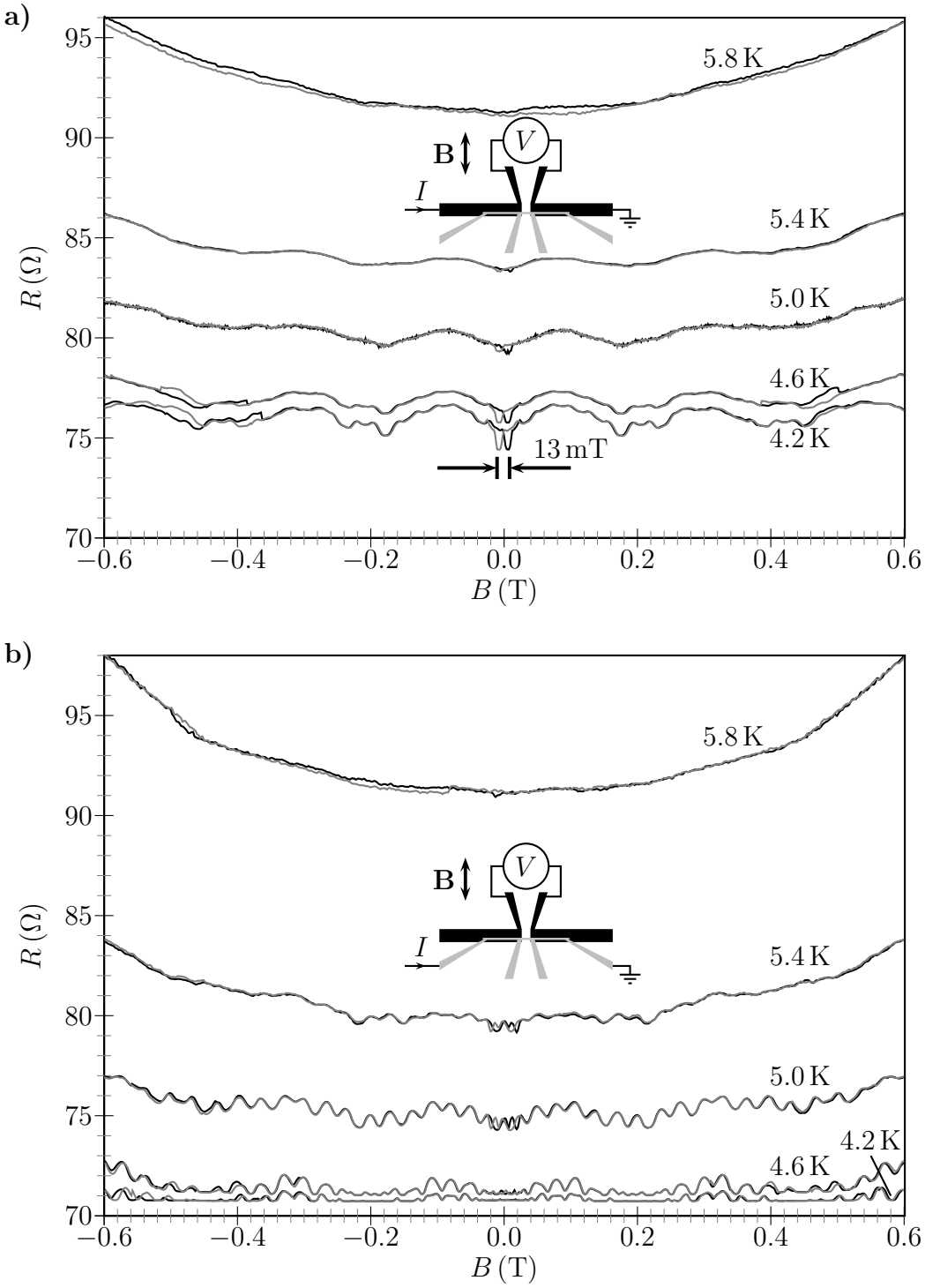

Figure 5.4: *Magnetoresistance oscillations of the sample 902A at various temperatures. a) The alternating current of* $10\,\mu A$ *is sent through niobium contacts, b) The current enters and leaves the sample through the* $Pd_{95}Fe_5$ *leads. The up sweep data is shown in black, the down sweep curves in gray. The inset shows the contact configuration and the direction of the magnetic field.*

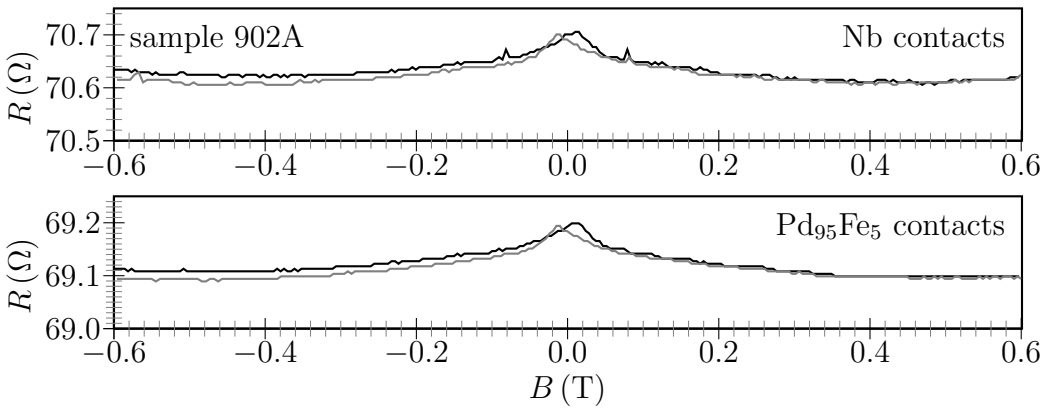

Figure 5.5: *Magnetoresistance for low alternating current $I_{\mathrm{ac}} = 1\,\mu A$ at $T = 4.2\,K$. For the contact configuration see fig. 5.4. The black line indicates the up sweep, the gray line the down sweep.*

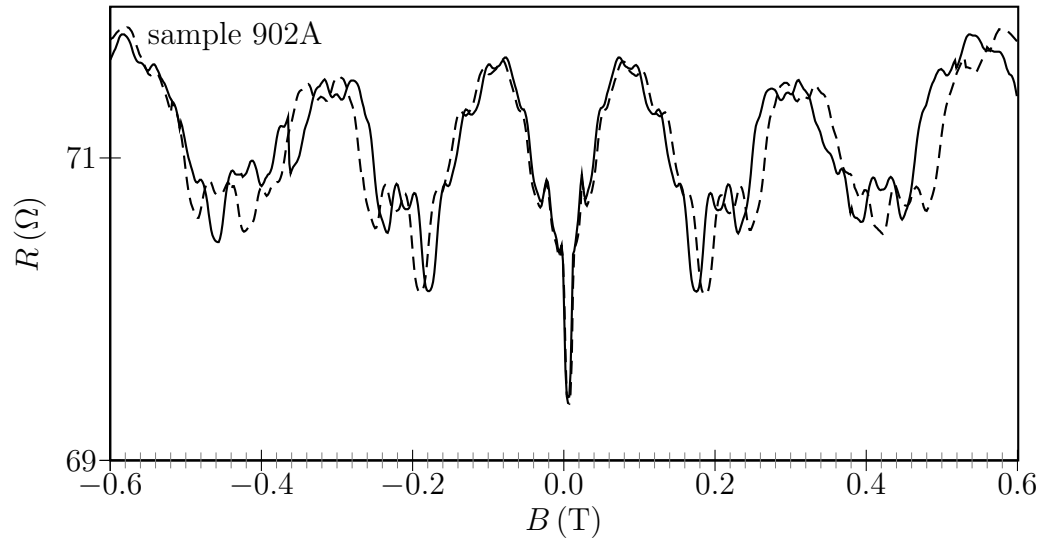

Figure 5.6: *Magnetoresistance of sample 902A measured at an interval of one week. The later measurement is plotted as a dashed line. The temperature was* $4.2\,K$ *and the current was injected at the niobium leads, c. f. 5.4a.*

sweep curve for 4.2 K. The other one (the dashed curve) was performed one week later under exactly the same conditions. The sample was kept cold in the cryostat during this period.

The central regions are quite well in accordance. The outer parts, on the other hand, deviate. This comes about by two effects. First, the curve for the later measurement is increasingly stretched towards higher magnetic fields on the positive side and towards lower values on the negative side. There are some possibilities to explain this. Either the magnetic coils in the cryostat had changed, so that a different magnetic field is produced for the same current. Or the calibration of the power supply had changed. A further possibility is some change of the sample, i. e. its geometry. What is most likely, is a

slight change of the orientation of the sample in the magnetic field. Sec. 5.5 describes the connection between the periodicity of the oscillations and the tilt of the sample.

If this stretching is disregarded, then the curves match well up to 0.3 T on the positive and up to -0.4 T on the negative side of the plot. On the outer parts of the curves, the magnetic domains influence again the course of the resistance.

Therefore, in summary, degradation during the time of the measurement can be ruled out, if the samples are kept at low temperatures.

5.4 Differential Resistance

Before investigating further the origin of the magnetoresistance oscillations of the preceding section, a review of the measurement technique, which was described in sec. 5.3, seems to be appropriate. This consideration gave the incentive for measuring the differential resistance.

An alternating current of some μA was applied in the magnetoresistance oscillations. If this sinusoidally oscillating current of the form $I(t) = I_0 \sin \omega t$ is sent through the sample, it scans the electrical properties in a range from $-I_0$ to $+I_0$. I_0 is the amplitude of the current. The lock-in amplifier measures a certain frequency component of the voltage response $U(t)$ of the sample. This signal is only sinusoidal, i. e. $U(t) \propto I(t)$, if the sample shows ohmic behavior over the whole range that the current scans. In this case, the value measured by the lock-in amplifier is exactly the amplitude of the voltage signal.

If the sample is non-ohmic, then the form of the voltage signal deviates from a sinus. Such a signal is a composition of sinuses and cosines of the base frequency and higher harmonics. A lock-in amplifier usually only detects the base frequency. (It can be operated in a mode that measures the higher harmonics, though.) So a non-sinusoidal response signal from the sample will only show the amplitude of this Fourier component.

Another effect that must be regarded is, that the signal might not lie symmetrically about the zero voltage line or has different shapes on the negative and positive side for a non-ohmic sample. This imbalance of the signal will also influence the voltage amplitude seen by the lock-in amplifier.

While controlling the voltage response of the samples during the magnetoresistance measurements on an oscilloscope, it was both observed as being non-linear and asymmetrical about 0 V. By changing the magnetic field, also the shape and the amplitude changed in accordance with the magnetoresistance oscillations.

The determination of I–V characteristic of the sample at different magnetic fields would provide some insight into the nonlinear behavior of the sample. In this work, however, it was not measured directly. The measurement of the differential resistance provides a very sensitive tool to measure non-ohmic I–V characteristics, as changes in resistance are recorded rather than the resistance itself. Also, the signal to noise ratio is improved, as in order to obtain the I–V characteristic, the data of the $\mathrm{d}V/\mathrm{d}I$ measurement is numerically integrated. This eliminates a considerable fraction of the noise.

To obtain the differential resistance from the resistance in the reverse direction is not feasible, as the noise in the I–V characteristic is even enhanced, if the data is differentiated numerically. It is sometimes favorable to look at the differential resistance, as it contains more direct information about, e. g. the density of states, c. f. sec. 3.2.

The increased signal to noise ratio has to be payed with measurement time. Usually a direct measurement of the I–V characteristic can be made within seconds or even milliseconds. The measurement of the differential resistance involves a lock-in amplifier with a certain time constant that does not allow the signal to change arbitrarily rapidly. The measurement times, in this case, range from about one to several few minutes for one characteristic.

5.4.1 Bridge Configuration

At first the same structures in the same contact configuration as in sec. 5.3 where investigated using the differential resistance method described in sec. 4.2.1.

These measurements provided some deeper insight into the structure of the magnetoresistance oscillations. Beginning with analyzing single scans of differential resistance at fixed magnetic field, those scans were finally recorded at a series of equally spaced values of magnetic field to produce a map of differential resistance depending on magnetic field and current. By this, the symmetry of the oscillations, the dependency on the sweep direction of the magnetic field and on temperature could be reproduced.

Single Scans

The data obtained from sample 902A is displayed in fig. 5.7a. The current sweep direction is irrelevant, as both the up and down sweep produce the same result. The differential resistance shows some remarkable behavior. The three curves are completely different for the three magnetic fields. There is a valley around zero current with a differential resistance of $69.4\,\Omega$. In this region, the $V(I)$ curve must be linear and therefore ohmic. At the measurement temperature of 4.2 K, all niobium should be superconducting. Then the only resistance left is the one of the normal conducting $Pd_{95}Fe_5$ bridge.

This valley is not symmetric about $I = 0\,\mu$A and its width varies considerably from one curve to the other. Also the peaks on the sides of the valley once appear on both sides and once only on one. The height is also very different. As the magnetic field at which the curves were recorded only varies by some 10 mT, there is a strong dependence on magnetic field.

Fig. 5.7b is the numerically integrated data of the differential resistance. This I–V characteristic is weakly nonlinear. On top of a linear background, two kinks can be found at the current values where the peaks are situated in the top picture. In comparison, the differential resistance measurements render this nonlinearity much more visible. The inset represents the same data with the linear background subtracted.

Another feature is given by the different values of differential resistance in the outer region of the curves between approximately $10\,\mu$A and $15\,\mu$A and its negative counterpart. The height depends on the width of the plateaus in the middle of the curves. The

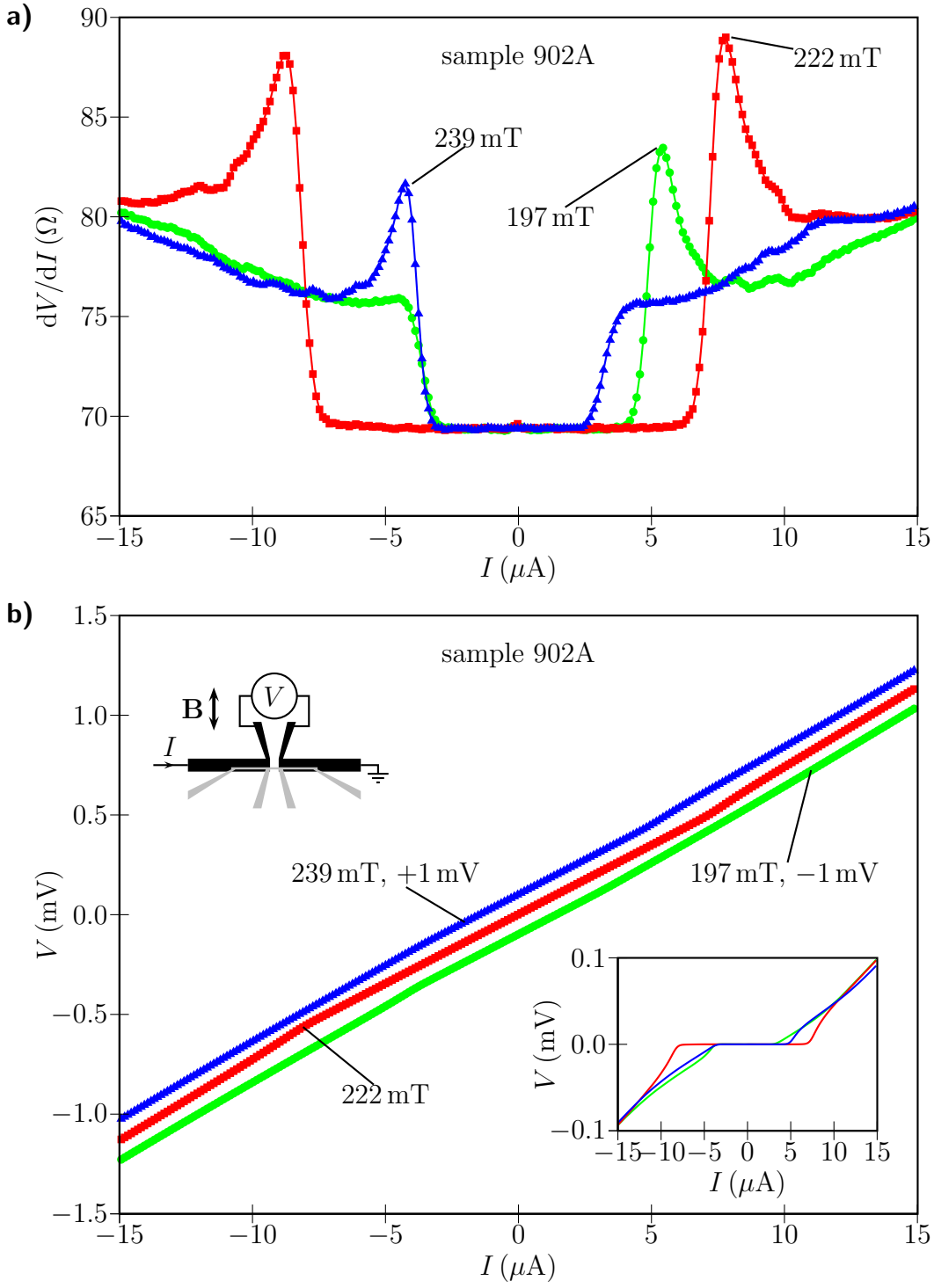

Figure 5.7: *a) Differential resistance (measurement), b) I–V characteristic (integral of differential resistance) of sample 902A at 4.2 K and in-plane magnetic field. The oscillating current applied was* $\mathrm{d}I = 0.1\,\mu A$*. The ramp current was swept from negative to positive values. In b) the curve for* 239 *mT is shifted* 1 *mV up and the one for* 197 *mT is shifted down the same amount. Inset: The same curves as in b) with the linear background subtracted.*

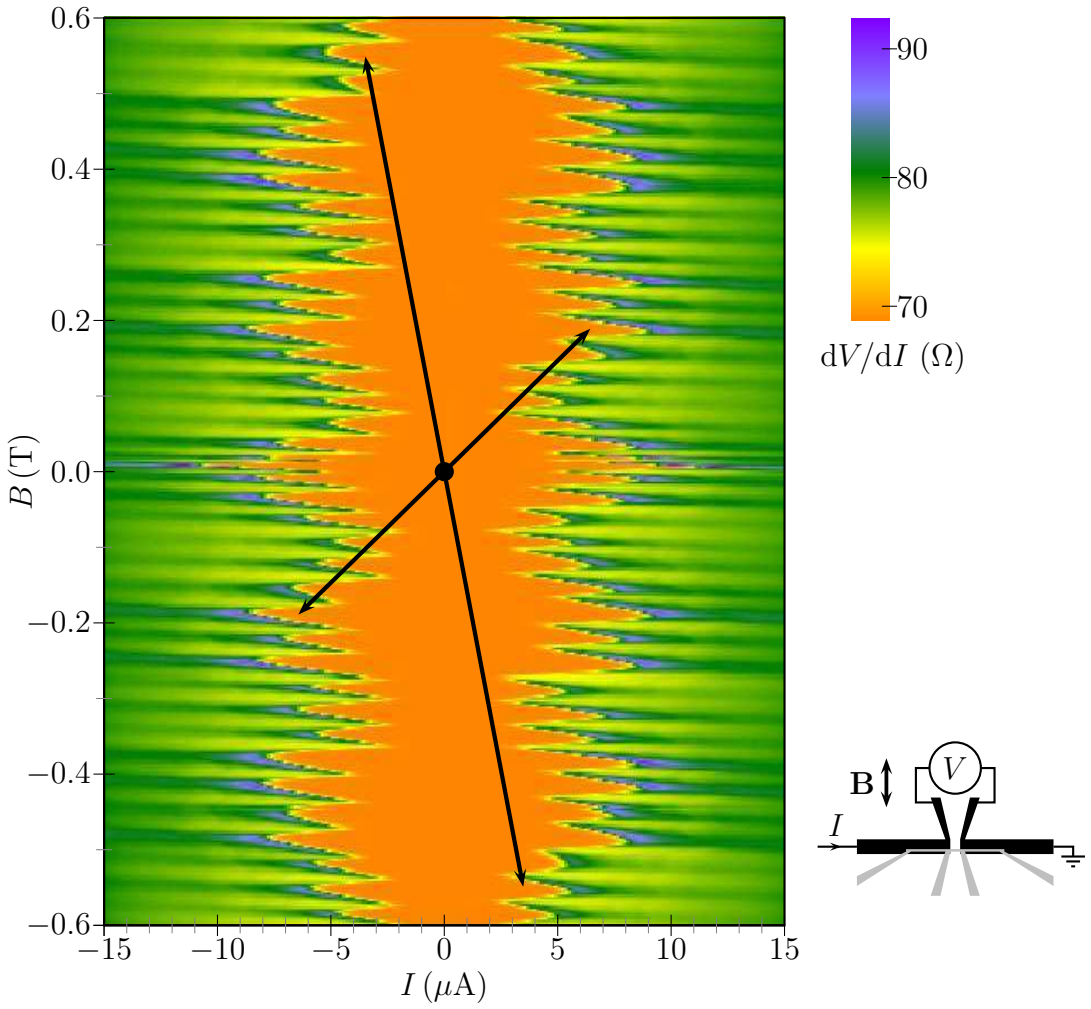

Figure 5.8: *Color coded image plot of differential resistance of sample 902A measured over the $Pd_{95}Fe_5$ bridge at a temperature of 4.2 K. The contact configuration includes the bridge in the voltage measurement. The sweep direction of the magnetic field applied in-plane was from −0.6 T to +0.6 T. The dot at $B = 0\,T$ and $I = 0\,A$ indicates the symmetry point. The arrows help to clarify the point symmetry of the graph.*

broader the plateau is, the higher is the differential resistance in these regions. This supposition will be affirmed by the image plots.

Color Scale Plots

The single scans in the previous section suggest that the behavior of the differential resistance is strongly dependent on magnetic field. This correlation was investigated more closely. The line scans at regularly distributed magnetic fields are plotted in fig. 5.8 with color coded differential resistance.

A striking feature of this plot is the regularity of the pattern that evolves during the change of the magnetic field. The valley (orange) around zero current has a rim

(yellow) at which the differential resistance rises abruptly. From the single line scans we know, that this happens at points which are mostly not symmetric about $I = 0\,\mu\mathrm{A}$ in accordance to the picture here. The rim has bulges extending to larger (or on the negative side smaller) currents. Their form resembles a SQUID interference pattern as described in sec. 3.6. The typical damping of a Fraunhofer interference pattern for an extended S/N/S weak link cannot be seen here. These bulges do not exactly occur at a fixed interval, but their distance varies slightly from one to another. The mean period is 32 mT, fitting the period obtained from the magnetoresistance measurements for this sample in sec. 5.3.2. The bigger oscillations, which also were already observed there, appear in this image plot again and have the same characteristic distance of approximately 220 mT.

Although the single line scans look quite asymmetric, this plot reveals a point symmetry about zero magnetic field and current, which is valid for both the smaller and bigger oscillations. The point of symmetry is indicated by a black dot in the plot. The black double arrows point at regions at which this symmetry is particularly easily perceived. At both ends of the arrows, the sequence and the form of the bulges is exactly mirrored taking into account the reflection at the $B = 0\,\mathrm{T}$ axis.

The single scans in fig. 5.7 had two peaks on both sides of the valley. In some cases, the peaks appeared only on one side and in others also on both sides. In the color coded plot in fig. 5.8 those peaks can be found close to the farthest extension of a bulge, designated by blue-violet color due to the high differential resistance. A thorough look reveals that the blue-violet regions occur only at one side of the bulges with respect to magnetic field. For $I > 0$, these regions of high differential resistance are situated on the side directed towards higher magnetic field, for $I < 0$ they show up on the side directed towards lower magnetic field. Due to the whole picture being point symmetric and not axially symmetric, those regions do not appear at the same magnetic fields, but they are displaced relative to each other. So a peak on one side may face a less or not at all peaked region on the other side.

Temperature Dependence

The magnetoresistance oscillations showed a distinct temperature dependence, which manifests itself also in the color scale plots of differential resistance. This is displayed in fig. 5.9 for a temperature range from 4.2 K to 6.6 K.

The images show a narrowing of the valley of constant differential resistance with rising temperature. The color scale spans the same values for all plots, allowing a comparison of the measured data. The color change of the valley regions of the five plots reveals that the differential resistance increases linearly with temperature. The characteristic pattern, however, persists up to 6.6 K, where it is still, even though faintly, visible.

The single line scans in fig. 5.10, taken from the color scale plots at $B = -165\,\mathrm{mT}$, show the temperature dependency very clearly. The shrinking of the valley width and the simultaneous lifting of its bottom is illustrated. It cannot, however, be excluded, that the variation in the valley width is also caused by a shift of the pattern, which is indicated by the variation of peaks nearby the valley for every temperature. For 4.2 K,

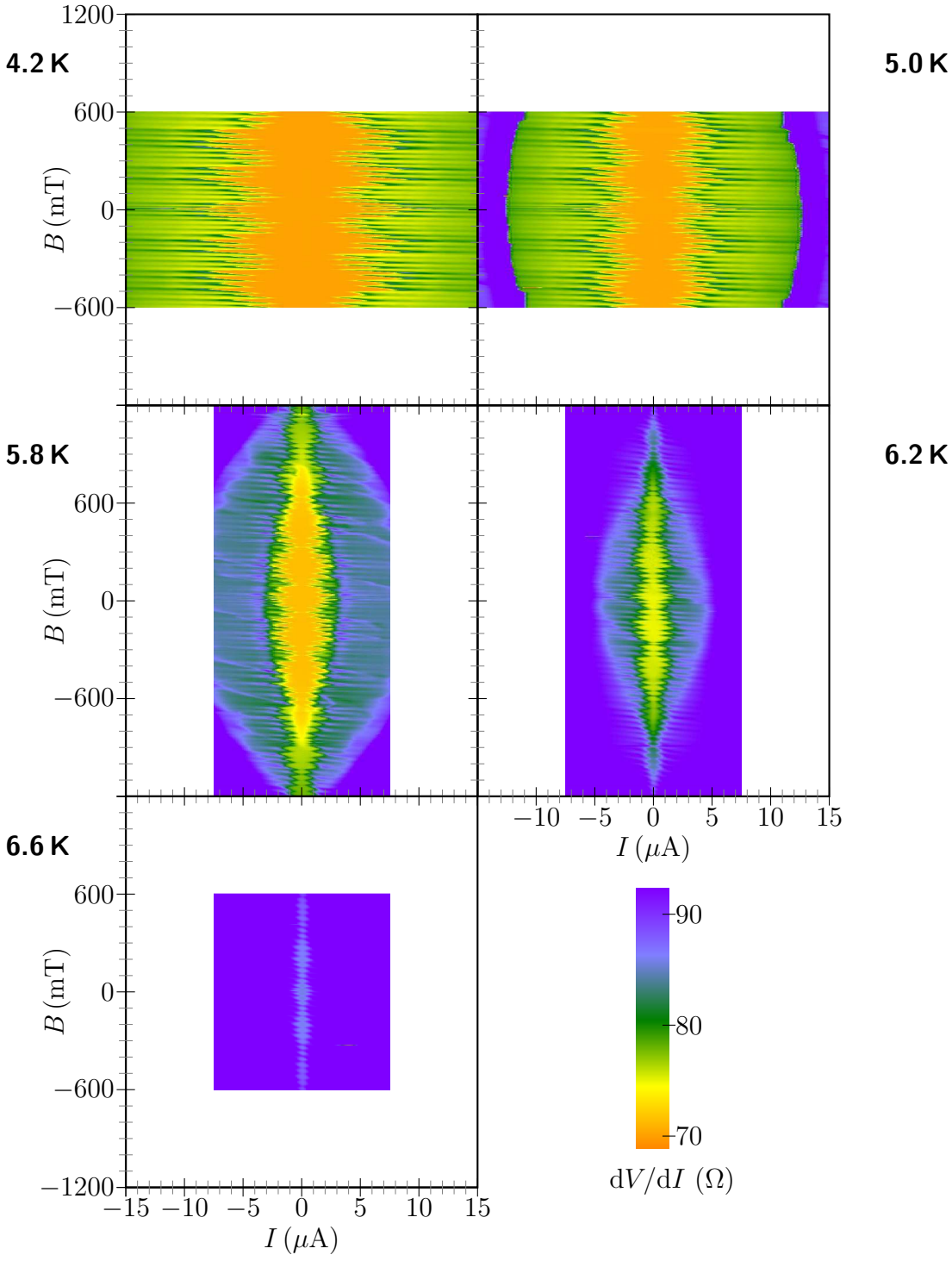

Figure 5.9: *Temperature evolution of the differential resistance pattern for sample 902A in bridge configuration. The sequence of the temperatures was from* 4.2 *K to* 6.8 *K. For reasons of contrast, the color scale is truncated at* 94.2 Ω*. The in-plane magnetic field and the current were swept from negative to positive values in all plots. For the contact configuration see fig. 5.8.*

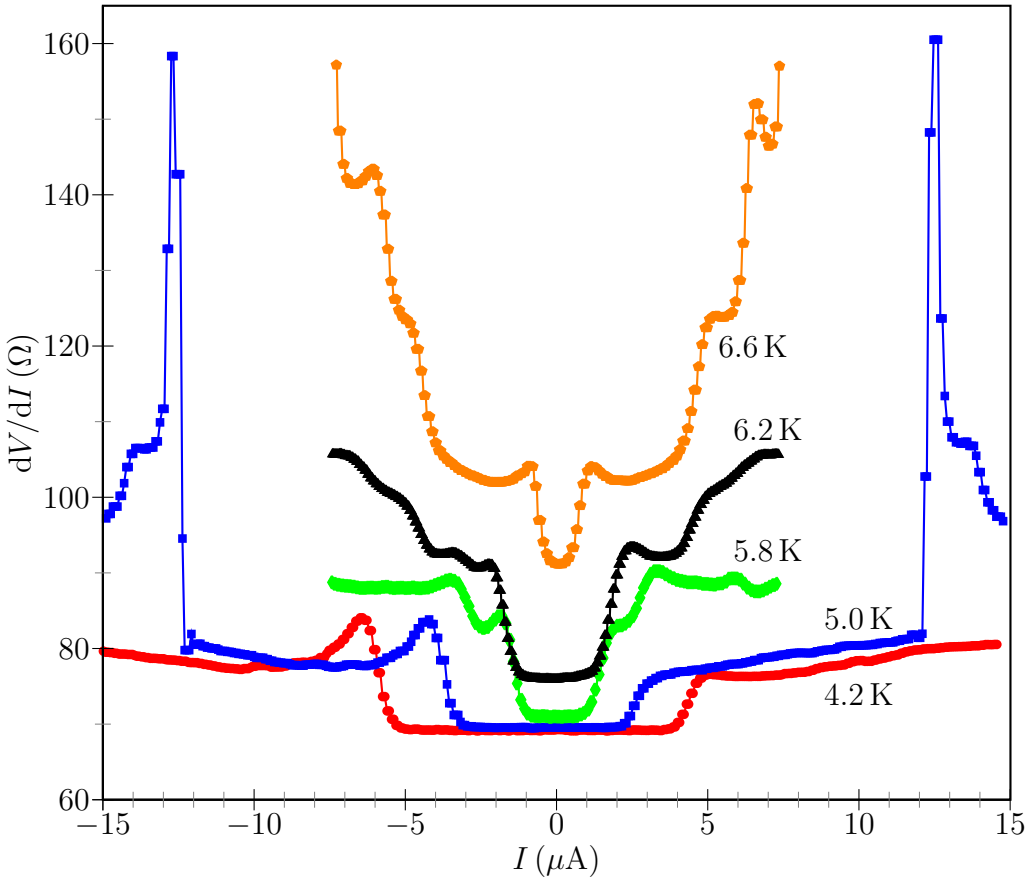

Figure 5.10: *Single differential resistance curves at various temperatures taken from the image plots in fig. 5.9 at $B = -165\,mT$.*

5.0 K and 5.8 K they are asymmetrical, for 6.2 K and 6.6 K, both peaks show the same height.

The differential resistance in areas outside the central valley regions also increases with temperature. A remarkable feature is the abrupt jump to high values that appears in the plot for 5.0 K. This high differential resistance region is absent at 4.2 K. At higher temperatures this jump does not occur, as it does presumably lie outside the measurement range.

Besides the temperature, also the magnetic field gives rise to a narrowing of the valley fig. 5.9. Starting with the temperature 5.8 K, the valley is constricted for high magnetic fields. This effect is continuously strengthened for the higher temperatures 6.2 K and 6.6 K. Again, this is a strong indication, that the differential resistance of the valley reproduces the bridge resistance.

In order to test for a change of periodicity and the change of position of the hysteretic peak, plots of the rim of the valley, were made in fig. 5.11. The current values at the rim of the values shall be called critical current. Later, in the section where the measurements in nonlocal contact configuration are presented, and in the discussion

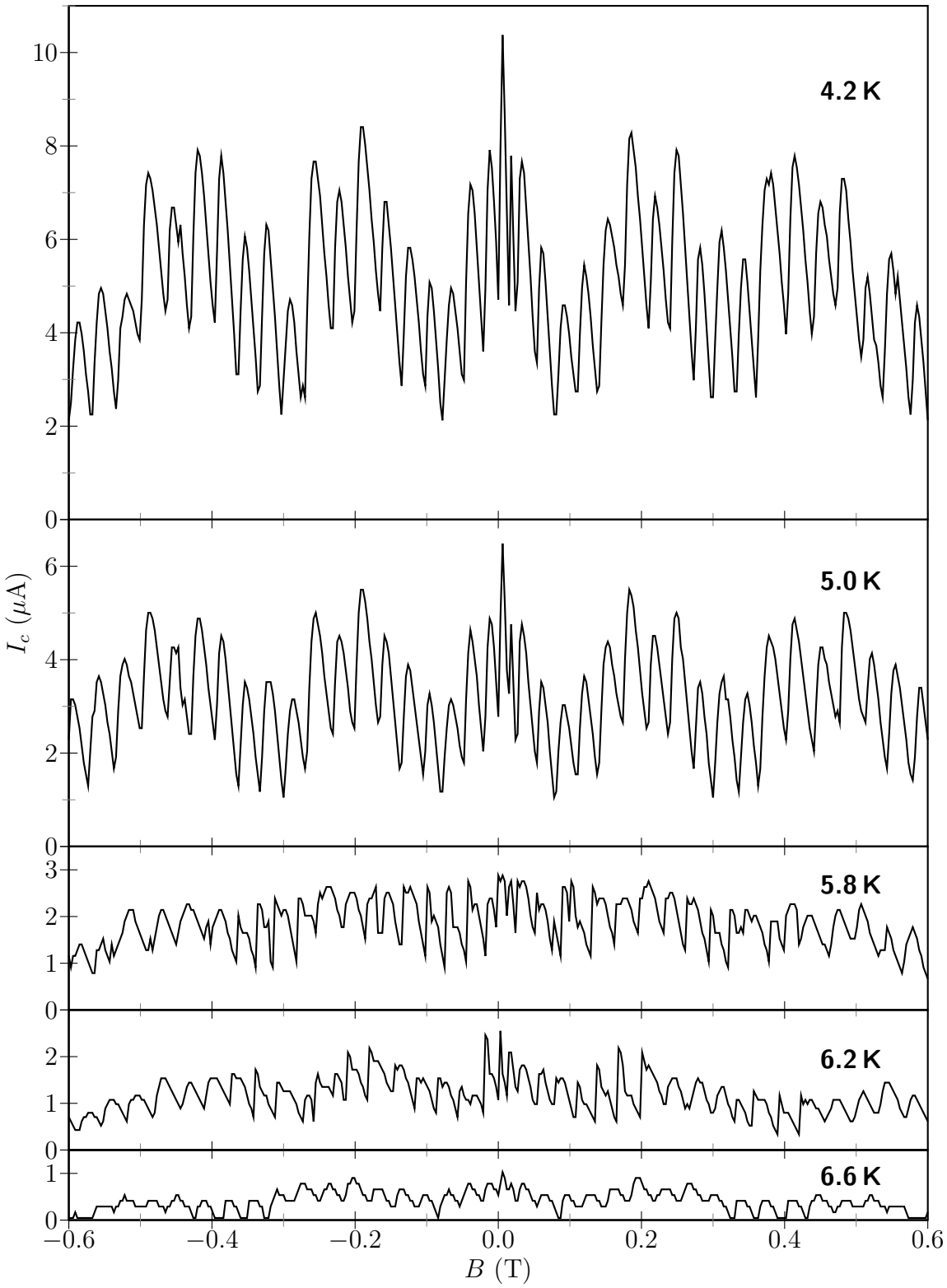

Figure 5.11: *Contours of critical current I_c as determined from fig. 5.9. They trace the rim of the valley of constant differential resistance in those plots. The temperatures within each frame linking these curves with the image plots in fig. 5.9.*

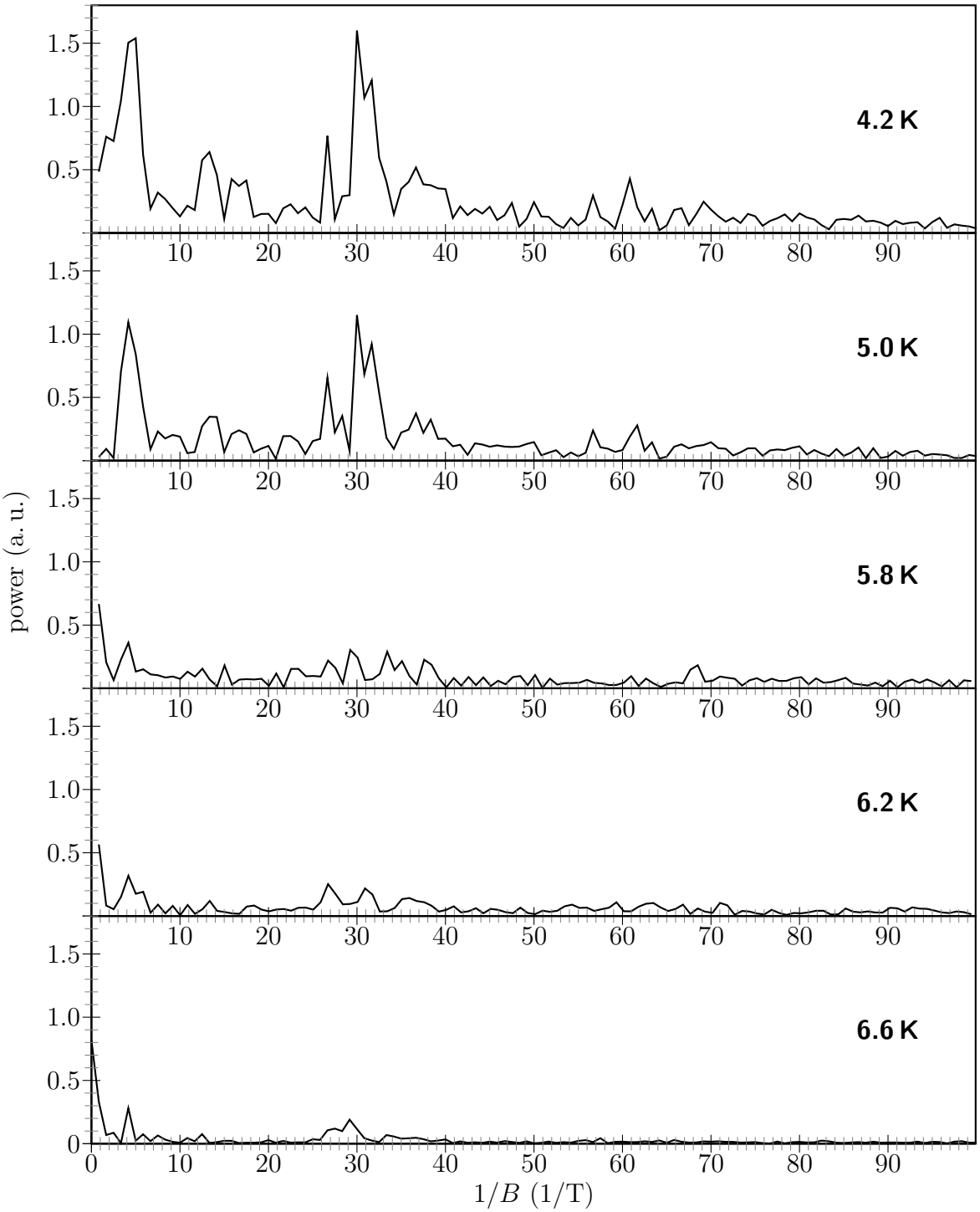

Figure 5.12: *Discrete Fourier transform of the critical current contours in fig. 5.11. The transform was done without any apodization. The unit of power on the abscissa is arbitrary, but the relative height of the peaks is preserved.*

chapter, this name will be made clearer. The curves shown reproduce many of the characteristics of the magnetoresistance oscillations, like the small oscillations which are modulated by a larger oscillation and a peak at around 0 T. The general decrease of the critical current with increasing temperature and also the diminution of the amplitude of the oscillations can also be observed.

A discrete Fourier transform of this data, which is given in fig. 5.12, reveals more details about the frequencies involved. There are three frequency groups. The two groups with the highest power lie at around $3.9\,\mathrm{T}^{-1}$ and $30\,\mathrm{T}^{-1}$. The other group of frequencies with much lower power is located in the vicinity of $14\,\mathrm{T}^{-1}$.

This representation is linked with fig. 5.11: The large oscillation with a period of 260 mT is associated with the frequency group at $3.9\,\mathrm{T}^{-1}$, while the smaller oscillations are connected with the frequency cluster at $30\,\mathrm{T}^{-1}$. The frequency of $14\,\mathrm{T}^{-1}$ corresponds to a period of 71 mT, which encompasses two or three periods of the shorter oscillations. Due to the low intensity of this frequency group, this modulation is not pronounced and cannot be perceived in fig. 5.11. The appearance of groups of frequencies was expected, as the oscillation peaks are neither in the magnetoresistance oscillations nor in the graphs of critical current equally spaced. The periods given in the framework of the magnetoresistance oscillations represent an average value.

Another observation can be made at the Fourier transform in fig. 5.12: The temperature groups are split into many frequencies at 5.8 K and also at 6.2 K. This behavior is reflected in the critical current graphs by irregularities, which emerge at these temperatures. It is unclear whether also at 6.6 K these jumps, spikes and shifts are present, as the resolution of the current was very low, which is indicated by the visible steps in the critical current curve.

A comparison of the powers of the more prominent frequency peaks at $3.9\,\mathrm{T}^{-1}$ and at $30\,\mathrm{T}^{-1}$ is given in fig. 5.13a). Going from lower temperatures to higher ones, the powers simultaneously decrease fast, whereas for 5.8 K to 6.6 K, they stay approximately at the same level. Both peaks have almost the same height for all temperatures. A different picture is shown in fig. 5.13b). Here, the mean of the critical current curves in fig. 5.11 is plotted against temperature. This mean was retrieved from the value of the Fourier transform at $0\,\mathrm{T}^{-1}$, which is not shown in the graphs above in order to keep them clear. Compared to subfigure a), this graph shows a much steadier decrease with temperature and in particular no saturation above 5.8 K.

Symmetry Of The Critical Current

In fig. 5.8, the point symmetry of the image has been pointed out. Here this fact shall be examined further. Therefore, the graph of the critical current at 4.2 K was taken for both the negative and the positive current side. Then two overlays were made, as shown in 5.14. Subfigure a) shows the overlay of the positive critical current with the graph of the negative critical current whose sign was reversed, i. e. mirrored about the $I_c = 0\,\mu\mathrm{A}$ axis. Subfigure b) shows the superposition of the point mirrored curve of the negative current side with the one at the positive current side. The mirror point was $B = 0\,\mathrm{T}$ and $I = 0\,\mu\mathrm{A}$.

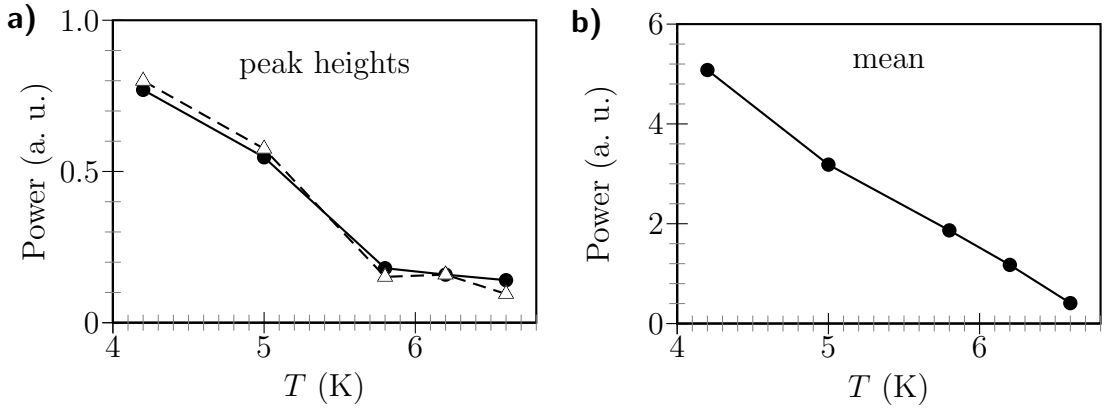

Figure 5.13: *a) Powers of the frequency peaks at 3.9 T^{-1} (filled dots) and at 30 T^{-1} (hollow rectangles). The corresponding solid and dashed lines serve as guide to the eye. b) Representation of the mean of the critical current graphs in fig. 5.11. Again, the line is just a guide to the eye.*

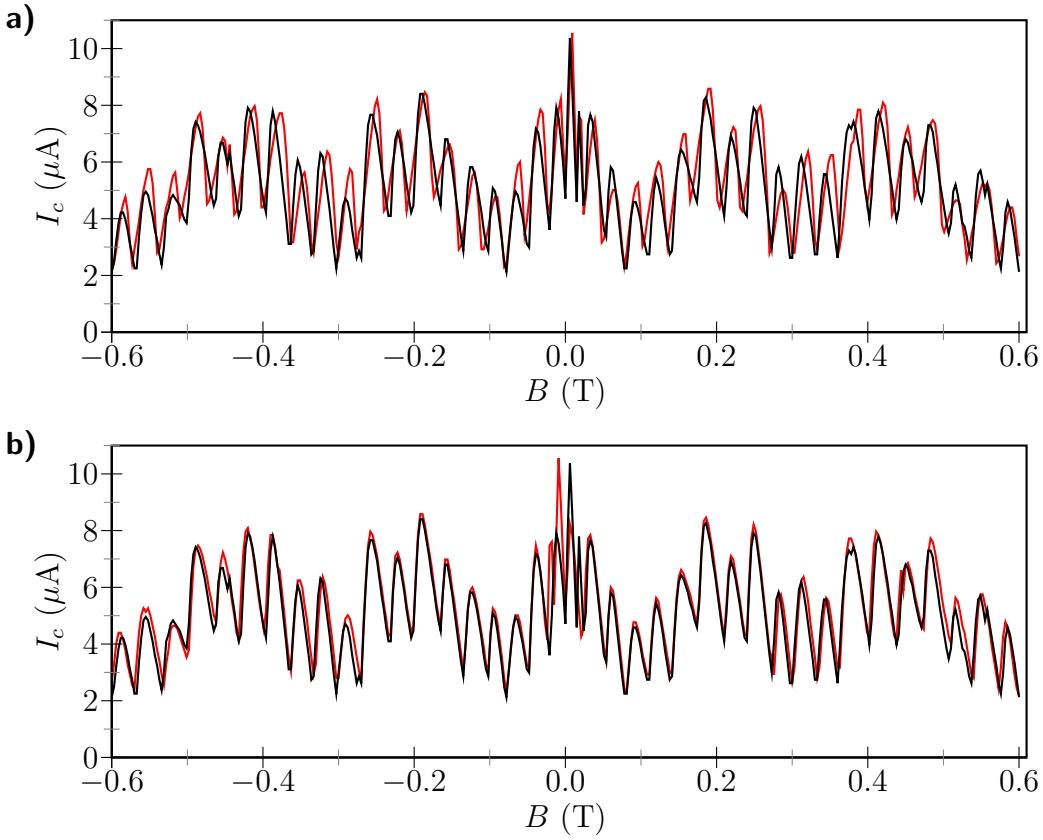

Figure 5.14: *Overlay of the positive (black) and negative (red) critical current curves at 4.2 K for different symmetry operations. a) The sign of the curve for negative critical currents is reversed (axis mirrored). b) The same curve is point mirrored at the point $B = 0$ T, $I_c = 0\,\mu A$.*

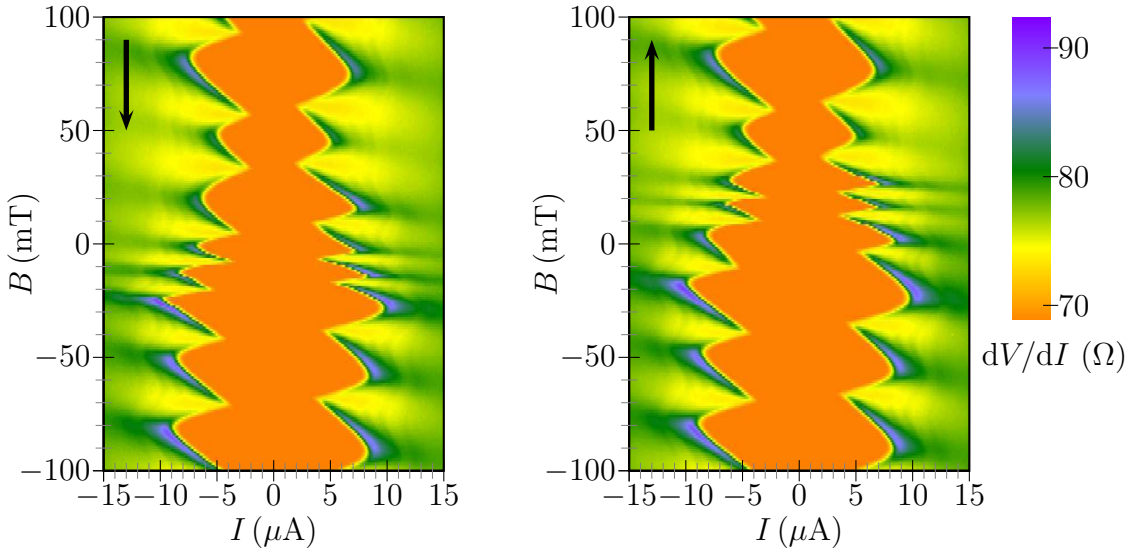

Figure 5.15: *High resolution scans of the central region measured with the same parameters as in fig. 5.8. The two sweep directions of magnetic field are indicated by the arrows. The data of the left picture was taken in the down sweep direction, the right picture shows the result of the up sweep.*

The axis mirrored curve (red) in subfigure a) has the oscillations at quite accurately the same places as the unmirrored curve (black). Also the heights of the peaks of the red and black curve deviate by a small amount. There is a slight inclination of the peaks, pointing to the right for the mirrored curve and to the left for the unmirrored one.

A by far better congruence is reached, if the point mirrored negative current side is superimposed on the curve for the positive current, see 5.14b. The peak heights, their positions and the inclination are the same. The only difference consists in the central region about 0 T, where the two highest peaks are separated, which is clear, as, in the unmirrored case they were found at the same nonzero magnetic field. Also, there is a small satellite peak, found at the right for the black and to the left for the red curve, which does not have a corresponding peak. This affirms the point symmetry of the effect, which was pointed out in fig. 5.8 already. If both magnetic field and current are reversed, then the system behaves the same.

Both, fig. 5.14a) and fig. 5.14b) are representative for the other temperatures.

Hysteretic Behavior

In the plots of magnetoresistance oscillations in sec. 5.3, peaks around $B = 0\,\mathrm{T}$ were observed, whose exact positions were depending on the sweep direction of the magnetic field. The critical currents in fig. 5.11 and fig. 5.14 also show a peaked value in this region. Apparently, the peaks and the hysteretic behavior should manifest themselves also in the color coded plots of differential resistance. Fig. 5.15 displays the result of an investigation of that feature. The two images were obtained by sweeping the magnetic

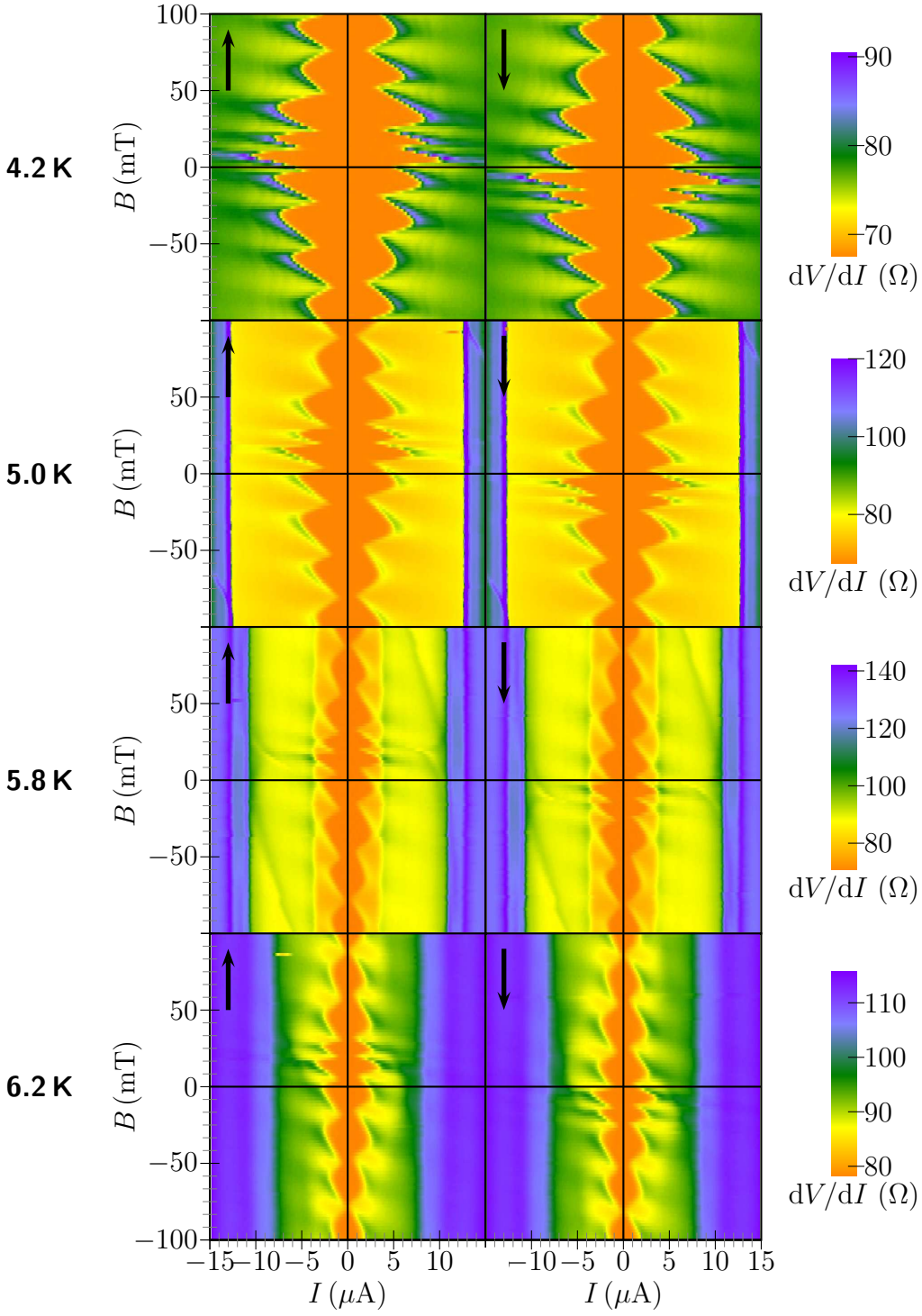

Figure 5.16: *Temperature evolution of the hysteretic structure of sample 902A in bridge configuration. The sequence of measurement of the temperatures ranged from 4.2 K to 6.2 K. For reasons of contrast, the color scale is truncated and adjusted. The in-plane magnetic field and the current were swept from negative to positive values in all plots. For the contact configuration see fig. 5.8.*

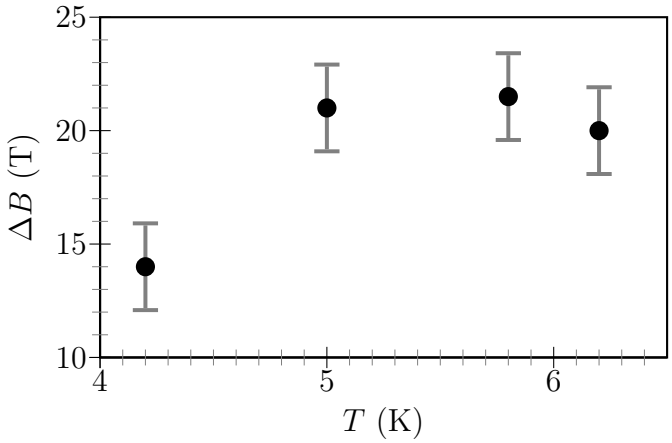

Figure 5.17: *Distance of the central peaks of the two sweep direction of magnetic field extracted from fig. 5.16. The error bars result from the width of the magnetic field steps.*

field from +100 mT to −100 mT (down sweep) and back again to +100 mT (up sweep). Apart from the known pattern with the expected periodicity of around 30 mT, regions of reduced periodicity appear. Depending on the sweep direction of the magnetic field, such a distorted region is located on the side with negative values of magnetic field (down sweep) or on the side with positive magnetic field (up sweep). In both these images, a pronounced peak like in fig. 5.8 is absent.

If the limits of the sweep range, however, are extended from −100 mT and +100 mT to −600 mT and +600 mT, then the central peaks appear again, like in fig. 5.16. Here the temperature evolution of the central region in the range from −100 mT to +100 mT for the two sweep directions is displayed. Before a sweep was started at −100 mT or +100 mT, the magnetic field was driven to −600 mT or +600 mT, respectively, and then increased or lowered monotonically to the starting point. This guaranteed the same height of the central peak as in fig. 5.8.

From these image plots the critical current contour was extracted and from plots similar to 5.11 the values of the magnetic field at the maximum of the highest peak were determined for the up sweep and the down sweep direction. The temperature dependent distance of the peaks is shown in fig. 5.17. Except for 4.2 K, the peaks are separated by 20 mT from each other. The distance for 4.2 K is 14 mT.

It is also very difficult to measure to much lower temperatures, as the straight lines at high current, which correspond to peaks like in the curve for 5.0 K in fig. 5.10, lead to a distortion of the interference pattern, which is shown in sec. 5.4.3 about the nonlocal measurements. The migration of those line influences the position of the central peaks very strongly. This finding may also explain the deviation of the data point at 4.2 K.

5.4.2 Contact Configurations

There is still the question, where the effects originates locally. Is it an effect of the PdFe bridge? To clarify this problem, different contact configurations were tested. Sample

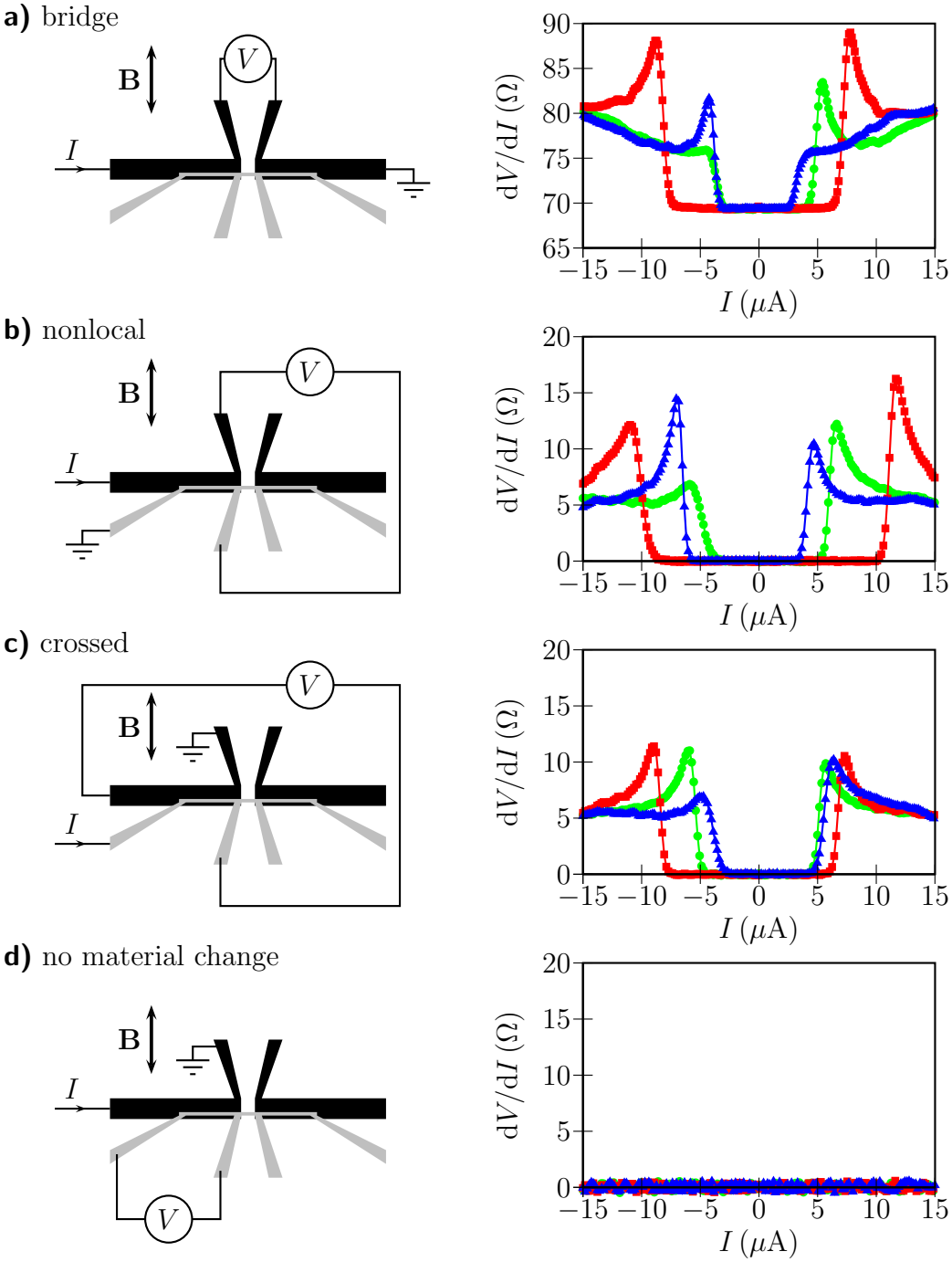

Figure 5.18: *Differential resistance of sample 902A for various contact configurations. The temperature during the measurement was* 4.2 *K. The magnetic fields for the curves were* 100 *mT (green circles),* 200 *mT (red squares), and* 600 *mT (blue triangles). The magnetic field was applied in-plane.*

902A offers the possibility of forcing different current paths and of probing the voltage at different points, which are connected to niobium or PdFe. A selection of representative configurations is shown in fig. 5.18 with the corresponding measured differential resistance.

In the bridge configuration, the current is sent from the thick niobium lead over the bridge to ground at the other main niobium lead. Voltage is sensed at the two niobium contacts close to the bridge. This is the configuration in which up until now all measurements were done on sample 902A. The differential resistance shows the typical behavior seen so far and the residual resistance in the valley centered around $I = 0\,\mu\mathrm{A}$ is attributed to the $Pd_{95}Fe_5$ bridge, as it increases with rising temperature, like it is typical of a normal metal, which is indicated in fig. 5.9 and fig. 5.10.

This temperature dependence of the valley is not present in the second configuration was shown already in fig. 5.1 for the $R(T)$ curve displaying charge imbalance peaks. Here the current is sent from the main niobium lead directly to the left palladium-iron contact. Voltage is measured at the niobium and palladium-iron probes close to the bridge. In the classical sense, the current and voltage paths do not cross, so that the voltage probes should lie at the same potential. Nevertheless, nonzero differential resistance is observed on both sides of a valley, where no voltage drop is seen.

Together with the asymmetries of the peaks enclosing this zero resistance region and the shift of the gap with respect to zero current, a similar picture like in the previous contact configuration is produced. In the valley, the resistance vanishes to absolutely zero, which also was checked by increasing the sensitivity of the lock-in amplifier. No voltage drop was found.

Quite contrary, the next contact configuration, which was called “crossed”, forces the current and voltage paths to intersect. It is important to notice that the current is now injected from a palladium-iron lead and not from niobium. Here, the curves show a behavior akin to the previous contact configuration: Nonzero differential resistance in the outer parts, a valley with constant $0\,\Omega$, confined by two asymmetric peaks. Although the same magnetic fields were applied in this and the previous contact configuration, the comparison of the differential resistances reveals some deviations: the peaks do not assume the same heights and the widths of the valleys do not match. Also the resistive outer parts behave differently.

In the last configuration, the current enters the structure at niobium and likewise runs to ground at a niobium contact. The voltage is probed at palladium iron leads. This situation in characterized by the current not having to cross the interface between both kinds of materials. The supercurrent flowing inside the niobium will not pass over to the resistive $Pd_{95}Fe_5$. No current means no voltage drop and, accordingly, no differential resistance was observed in this configuration.

In summary, one gains some new insights about the system. Three of the contact configurations presented here, i. e. the bridge, nonlocal and crossed configuration, produce a similar differential resistance, which, though, behaves different for every contact configuration, although the temperature and the magnetic fields are the same. The vanishing differential resistance of the last configuration hints at the interface between niobium and palladium iron as the cause for the oscillations.

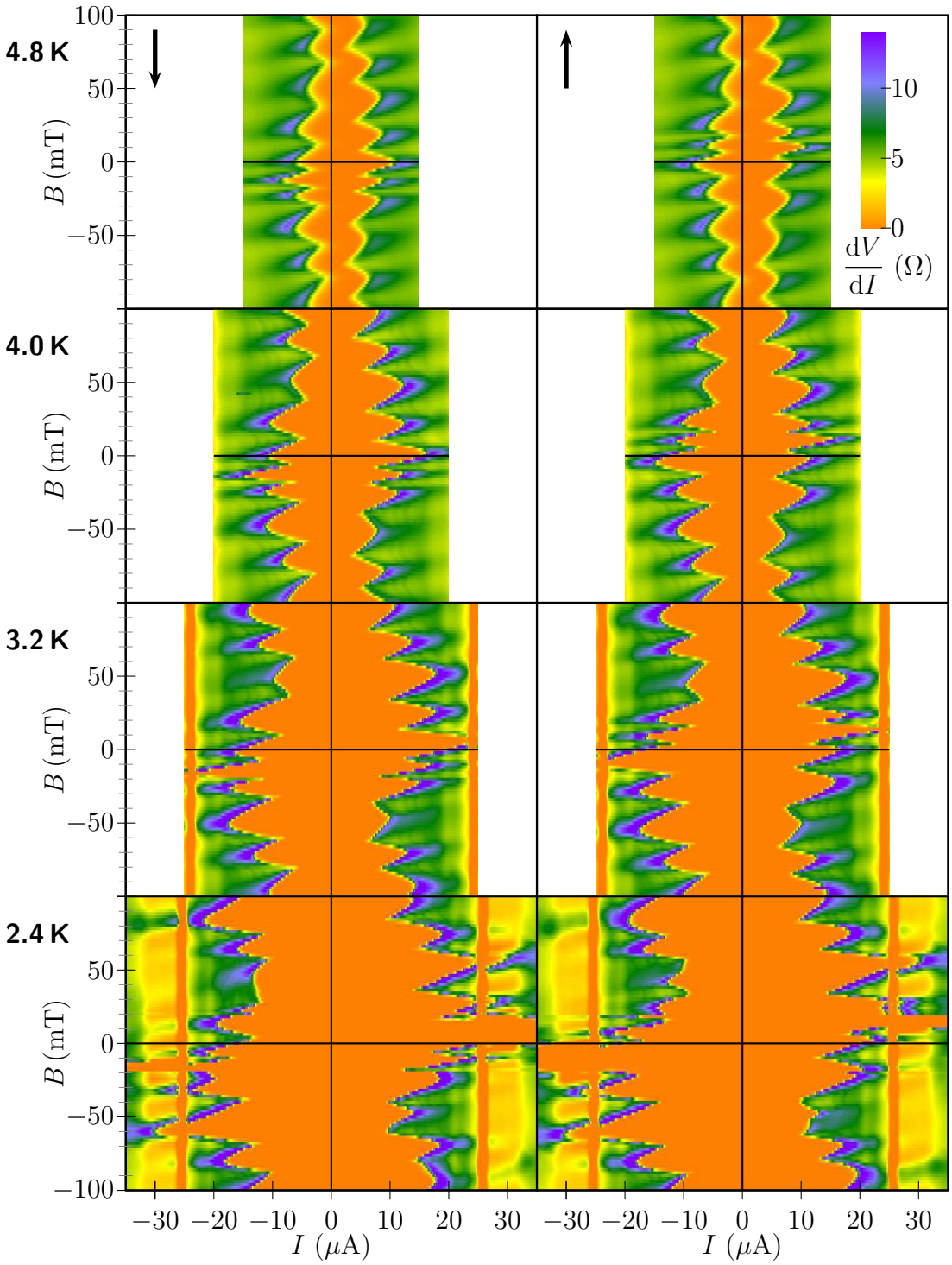

Figure 5.19: *Temperature evolution of the differential resistance pattern for sample 902A in nonlocal configuration (see fig. 5.18b). The sequence of the temperatures was from 4.8 K down to 1.6 K. The image for 1.6 K is shown in fig. 5.20. For reasons of contrast, the color scale is truncated to 0 Ω and 14 Ω. The current was swept from negative to positive values. The sweep direction of the the in-plane magnetic field is indicated by the arrows.*

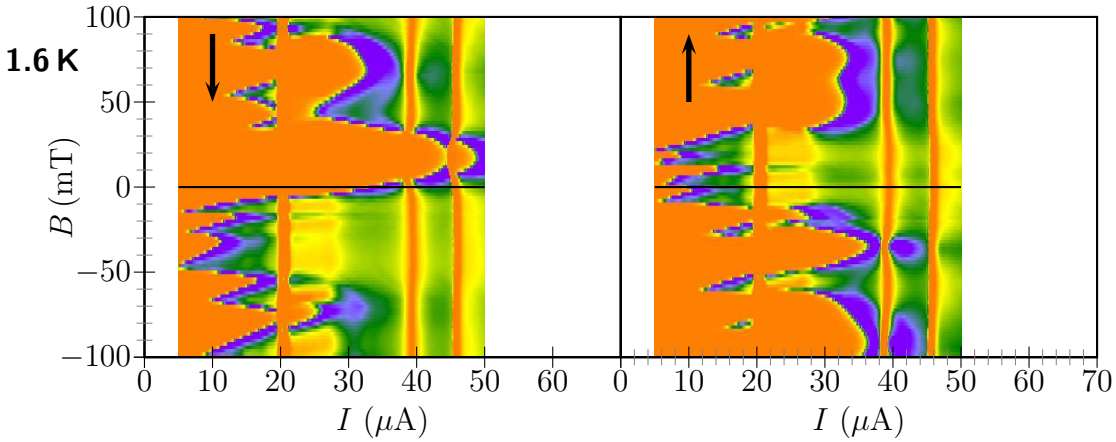

Figure 5.20: *Sequel of fig. 5.19. Data was collected only in the positive current range from $+5\,\mu A$ to $+50\,\mu A$.*

5.4.3 Nonlocal Configuration

As the measurements in the last section showed that the bridge does not play a decisive role in the development of the interference pattern, the nonlocal configuration was investigated more deeply. Therefore, temperature dependent behavior of the hysteretic region, like it was done already in sec. 5.4.1 for the bridge configuration, was repeated. The current and voltage contacts were chosen as in fig. 5.18b. Fig. 5.19 displays the results. At 4.8 K the line of critical current, hemming in the zero resistance valley, seems to be broader than at the other temperatures. This was caused by a longer integration time, which was inadvertently used in this measurement. This was corrected for the other temperatures.

Besides the expected broadening of the superconducting zone with decreasing temperature, the hysteretic behavior is again clearly visible. At least for 4.8 K, it compares well with the measurements fig. 5.16, where the $Pd_{95}Fe_f$ bridge was included in the current path. Comparing both magnetic sweep directions, one finds, that the hysteretic shifts are equal with respect to the $B = 0\,\mathrm{T}$ line.

But at lower temperatures, a new effect, the distortion of the differential resistance pattern, emerges. The whole hysteretic pattern gets less and less recognizable decreasing temperatures. Far away from this central region the regular oscillations recover at their usual positions.

Orange lines appear at the minimal and maximal current in the plot for temperature 3.2 K. These line are also there at 2.4 K and 1.6 K, see fig. 5.20. In addition to the line at $26\,\mu$A, two lines at $41\,\mu$A and at $47\,\mu$A appear in the image. Due to the truncation of the color scale it is not clear in those images, that these lines actually represent a sharp drop of differential resistance to negative values and a following sudden rise to the old level again.

This is more clearly shown by the single curves in fig. 5.21a). Even though the usual shifts of the peaks and the valleys are present for the two different magnetic fields, the downward spikes at $\pm 26\,\mu$A always remain at the same position. At -26μ A, the

differential resistance decreases at the spike to the same value for both magnetic fields. This is also reflected in the I-V characteristic represented in fig. 5.21b). At this current side, one curve lies quite well on atop the other. The downward spike of negative resistance appears here as a kink.

The picture is different on the positive current side. The differential resistance in the 56 mT curve shows a much less pronounced spike than in the 66 mT curve. The difference is, that the weak spike lies in a very low resistive region, while the strong spike lies in a high resistive region. The behavior of the kinks of the I-V characteristic corresponds to the spikes. At the higher magnetic field, the kink is stronger than at the lower magnetic field.

5.5 Periodicity And Flux

In this experiment the dependency of the oscillations on the orientation of the sample in the magnetic field was examined. The tilting has an effect on the magnetic flux through the sample. As it is defined as $\Phi = \mathbf{B} \cdot \mathbf{A} = B \cdot A \cdot \cos(\alpha - \pi/2)$, where α is the angle enclosed by the surface of the sample and the magnetic field, it is increased, as α grows. Thanks to the tilting mechanism built into the cryostat the whole range of angles between 0° and 90° could be covered.

In order to increase the speed of measurement, the data was recorded using a different method. The setup for differential resistance in fig. 4.3a provided the basis. Instead of sweeping the dc current source (Yokogawa 7561), it was held fixed at 12 μA while the magnetic field was swept continuously. From any image plot (e. g. fig. 5.8), one can see, that along a constant current line in the resistive region, the differential resistance changes with the same periodicity as the interference pattern. Both the short and the

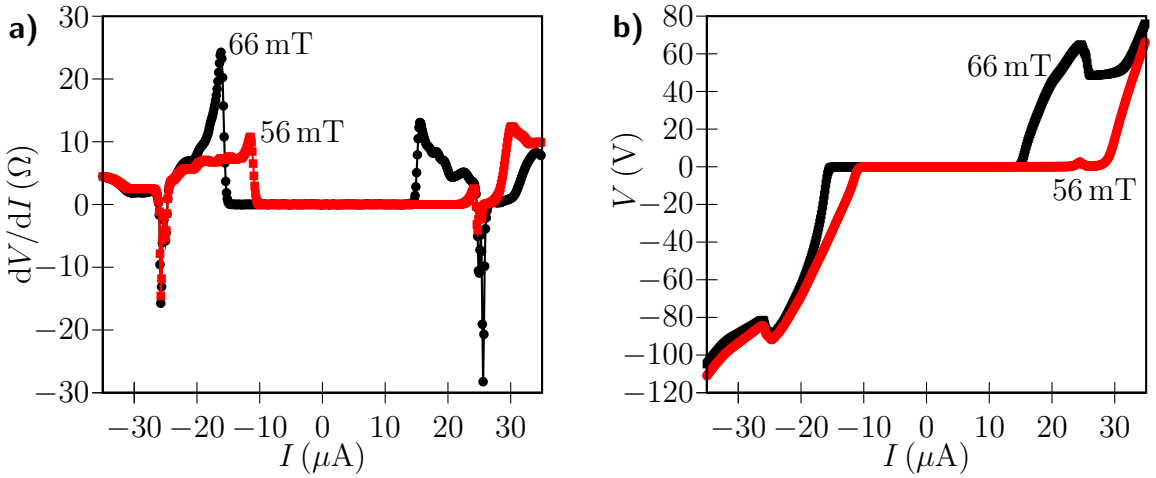

Figure 5.21: *Single line scans for the plot at temperature 2.4 K in fig. 5.19. The up sweep (− → +) side was taken at magnetic fields 56 mT and 66 mT for these graphs. a) The differential resistance. b) The integration of graph a) giving the current-voltage characteristic of the sample.*

long oscillations are reproduced by this measurement method. Fig. 5.22 shows the results obtained for gradually tilting the sample from the in-plane position of the magnetic field to the perpendicular direction. The in-plane starting point is shown in the sketch of the contact configuration in fig. 5.8.

At the beginning of the tilting, i. e. at small angles, the change of the period is very strong. In contrast, there only is a very small diminution of the period at high angles. The curve at 0° was scanned for the whole range of the magnetic field from $-0.6\,\mathrm{T}$ to $+0.6\,\mathrm{T}$. Here, also the hysteretic contraction of the pattern around $B = 0\,\mathrm{T}$ is very distinct. In the graph for 5°, this region is absent. But one can observe that before that, there was a stretch of relative irregular oscillations. Farther towards the lowest magnetic fields the pattern was regular. This behavior of irregular sections in the curves can be seen for most of the angles. This might be due to flux trapped in the structure or due to moving vortices. The assumption is affirmed by the observation that at the start of the measurement, when the sample was able to relax for some minutes, no such irregularities occur. Nevertheless, the regular regions provide a means of determining the period of the oscillations, which will be further discussed in sec. 6.3.

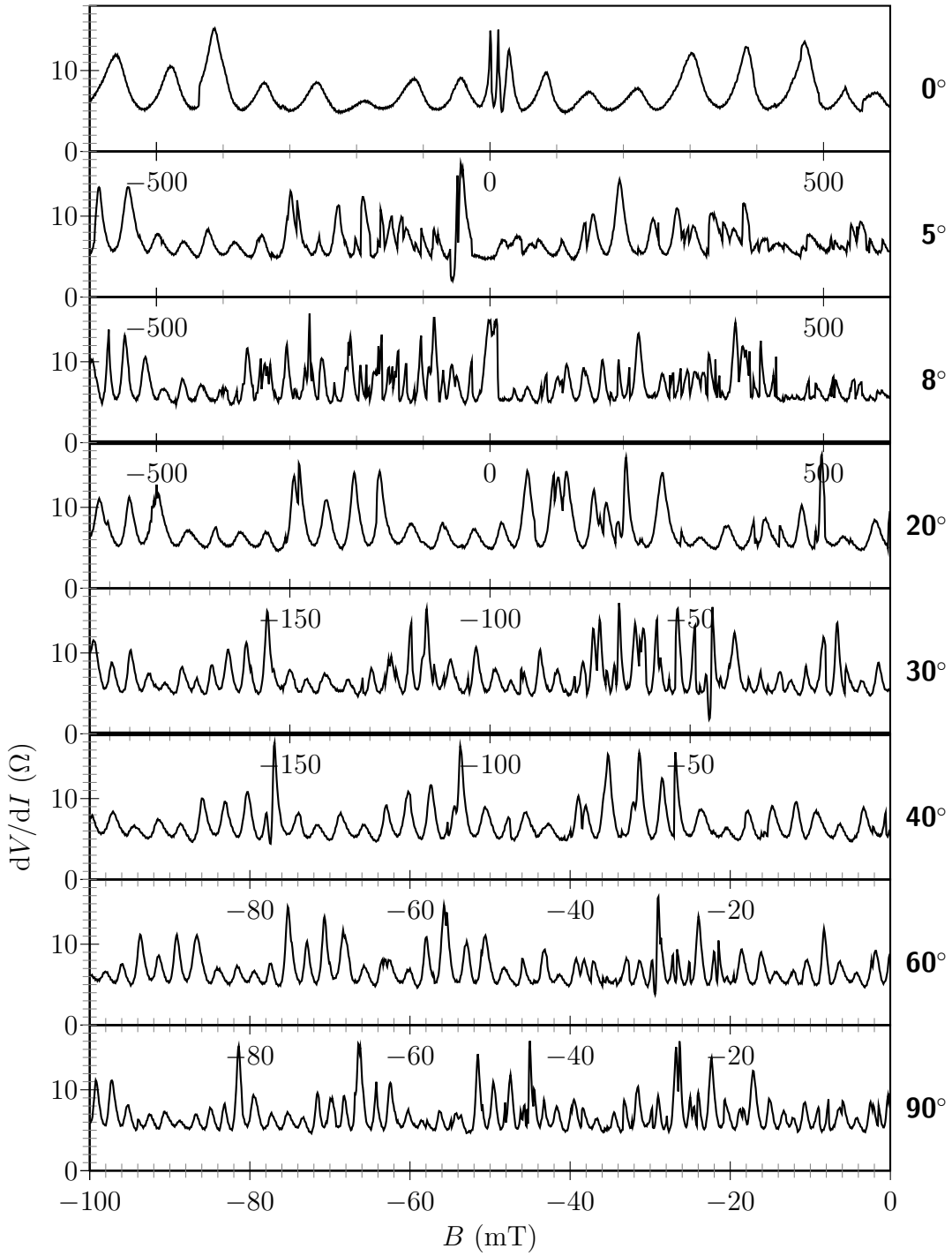

Figure 5.22: *Line scans at constant current $I = 12\,\mu A$ and $T = 4.2\,K$ showing the differential resistance oscillations in a completely resistive region. The sample plane was tilted relative to the magnetic field from the in-plane direction* (0°) *to a perpendicular orientation* (90°)*. The degrees on the right side indicate the deviation of the magnetic field from the in-plane direction. The thicker lines in between the single curves indicate a change of the scaling of the magnetic field axis.*

6 Discussion

The measurements on $Nb/Pd_{95}Fe_5$ hybrid structures impose some questions. These may be classified into several groups whose connection to the parameters changed during the measurement is quite apparent, on the one hand. On the other hand, there are experimental results whose origin cannot easily be determined initially.

One group of questions is related to experimental facts which appear due to the magnetic field, or due to its change, respectively. Among those are the appearance of oscillations, the dependence on the sweep direction of the magnetic field, change of period close zero magnetic field, and jumps and irregularities in the simple graphs and color coded plots of differential resistance.

Another flock of questions emerges by effects observable only if the electrical current is varied. Here we have in particular all the effects connected to the differential resistance measurements. This quantity shows a behavior whose details, like the existence of a valley with lower or zero resistance, its adjacent peaks, the asymmetry of the peaks and the structure of the regions with higher resistance, deserve closer inspection.

Another parameter which changes the picture is temperature. The width of the valley shrinks with rising temperature, likewise is the amplitude of the oscillations of magnetoresistance and the depth of the peaks in the color coded plots of differential resistance diminished.

In this chapter, these questions will be addressed. Although not a simple conclusive picture can be given in the end, some argumentation can be presented which could lead to a somewhat deeper understanding of the observed effects.

6.1 Relation Between Magnetoresistance And Differential Resistance

In sec. 5.3, magnetoresistance oscillations were described, which emerged during sweeping the magnetic field and applying an alternating current of $10\mu A$. There clearly is a connection to the differential resistance measurements. The similarity of many features of the curves in fig. 5.11 and fig. 5.14 with the magnetoresistance oscillations in e. g. fig. 5.2 is apparent. They both show oscillations with the same periods, a peak in the middle and hysteretic behavior. The physics behind both kinds of graphs must be the same, but the measurement methods for both data is fundamentally different.

A successful attempt of linking both kinds of data has been made by taking measurement method of the magnetoresistance into account. The signal which is output by the

lock-in amplifier is equal to the result of the following formula [Kun86]:

$$U_{\mathrm{out}}(t) = \frac{1}{\tau}\int_{t-\tau}^{t} \mathrm{d}s \sin\left(2\pi f_{\mathrm{ref}} s + \varphi\right) U_{\mathrm{in}}(s) \tag{6.1}$$

where τ is the integration time and φ the phase between the reference signal f_{ref} and the signal from the sample U_{in}. U_{in} is just the integral of the differential resistance, where the integration constant can be fixed by taking into account that $V(I = 0\mathrm{A}) = 0\,\mathrm{V}$. During the magnetoresistance measurements, the phase φ was virtually 0.

Some thought has to be spent for the integration range τ. This parameter, the time constant of the lock in, determines the improvement on the signal to noise ratio and gives the integration range in eq. (6.1). As the differential resistance data is quite noise free and for the sake of simplicity, the integration range is chosen to go from $-I_0$ to $+I_0$, which corresponds exactly to half a period T of the reference signal. To fulfill the constraint of an in phase measurement ($\varphi = 0$), the variable term in the argument of the sine, $2\pi f_{\mathrm{ref}} s$, must start at $-\pi$ and end at $+\pi$ during the integration. The current of the reference signal depends on time as $I(s) = I_0 \sin(2\pi s/T)$. Considering this dependence, the phase constraint, and the integration range, one obtains the formula

$$U_{\mathrm{out}} = \frac{1}{\pi}\int_{-1}^{+1} \mathrm{d}x \frac{x}{\sqrt{1-x^2}} U_{\mathrm{in}}(x)\,, \tag{6.2}$$

where $x = I/I_0$.

This expression now makes it easy to transform the differential resistance data to magnetoresistance curves. Consider for instance the data in fig. 5.9. The differential resistance first has to be integrated with respect to current at constant magnetic field in order to obtain the current-voltage characteristics $U_{\mathrm{in}}(I)$. To be able to compare the results for all temperatures, I_0 is set to $7.5\,\mu\mathrm{A}$, as this is the maximum range which can be applied to *every* graph. Then, after eq. (6.2) has been evaluated, the result can be plotted as a voltage depending on magnetic field and examined in fig. 6.1.

The similarity of this picture with fig. 5.4 approves the interpretation of the magnetoresistance oscillations as a different manifestation of the differential resistance pattern. The well known vanishing of the oscillations with rising temperature are common to both figures, the distorted region around $B = 0\,T$, the different periods of oscillation, the bending of the curves upwards with rising absolute value of the magnetic field, and also the cut-off of the oscillations at the lowest temperature.

This last feature is now easily understandable. For the following explanation, it is advisable to compare fig. 5.8 and the curve for 4.2 K in fig. 6.1. If the integration range, or the reference current, respectively, only stays within the valley of constant differential resistance for consecutive magnetic fields, no change of voltage can occur, as the integral comprises the same values for both magnetic fields. This is most articulate in the two figures between 0.19 T and 0.20 T. Only when the rim of the valley is crossed, then a change can be observed. This picture can now be transferred to the magnetoresistance measurements, where the same effect is responsible for the cut-off at low temperatures. Clearly, this cut-off can be avoided by increasing the amplitude of the reference current, in the same way as the integration range can be enhanced.

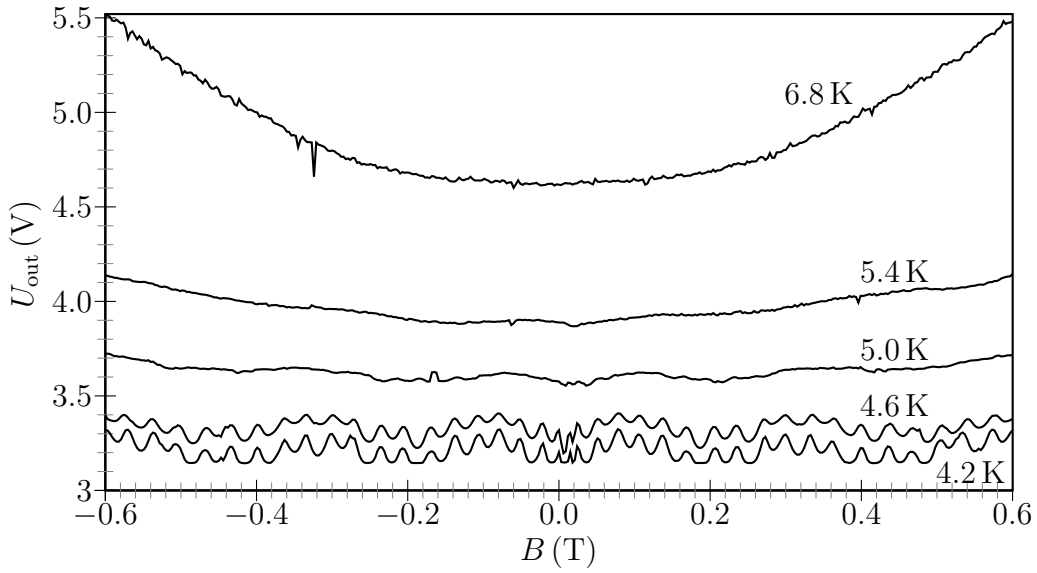

Figure 6.1: *Simulation of the magnetoresistance oscillations for different temperatures as derived with the help of the lock-in formula eq. (6.2) from the data presented in fig. 5.9. This simulation of the lock-in measurement technique was done with the assumption of an oscillating current of* $7.5\,\mu A$*. The voltage given on the right should not be compared with magnetoresistance measurements, as some factors during the calculation of this data were not taken into account.*

The distinct hysteretic peaks close to $B = 0\,T$ in fig. 5.2 and the other figures with magnetoresistance originate from the integration range being chosen in such a way that barely any resistive region is touched, because at this position the dents of the differential resistance pattern are situated, which extend furthest outwards.

The magnetoresistance oscillations were, apart from the hysteretic region, symmetric about $B = 0\,\mathrm{T}$. This now can be ascribed to the point symmetry about $B = 0\,\mathrm{T}$ and $I = 0\,\mu\mathrm{A}$ of the color plots of differential resistance. Under the integral in eq. (6.2), the same values appear regardless if the integral is taken at the positive or the negative magnetic field. The exactness of the calculated symmetric curve in fig. 6.1 from the differential resistance data, on the other hand, is an indication of the point symmetry of the differential resistance pattern. This was already presumed in fig. 5.14, where the critical currents of the negative and the positive current side were compared.

6.2 Hysteretic Behavior

Another effect related to the magnetic field is the hysteretic behavior of the central region of the magnetoresistance oscillations and the differential resistance plots around $B = 0\,\mathrm{T}$. An example for this can be found in fig. 6.2. One observes that in this region the width of the bulges of the constant differential resistance valley is compressed and it is shifted depending on the sweep direction of the magnetic field.

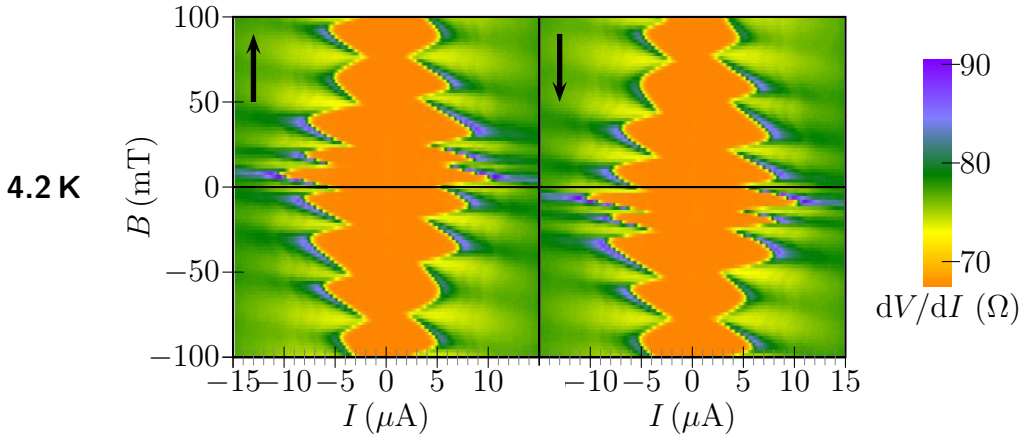

Figure 6.2: *Hysteretic behavior of magnetoresistance in magnetic field. This plot for 4.2 K is taken from fig. 5.16. It shows the difference of the central region at $B = 0$ T for the two magnetic sweep directions which are indicated by the arrows..*

An interpretation of these facts can be given in terms of the ferromagnetic switching of the $Pd_{95}Fe_5$ layer in the sample. There are actually two magnetic fields existent in the sample. One, $\mathbf{B}$, comes from the external source, the magnetic coils of the cryostat. The other one, $\mathbf{B}_M$ is generated by the magnetic moment of the ferromagnetic layer. Both are superposed linearly to create the total magnetic field $\mathbf{B}_{tot} = \mathbf{B} + \mathbf{B}_M$. The external field alone changes linearly and and its direction is fixed by the axis of the coils producing this field, which only allows a sign reversal. Thus it cannot be the root of the distortion of the central region. The magnetic moment of the $Pd_{95}Fe_5$ layer on the other hand, hence also $\mathbf{B}_M$, depends nonlinearly on $\mathbf{B}$, as is known from the anomalous hall measurements and the SQUID measurements depicted in fig. 2.2b and fig. 2.6b. It can be assumed that there are magnetic domains in the layer, which may switch more or less independently their direction of magnetization. This leads to a reduction of the magnetic moment of the layer at low magnetic fields, as not all domains are oriented in the same direction. Also the direction of the magnetic moment may deviate from the external field $\mathbf{B}$, as it depends of the orientation of the single moments of the domains. At high magnetic fields, all the domains are directed in the same direction. The magnetic moment therefore is saturated and only the variation of the external field plays a role here, see fig. 2.6b displaying the magnetic moment of $Pd_{95}Fe_5$. Hence there is a linear increase or decrease of the Hall resistance, which depends on the combined field B_{tot}.

Just this switching of the magnetic moment of the $Pd_{95}Fe_5$ layer is depicted in fig. 2.2b and fig. 2.6b. B_{tot} therefore also performs this rapid change. This happens in a range of around 50 mT which compares quite favorably with the width of the compressed area as shown in fig. 6.2. Fig. 2.6b demonstrates that this effect is hysteretic, as is expected from ferromagnetic material. This also accounts for the hysteretic shift of the distorted central region in the image plots of differential resistance.

The fact that the pattern of the differential resistance and the magnetoresistance oscillations follow this switching quite closely leads to the conclusion, that the magnetic

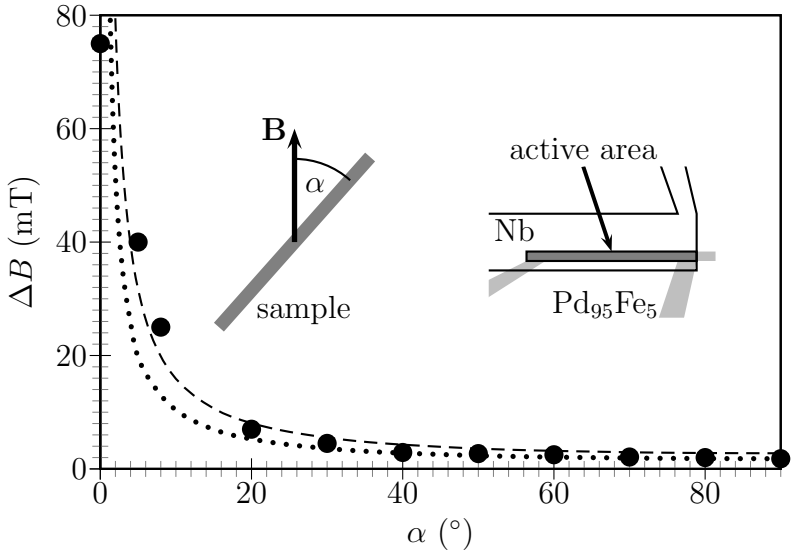

Figure 6.3: *Period of the small oscillations depending on the tilting angle of the sample plane normal with respect to the magnetic field. The black dots designate the experimental data. The dashed and dotted lines are fits to the data, using eq. (6.3) and parameters calculated from the geometrical data of the sample (dashed) and from the period at* 90° *(dotted). The left sketch demonstrates the geometry of the experiment. The right insert contains a cutout of the sample geometry with the active area assumed for the fits indicated in dark gray.*

field plays an integral role in its formation.

6.3 Period Of Oscillations And Of Patterns

As has been shown in the last section, the magnetoresistance oscillations and the differential resistance depend on the magnetic field, to say it more exactly, on the magnetic flux. This can be inferred from the measurements in sec. 5.5. The period can be determined from the data in fig. 5.22. The result is shown in fig. 6.3 as black dots. The lines drawn in the graph represent fits to this data based on quantum interference.

It is assumed that exactly one period of the oscillation should be completed if the flux through an active area A has changed by one flux quantum, c. f. sec. 3.5 and sec. 3.6. This corresponds to a change of magnetic field of $\Delta B = \Phi_0/A$. If the sample area gets tilted from a position, where the magnetic field vector lies in the sample plane ($\alpha = 0°$), to a configuration in which it is directed perpendicular ($\alpha = 90°$), then the area is given by $A = A_0 \sin\alpha$. This yields an expression for the dependence of the distance of the oscillation maxima (or minima) on the tilting angle:

$$\Delta B = \frac{\Phi_0}{A_0 \sin\alpha}\,. \tag{6.3}$$

The fit designated by the dashed line was calculated using the geometrical data of the $Nb/Pd_{95}Fe_5$ bilayer taken from fig. 4.1b. The full area then is $A_0 = 4\,\mu m \times 180\,nm =$

$0.72\,\mu\mathrm{m}^2$. With this parameter, the calculated curve fits the measured points generally best, but fails at the extremal angles 90° and 0°, where too high periods of 158 mT and 2.76 mT result. But in between, at the knee, the agreement is quite accurate.

Two experimental reasons argue for using the bilayer area in this fit. First, the period roughly corresponds to this area. From fig. 4.1b it is apparent that there is no other area on the same order of magnitude. The small niobium single layer between the palladium iron contact is smaller than the area of the bilayer, even EBL inaccuracies are taken into account, and would produce a fit worse than the one obtained from the bilayer area. The remaining single layer niobium covers a region which is much too large.

A second rationale for the bilayer as the active region is found in the experiment described in sec. 5.3.1. Here the magnetoresistance oscillations of two structures with different lengths of 200 nm and of 600 nm of the $Pd_{95}Fe_5$ bridges were measured. The elongation of the bridge corresponds to a shrinking of the $Pd_{95}Fe_5$/Nb bilayer. On one side of the bridge the bilayers covered an area of $1.9\,\mu\mathrm{m} \times 0.2\,\mu\mathrm{m} = 0.38\,\mu\mathrm{m}^2$ and of $1.7\,\mu\mathrm{m} \times 0.2\,\mu\mathrm{m} = 0.34\,\mu\mathrm{m}^2$, calculated of their respective lengths and widths. Between the measurements presented in fig. 5.2, the sample was not tilted. Also, both structures were situated on the same sample and therefore were fabricated under exactly the same conditions. Therefore the periods of the oscillations can be compared reliably. The sample with the larger area produced a period of 51 mT, the other one showed a period of 65 mT in agreement with eq. (6.3).

Another sensible approach to fit the data in fig. 6.3 seemed to take the area calculated from the experimental data for the period $\Delta B = 1.8\,\mathrm{mT}$ at 90°, where the variation of ΔB on the angle is weak and therefore the uncertainty of A_0 is smallest. This yields a value of $A_0 = 1.15\,\mu\mathrm{m}^2$, which is 1.6 fold the area calculated from the geometrical data. The dotted line represents this fit. The calculation fits the points at 0° and 90° better, yet produces bad results for the knee region.

By using other values of A_0, the measured data can also not be fitted completely. Nevertheless, the general picture is quite well reproduced by this model. A reason for the imperfection of the fit may be found in the inverse proximity effect. With tilting the sample out of the in-plane position of the magnetic field, more and more flux per area penetrates the sample. This increasing magnetic flux has the tendency to break superconductivity. By this, those areas may be enlarged in which it is weakened already by the inverse proximity effect originating from the adjacent diluted ferromagnetic layer. In this way, the area A increases as the sample is more and more tilted. Therefore, the period decreases more rapidly as would be expected from the simple formula in eq. (6.3).

As a second reason, the demagnetizing factor of superconductors may be given. As a superconductor is perfectly diamagnetic, it tends to displace the magnetic field lines, so that they cannot penetrate the superconducting areas. In that way, the density of the field lines close to the superconducting Nb single layer is increased. As in the Nb/$Pd_{95}Fe_5$ bilayer the superconductivity is weakened by the additional magnetic field from the ferromagnet, even more field lines will penetrate this area, thus increasing the effective flux.

This experiment speaks for quantum interference effects as the root cause of the magnetoresistance oscillations and the differential resistance patterns. However, it is hard

to justify a closed path around the Nb/$Pd_{95}Fe_5$ bilayer, in which the necessary supercurrent can circulate. The $Pd_{95}Fe_5$ contact leads, contacting the assumed active area as indicated in fig. 6.3, constitute an obstacle for the circulating current. As their width is of the same order as the width of the active area, it is not reasonable to adopt the view of the supercurrent penetrating this obstacle, but not the active area. The same is true for the active area itself, as on the right hand side, where the bilayer passes over to the $Pd_{95}Fe_5$ single layer, which forms the bridge, no channel for the supercurrent is available. Of course, this does not take into account fringe effects, and maybe trapped magnetic domain walls, where due to the magnetic moments pointing in different directions, the resulting magnetic field is locally weakened so that supercurrent may flow.

A hint on the importance of the magnetic domains is probably given by the irregularities in the magnetoresistance oscillations and the differential resistance patterns. The contours of critical current in fig. 5.11 illustrate this. At low temperatures (4.2 K and 5.0 K), there sometimes appear irregularities, especially at the local extremal regions. The incisions in the curves may be due to domain walls wandering in the ferromagnetic layer or single smaller ferromagnetic domains suddenly turning their magnetic orientation and thus changing the flux abruptly. Yet, the irregularities are a lot more numerous at lower temperatures. Such a strong dependency on temperature is not expected for the magnetic behavior of the $Pd_{95}Fe_5$ whose Curie temperature is around 180 K.

There is another entity in the system which is able to influence the critical current. Niobium is a type II superconductor. This means that above a critical field H_{c1}, the magnetic field can enter the superconductor in the for of vortices. Vortices are able to carry flux. They consist of supercurrent circulating around a normally conducting core in which the field lines of the magnetic field are captured. It has a radius of approximately the superconducting coherence length ξ, which has been treated in more detail in sec. 3.3. If an electrical current is applied on a superconductor with vortices, they start to move, displacing their normal cores and thereby dissipating energy. This results in a measurable resistance. If the vortices are captured by *pinning centers*, regions of weakened or inhomogeneous superconductivity, and thus made immovable, the emergence of this resistance is prevented. Nevertheless, those pinned vortices may detach from a pinning center, start to move and eventually be captured again by another pinning center. The resistance and also the distribution of the magnetic flux are changed by this process, which finally may lead to disturbances in during the measurement. In contrast to the magnetic properties, superconductivity changes appreciably in the temperature range from 4.2 K to 6.6 K as covered by the measurements displayed in fig. 5.9 and fig. 5.11. Therefore the occurrence of the irregularities may be augmented.

6.4 Differential Resistance And I-V characteristics

Ultimately, both the the patterns displayed in the color scale plots are based on differential resistance measurements at changing magnetic fields. Examples of such single measurements are given in fig. 5.7 for the contact configuration including the bridge in the current path. To have these illustrations at hand, parts of this figure are cited here

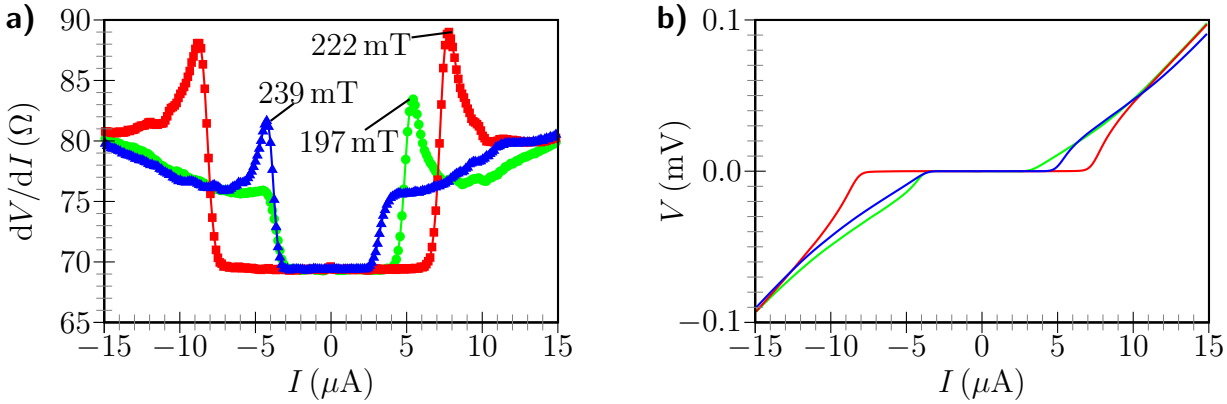

Figure 6.4: *a) Differential resistance and b) I-V characteristics of sample 902A at three magnetic fields, taken from fig. 5.7. The colors in graph a) and b) correspond to each other. b) was obtained by subtracting the constant background of the differential resistance of 70 Ω from a) before the integration.*

in fig. 6.4.

As has already been pointed out, the asymmetry of the differential resistance, expressing itself in the disparate peak heights, the shift and the shrinking and enlargement of the valley, is remarkable. This asymmetry does not depend on the current sweep direction, which was tested at various magnetic fields. The fact that the differential resistance depends on the current flow direction means that in this experiment time reversal symmetry is broken. If also the magnetic field is reversed, then the same value of differential resistance is observed. As a whole picture, the point symmetrical plots like e. g. in fig. 5.8 are obtained.

The asymmetry is reflected also in the I-V characteristics in fig. 6.4b, as these curves emerge by integrating the differential resistance, using the fact that at $I = 0\,\mathrm{A}$ also $V = 0\,\mathrm{V}$. Previously a constant differential resistance of $70\,\Omega$ was subtracted, which shifts the valley in fig. 6.4a to $0\,\Omega$. This was done in the assumption that this remaining resistance stems from the $Pd_{95}Fe_5$ bridge. The features coming from the other structures can then be more easily seen in the I-V characteristics. This operation is further justified by the measurements in the nonlocal contact configuration presented in fig. 5.18. The curves in fig. 6.4b correspond to the I-V characteristics of the latter measurement. Therefore it can be concluded that the differential resistance is not due to the ferromagnetic bridge.

The form of the curves in fig. 6.4b reminds of the typical characteristics of an overdamped Josephson junction. The Ambegaokar-Halperin theory for overdamped Josephson junctions [AH69] states that even below the theoretical critical current I_c introduced in eq. (3.18), there is a finite resistance which dies out exponentially as the current I goes to zero. The onset of this resistance is the steeper the closer it happens at I_c. Then above I_c, the progression of the I-V characteristic becomes more and more linear. This is also the behavior observed in fig. 6.4b. Conferred to the differential resistance this means that at a steeper onset the peaks are higher, while a smooth onset results in a low or vanishing peak. This might be affirmed by the color scale plots, e. g. fig. 6.2, in which

the higher peaks (blue-violet areas) occur at higher current. At low currents, the peaks are also lower. This statement represents just the tendency, as there still the oscillations, asymmetries and shifts of the constant resistance valley have to be considered, which cannot be explained by this model. The onset of the resistance in the I-V characteristic is determined by the *normalized activation energy* $u = \hbar I_c / e k_B T$, where in these experiments, $I_c \approx 10\,\mu$A and $T \approx 5\,K$, which amounts to $u \approx 95$. This value would reproduce a similar onset of resistance as observed in fig. 6.4b. For $u = \infty$, the differential resistance diverges and for $u = 0$, it is the normal state resistance. This formula on the other hand depends on the critical current I_c and the temperature T, which must be determined by other effects still requiring clarification. It must be stressed again, that this theory just constitutes an attempt at explaining the I-V characteristics and should not be considered the final word on this topic. Namely it is again difficult to locate locate the weak link required for the formation of the Josephson junction in the sample. Such a region could be suspected in the Nb/$Pd_{95}Fe_5$ bilayer where the superconductivity is weakened by the dilute ferromagnet beneath, as the inverse proximity effect and the additional magnetic field break Cooper pairs. The surrounding niobium areas are the superconducting banks.

As has been mentioned already in sec. 5.4.1, there are strong indications that the valley of constant differential resistance is cause by a critical current. Firstly, the shrinking of the valley width with rising temperature and its vanishing close to the critical temperature of the superconductor as shown in fig. 5.9 and fig. 5.16 can be given. Secondly, the measurements in the nonlocal and crossed contact configurations in fig. 5.18b and c prove that no differential resistance is present in this current domain, if the normal conducting bridge is elided from the current path. By exploiting the condition that at $I = 0\,\mu$A also $V = 0\,V$, the resistance in this region can be set to zero. So, within the valley, also for $I \neq 0$ A, there is no voltage drop, which is typical of a supercurrent.

The crossed configuration in fig. 5.21 may give rise to the supposition, that the onset of differential resistance is caused by the voltage dropping between the start and the end of the bilayer, i. e. the points where the $Pd_{95}Fe_5$ contact leads enter the bilayer stripe. The current flow in this contact configuration can be imagined as being from left to the right, covering the whole bilayer area. But since a similar pattern can be observed in the nonlocal contact configuration fig. 6.4b, where the current in this naive picture flows from the leftmost niobium lead to the leftmost $Pd_{95}Fe_5$ lead and should not be forced to penetrate into the area between the vertically arranged voltage probes, the aforementioned reasoning is no longer cogent. Although it is to be expected that the current spreads over the whole superconducting niobium area, the higher current density at the interface between the niobium and the $Pd_{95}Fe_5$ layer is expected at the left end of the bilayer. Current entering at the right end of the bilayer would feel higher resistance, since the ferromagnetic layer, through which it has to pass, is expected to stay normal conducting. Due to this reduced current, a lower voltage drop between the corresponding probes in the nonlocal contact configuration would be anticipated. But the I-V characteristics obtained by integration of the differential resistance shows voltages of similar magnitude for both the nonlocal, the crossed and the bridge contact configuration. (The offset from the bridge has to be subtracted from the latter.) So one

can conclude that, at least for the general picture, the contact configurations as considered up to this point only play a minor role. Nevertheless, the differential resistance curves resulting from each contact configuration in fig. 5.18 are different. This might indicate local variations of the effect.

The last configuration labeled *no material change* is different from the other three in that respect that the current does not have to cross the interface between Nb and $Pd_{95}Fe_5$. As a result, the effect vanishes and the differential resistance is constantly zero over the whole measurement range. Consequently, the interface is involved in the emergence of the resistance.

An interesting feature of the differential resistance are the strong peaks at high currents. The 5.0 K plot in fig. 5.10 is a prominent example. This spike occurring at 12.5 μA should also exist at the other temperatures. The smaller current range at higher temperatures does not cover its location, and at 4.2 K, it lies beyond the measurement range. Fig. 5.16, on the other hand, displays it indirectly for all measured temperature. It is situated at the transition lines from the yellow-green regions to the blue-violet areas. With higher and higher temperature these lines move more and more towards the $I = 0\,\mu$A line. This temperature behavior indicates a connection with superconductivity. It is supposed, that some superconducting region quite abruptly becomes normal conducting and this jump in resistance produces the spike observed in differential resistance. Since the critical current is diminished at higher temperatures, the position of the spike follows suite.

7 Control Experiments

7.1 Pure Palladium Layer

For comparison, a sample with pure palladium was made. This should prove that the nonsuperconducting layer has to be ferromagnetic for the interference effect to appear. For the sample layout see fig. 4.1a. As this was a design 1 sample, only the measurements with the contact configuration in fig. 7.1b were available.

The image plot of differential resistance is shown in fig. 7.1. Again there is a valley of zero differential resistance flanked by high resistance plateaus on both sides. The critical current can be marked by two straight lines at -5.9 μA and 9.7 μA. The interference effect cannot be observed here. The sweep direction of the current was from negative to positive values. This explains the shift of the zero resistance valley to positive current. Coming from $-15\,\mu$A, the sample is in the normal conducting state. Due to the resistance, electrical energy is dissipated, creating heat and hence a rise of temperature. At higher temperatures the absolute value of the critical current is lowered leading to a resistance jump at $-5.9\,\mu$A. While it is in the superconducting state, no energy is converted to heat and the sample can cool down again which increases the critical current to $+9.7\,\mu$A. This asymmetry must depend on the current sweep direction. Fig. 7.1c confirms this behavior. With the ferromagnetic samples no such dependency of the sweep direction has been observed.

Another very interesting fact is shown in fig. 7.1d. The resistance of the contact configurion with niobium only drops very sharply at 6.6 K. There are no steps whatsoever in this transition. The resistance including the palladium bridges displays the same sharp drop at 6.6 K followed by a smoother decrease between 6.6 K and 5.5 K. Then the resistance suddently falls to zero. The smoother decrease hints at the proximity effect in palladium. With falling temperature the proximity superconductivity extends farther and farther from the two niobium electrodes into palladium until in the end both regions start to overlap at 5.3 K and the whole bridge is superconducting. This is indicated by $0\,\Omega$ resistance for temperatures lower than 5.3 K. Due to the symmetry of the sample, the distance at which the effect reaches into palladium is at least 100 nm, as the length of the bridge was lithographically defined to be 200 nm.

We can learn from these measurements, that a magnetic layer is necessary for the interference effect to appear. The pair breaking effect of the ferromagnetic palladium-iron layer in the former samples supposedly provides the weak links at the bilayers of $Pd_{95}Fe_5$ and Nb. In a nonmagnetic sample the palladium gets very easily superconducting, so no weak links will be formed.

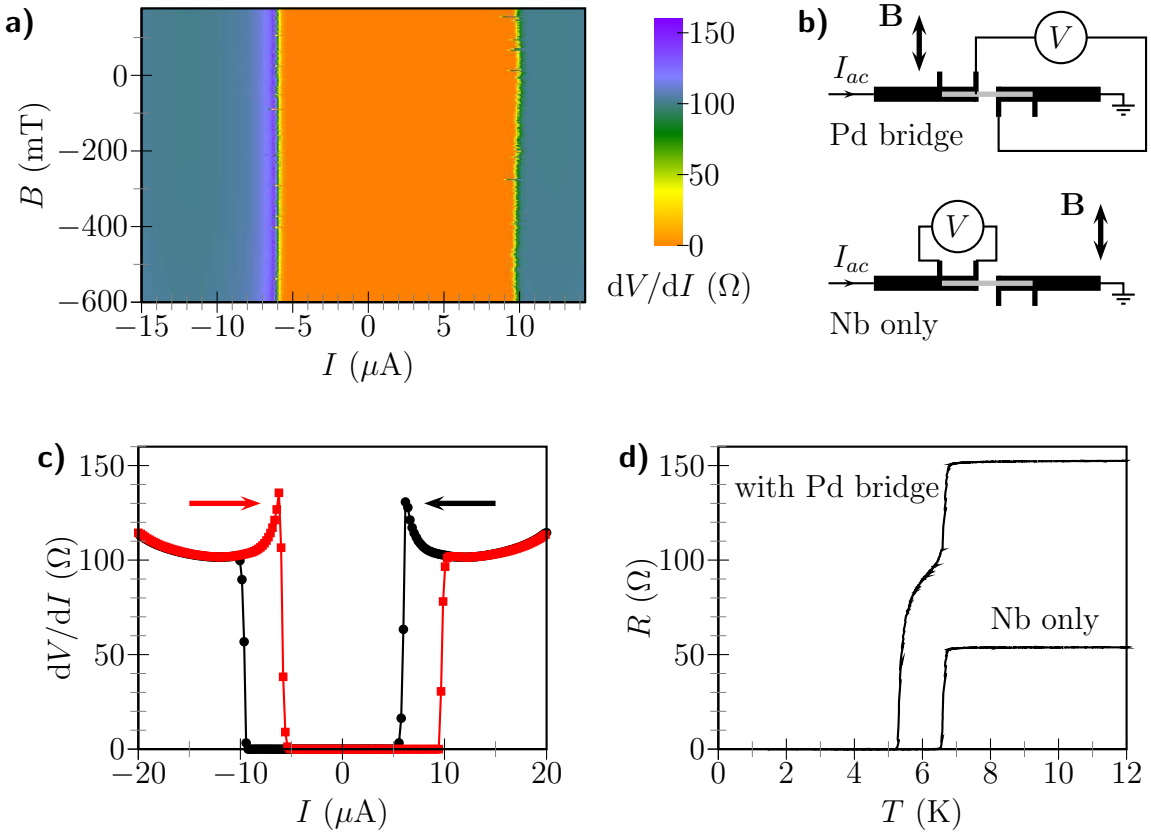

Figure 7.1: *Measurements for the sample with pure palladium bridge of length* 200 *nm. a) Image plot of the differential resistance at* $T = 5.0\,K$*, sweep direction of the current was from negative to positive. b) Contact configurations. The configuration labeled "Pd bridge" was used in a), c) and d). The lower setup labeled "Nb only" was used in d). c) Single graph of differential resistance for two current sweep directions at* 5.0 *K. The arrows indicate the sweep direction belonging to the respective peak. d) Resistance over temperature, measured once over the niobium and the palladium-iron bridge and once only over niobium.*

7.2 Alternative Measurement Method

Another sample was measured to confirm the previous measurements with a ferromagnetic layer. The temperature dependence of the resistance in nonlocal configuration is shown in fig. 7.2 for various current amplitudes. Again, there are various transition temperatures visible. The highest one is at 6.7 K. For 1 μA and 10 μA charge imbalance causes a peak at that point followed by a slow resistance drop. This peak is suppressed for the 30 μA curve, possibly due to heating effects, which shrink the superconducting gap. At 5.7 K the 1 μA curve drops sharply indicating that the whole sample including the $Nb/Pd_{95}Fe_5$ bilayer is superconducting. At higher currents this drop does not occur completely. Instead, it is intercepted by another peak coming into existence. This suggests, that a second region gets superconducting, thereby creating resistance by charge

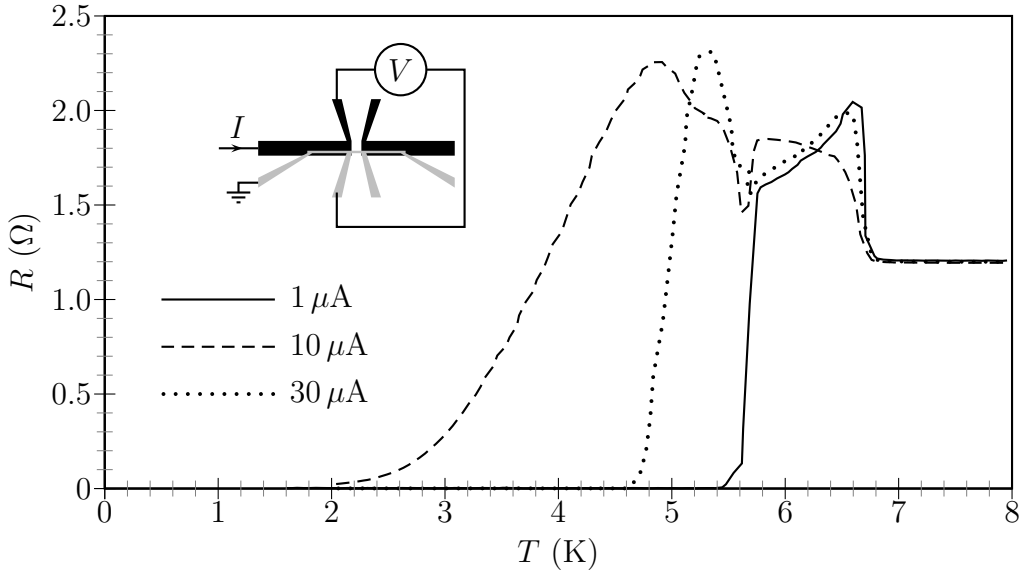

Figure 7.2: *Resistance depending on temperature of the sample 902C in nonlocal configuration. Lock-in technique was used at various excitation currents.*

imbalance effects. The typical behavior in this case is most prominently visible for the 30 μA curve, where the decay of resistance extends down to 2 K.

The image plots of the I–V characteristic depending on magnetic field and current were obtained in the measurement setup described in fig. 4.3c and section 4.2.3.

At 0° the picture is quite regular, but compared to the previous measurements it exhibits a double peak structure. This may be caused by the same beating which has been observed already, but here it has a much shorter period. Going to higher angles, one notices that the pattern gets increasingly more irregular. A representative picture is given for 10°. No periodicity can be found and sudden jumps of critical current occur.

As was discussed already, this might be explained by the creation of vortices, whose creation probability is much more probable at higher angles. They transport magnetic flux through the sample, which induces current. Their trapping and pinning may give rise to these irregularities. At even higher tilting angles, the irregular pattern is finer structured as is displayed here for 30°.

Jumps like the ones observed here abundantly, are not completely new. They were observed to a lesser degree also in other measurements not shown in this work. The irregular structures in the line scans at fixed current in sec. 5.5 are also attributed to this effect.

Measurements of differential resistance were also made for 0°. This can be compared to the direct measurement of the current-voltage characteristic by integration. Fig. 7.4 shows the result. The middle picture agrees very well with the right image, although between these measurements the sample was tilted and then readjusted. This yields the slight compression of the integration image compared to the direct measurement.

The image of differential resistance shows various lines around 23 μA, which also were mentioned in section 5.4.3. They correspond to dips in the differential resistance, which

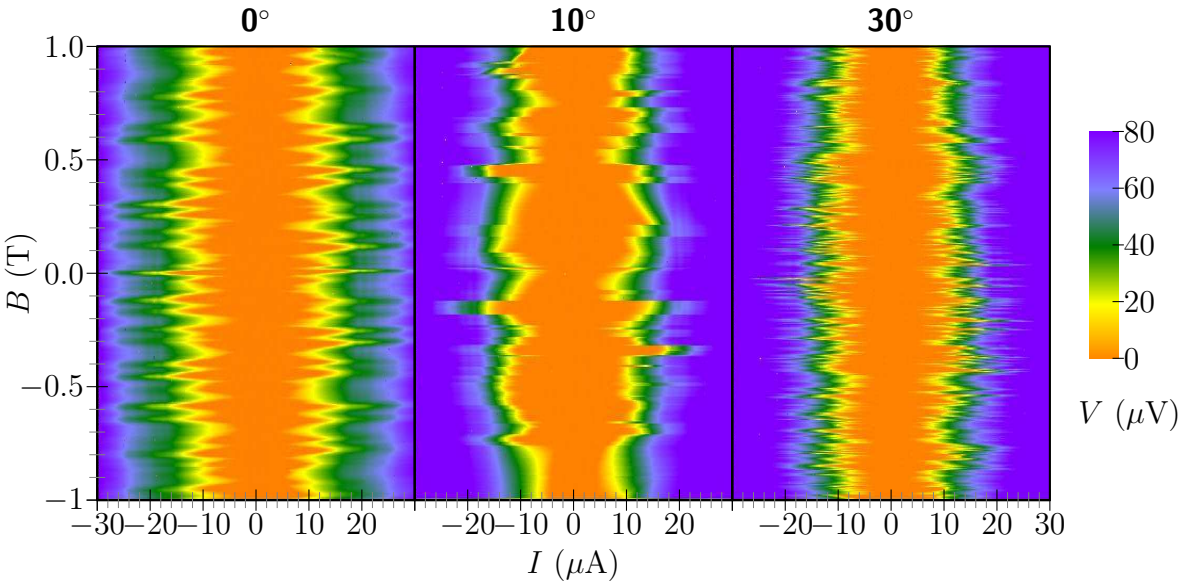

Figure 7.3: *Image plots of voltage depending on current and magnetic field at three representative angles. The contact configuration is given in fig. 7.2. The angles are the deviation of the magnetic field from the in-plane direction. The images display the absolute values of the voltage for reasons of contrast. On the left hand side of $I = 0\,\mu A$, all voltage values have to be considered negative.*

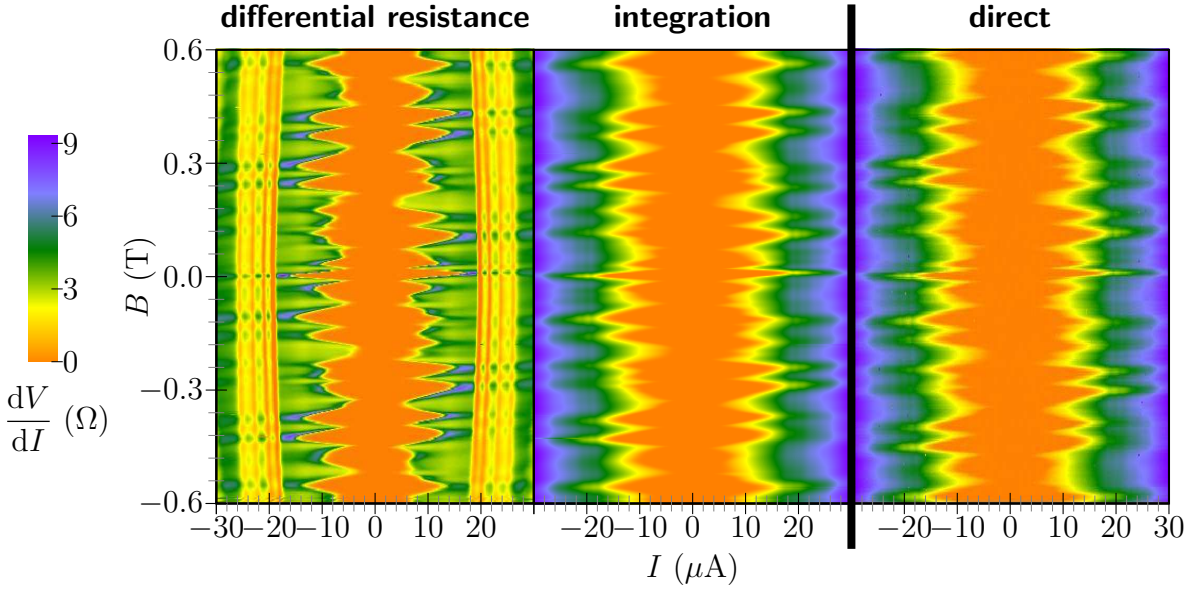

Figure 7.4: *Comparison of the plots obtained by integrating the differential resistance and by measuring the voltage directly. The magnetic field was in-plane, the temperature was 5 K, and the magnetic field was swept from negative to positive values. The color scale on the left hand side is for the differential resistance image and is truncated at 0 Ω. The scale for the voltages in the middle and right graph can be found in fig. 7.3.*

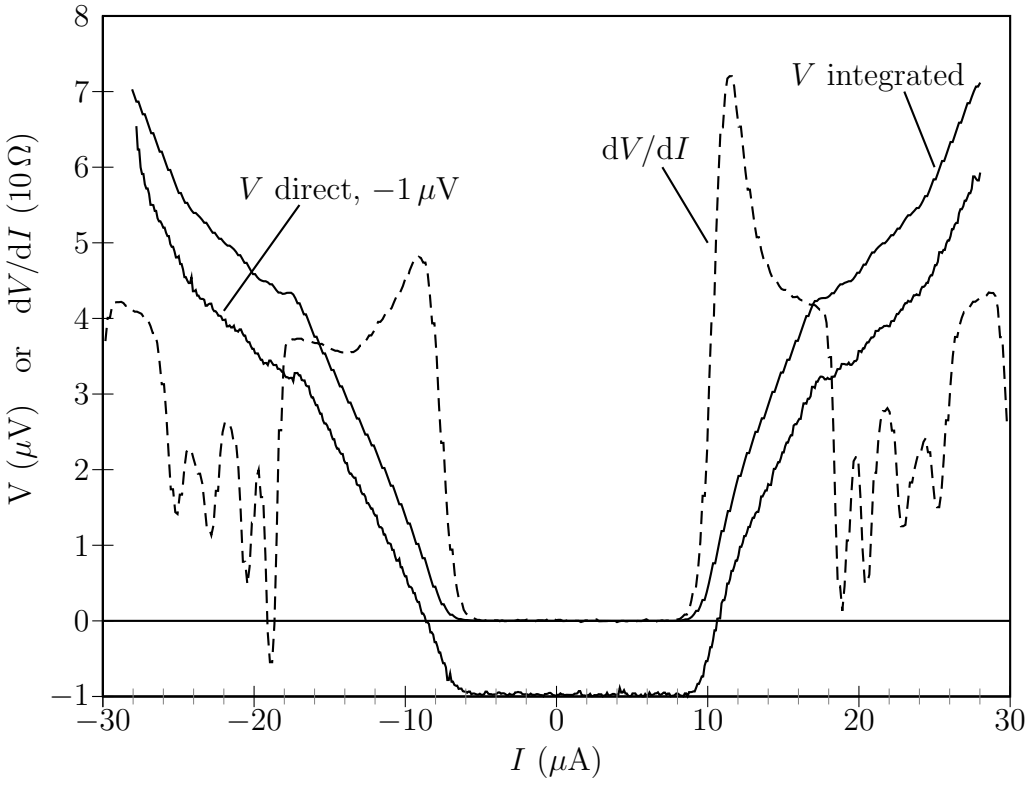

Figure 7.5: *Comparative plot of differential resistance and the integrated data taken at* $-312\,mT$ *from fig. 7.4. The corresponding curve for the direct measurement is given as a plot shifted by* $-1\,\mu V$*. Due to the slight tilting differences, it was found at* $-332\,mT$*. The parts of the voltage curves lying below* $0\,\mu A$ *have actually negative values.*

can also cross the zero resistance line and assume negative differential resistance at their minima. This is shown in fig. 7.5. They appear symmetrically about $I = 0\,\mu$A with just some minor deviations in the minimum values. In the integrated curve, the dips show up as small flattenings or steps.

The agreement between the curve obtained by integration of the differential resistance and the direct measurement is very good, except for currents below $25\,\mu$A. This deviation might be caused by the initialization process of the Accura oscilloscope. One should not forget, that a time span some days passed between those measurements and that the sample was tilted in between, so that the initial angle probably was not reached absolutely correctly again.

Although this sample's behavior is in detail quite different from previous measurements, it confirms that an interference pattern is created. The differences are probably due to slightly deviating geometries. Also interdiffusion of niobium and palladium-iron quite surely plays a role here, as this sample 902C was measured six months after 902A. This dependence of the behavior on time was seen also with the other samples, although not investigated systematically.

8 Summary, Conclusions And Perspective

This thesis was committed to the investigation of the electric properties of Nb/$Pd_{95}Fe_5$ hybrid structures.

The dilute ferromagnetic $Pd_{95}Fe_5$ thin films were deposited by simultaneous thermal evaporation of palladium and iron from separate Knudsen cells. This allowed to control the composition of the film.

The magnetization dependent anomalous Hall effect provided a characterization method for the magnetic properties of these films. Hall structures were prepared from the ferromagnetic material and placed at low temperatures in a cryostat. The temperature dependent Hall curves yielded information about the Curie temperatures, the normal Hall coefficients, and the square resistances for various iron concentrations. The temperature dependent magnetization and the hysteretic behavior were studied further in SQUID measurements, which affirmed the findings extracted from the Hall data.

To fabricate the superconductor/ferromagnet hybrid structures, thin layers of niobium were placed on top of $Pd_{95}Fe_5$ thin films. The PES technique was applied to ensure good quality of the niobium. This involved depositing and structuring a silicon nitride mask on top of a relatively thick PES layer. Isotropic plasma etching of the PES the formed a cavity under the openings of the mask down to a previously deposited $Pd_{95}Fe_5$ layer. In the following step, the underetch of the mask ensured that the niobium did not get into contact with the PES resist. Two types of samples were structured in this way: one with a ferromagnetic layer which was not contacted by external leads and one with additional probes at this layer.

Measurements of magnetoresistance by a lock-in technique in a sweeping magnetic field revealed distinct oscillations symmetric about $B = 0\,\mathrm{T}$. Two main periods could be identified. Close to $B = 0\,\mathrm{T}$ the symmetry was broken, as hysteretic peaks appeared. The distance of the peaks was in accordance with the hysteresis of the ferromagnetic layer. The superconducting nature of the niobium layer appeared in the vanishing of the oscillations towards higher temperatures. Regular oscillations were observed only if the magnetic field vector lay in the plane of the films, whereas in perpendicular orientation, they were irregular. Nevertheless, the same pattern could be reproduced by reversing the sweep direction of the magnetic field.

To gain more insight into the processes leading to the magnetoresistance oscillations, the differential resistance depending on current was measured at fixed magnetic field. The resulting data showed an asymmetry which did not depend on the sweep direction of the current. The form of the curves can be described as a valley of constant differential resistance flanked by peaks and outer regions of increased differential resistance.

The constant value enclosed by the peaks was attributed to the resistance of the $Pd_{95}Fe_5$ bridge. The width of the valley, likewise its shift relative to $I = 0\,\mu$A, changed at varying the magnetic field. The peaks flanking the valley, altered their height at changing the magnetic field. However, the peaks showed unequal height in one differential resistance measurement, being equally asymmetric like the location of the valley. The V-I characteristics obtained from the differential resistance data displayed a Josephson effect like behavior.

Plotting the color coded differential resistance in dependence of current and magnetic field resulted in a systematic pattern. At closer inspection, the pattern was found to be point symmetric about the point where $B = 0\,T$ and $I = 0\,\mu$A. By taking the differential resistance plots at various temperatures, the vanishing of the pattern close to the superconducting critical temperature of niobium could be proven. This hints at the effect being based on superconductivity, among other things. The investigation of the rim of the valley of constant differential resistance, which was equated with the critical current of the hybrid structure, showed that the periodicity did not change with temperature.

By measuring under the two sweep directions of the magnetic field, the hysteretic behavior of the central region around $B = 0\,$T was demonstrated. The compression of the pattern in this area could be linked to the switching of the magnetic moment of the $Pd_{95}Fe_5$ layer.

The magnetoresistance oscillations and the differential resistance pattern were observed with both sample designs. The samples with additional contacts on the ferromagnetic layer allowed the analysis of various contact configurations. One outcome was that the effect is not due to the ferromagnetic bridge in the structure, but to the part where the superconductor covers the $Pd_{95}Fe_5$ layer. Only contact configurations in which the current is forced to change from the superconductor to the ferromagnet, or reverse, were found to produce the oscillations and patterns. Especially the nonlocal contact configuration attracted attention, as here the current was able to flow partially without resistance, which points at supercurrent in the sample.

By tilting the sample in the magnetic field, the dependence of the periodicity on the magnetic flux was examined. The decrease of the periodicity was fitted by a formula involving the superconducting flux quantum and an active area. By this, the magnitude of the active area could be determined to lie in the range of the $Nb/Pd_{95}Fe_5$ bilayer. This is astonishing, as a SQUID structure could not be clearly identified in the sample.

Finally, two control experiments were performed. The first one comprised the sample design with fewer leads and a layer of pure palladium instead of $Pd_{95}Fe_5$. The differential resistance curves had a similar shape like in the previous measurements, but due to thermal effects, they were dependent on the current sweep direction. The periodic differential resistance pattern could not be observed here. Together with the $R(T)$ curves, it could be shown, that at the temperature of liquid helium the proximity effect in pure palladium has an extent of at least 200 nm. In the second experiment, a ferromagnetic layer was used again. By applying an alternative and faster measurement method, the differential resistance pattern with similar properties as in earlier samples was obtained again.

The oscillations and differential resistance patterns cannot clearly be attributed to quantum interference effects and to the Josephson effect, as the sample geometry does not allow this. Therefore, new sample designs are proposed. A continuous $Nb/Pd_{95}Fe_5$ bilayer could provide information about the critical current in this system. If superconductivity is suppressed significantly, then it gets more probable that a weak link exists also in the samples examined in this work. As a next step, it would be interesting to make a simple weak link structure, i. e. two superconducting banks separated by the bilayer, to see if the differential resistance or the I-V characteristic can be reproduced. Another emphasis could be placed on a possible nonlocal effect by moving the voltage probes in a similar nonlocal contact configuration, like used in this work, closer or farther away from the current path. As the flux through the sample has proven to be essential for the oscillation period, samples with different bilayer areas should be investigated. It might also be worthwhile to visualize the magnetic domains of the PdFe layer in a low temperature transmission electron microscope or by Hall magnetometry.

The complete picture of the results is quite complex and requires further study. Especially the asymmetry of the differential resistance seems to be an interesting question, whose answer might also explain many features seen in the color plots. If this is not a new effect, then at least an exciting new combination or variation of physical processes has been observed in this work.

A Detailed Recipe For Sample Preparation

Preparation Of The Substrate

- material: monocrystalline silicon substrate, p-doped with Boron, covered with 300 nm silicon dioxide
- coat with AR-P 3740, 1500 rpm, 30 s as protection layer
- cleave silicon substrate in 8 mm × 8 mm chips
- clean in an ultrasonic bath with acetone, flush with acetone and propanol, dry with nitrogen stream
- clean surface in soft oxide plasma, 2 minutes

Bond Pads And Rough Leads

- two layer PMMA resist, spinning parameters: 3000 rpm for 5 s (acceleration 0) and 8000 rpm for 30 s (acceleration 9), total thickness: 125 nm + 70 nm = 195 nm
  1. spin on PMMA 50 k 6 %
  2. bake on hot plate for 10 min at 150 °C
  3. spin on PMMA 950 k 2 %
  4. bake on hot plate for 6 min at 150 °C
- electron beam lithography (Topcon SM 510)
  1. rough leads and alignment marks: spot size 7, pixel spacing 10 nm, dose 240 μC/cm^2
  2. bond pads: spot size 11, pixel spacing 30 nm, dose 240 μC/cm^2
- developing: MIBK + propanol (1:3) for 1 min 30 s, flush in propanol for 1 min
- deposition of gold (UNIVEX)
  1. presputter with Argon at 2 kV
  2. evaporate 5 nm titanium (e-beam)
  3. evaporate 30 nm gold (crucible)
- lift-off in acetone

$Pd_{95}Fe_5$ Structures

- electron beam lithography
  1. spin on PMMA 950 k 4 %, parameters: 3000 rpm for 5 s (acceleration 0) and 8000 rpm for 30 s, acceleration 9; resulting thickness: 210 nm
  2. bake on hot plate for 6 min at 150 °C
  3. electron beam lithography (SEM LEO 1530): aperture 2, pixel spacing 5 nm, dose 220 μC/cm^2
  4. developing: MIBK + propanol (1:3) 1 min 35 s, propanol 1 min
- deposition of $Pd_{95}Fe_5$ (UHV, Knudsen cluster)
  1. insert sample in main chamber, close sample shutter
  2. turn effusion cell shutter to open palladium and iron cells
  3. heat up iron cell to 17 (value displayed at controller) and palladium cell to 12, heat up rate 0.3/min
  4. adjust iron rate to 0.1 Å/9 s (quartz set to iron parameters) by heating up more or cooling down
  5. control rate again after 5 min
  6. heat up palladium cell to an evaporation rate of 0.25 Å/s (palladium rate + iron rate measured with palladium settings at quartz)
  7. open sample shutter, evaporate 22.5 nm of $Pd_{95}Fe_5$
  8. close sample shutter
  9. cool down effusion cells, close effusion cell shutter
  10. take sample out of UHV system
- lift-off in acetone

For other iron concentrations see section 2.1.2.

Si_3Ni_4/PES Mask

Samples with a PES layer always must be stored dry (vacuum)!

- heat up hot plate to 275 °C. If deposition of Si_3N_4 follows immediately, also heat up PECVD to 275 °C
- PES layer (700 nm to 800 nm), Ultrason 2020 P
  1. dry resist spinner with nitrogen gas for 10 to 15 min, keep a reduced flow up during next steps, do not aim stream directly at sample
  2. put sample in resist spinner and cover completely with PES 20 % solution (syringe with particle filter 0.2 μm)
  3. spin with 3000 rpm for 300 s, acceleration 9 (parameters of the second step are all set to zero)

4. instantly put sample for 1 min on hot plate (275 °C)
5. put sample in vacuum or immediately continue with deposition of Si_3N_4 in PECVD (PES film and PES solution are hygroscopic)

- 60 nm silicon nitride layer (Oxford Plasmalab 80+ PECVD), deposition parameters: SiH_4 1000 sccm, NH_3 20 sccm, 20 W, 650 mTorr, 275 °C, 4 min

Nb Structures

- electron beam lithography (SEM LEO 1530)
  1. spin on PMMA 950 k 2 %, parameters: 3000 rpm for 5 s (acceleration 0) and 8000 rpm for 30s (acceleration 9), thickness 70 nm
  2. bake on hot plate for 6 min at 150 °
  3. electron beam lithography: aperture 2, pixel spacing 5 nm, dose 220 μC/cm^2
  4. developing: MIBK + propanol (1:3) 54 s, propanol 1 min
- reactive ion etching (Oxford Plasmalab 80+)
  1. Si_3N_4 layer, parameters: CHF_3 50 sccm, O_2 5 sccm, 30 mTorr, 150 W, 1 min
  2. undercut in PES layer, parameters: O_2 100 sccm, 300 mTorr, 100 W, 5 min
- deposition of niobium (UHV)
  1. cool the sample holder in the main chamber with liquid nitrogen to -30 °C
  2. argon sputtering (lock, Commonwealth Scientific IBS 250), parameters: discharge 40 V, beam current 5 mA, beam voltage 500 V, 20 s, 7.3×10^{-4} mbar
  3. deposition of 40 nm niobium (main chamber, electron beam evaporator), parameters: 210 mA, 1 Å/s
  4. stop cooling and let sample warm up to room temperature
- cleave the chip in 4 mm × 4 mm pieces, each with 4 structures
- lift-off in n-methyl-2-pyrollidone (NMP) at 60 °C, no ultrasonic bath!
- rinse in acetone and propanol

Addendum: Preparation Of The 20 % PES Solution

- dry 2 g of Ultrason E2020 P (BASF) flakes at 200 °C overnight
- dissolve flakes in 10 ml n-methyl-2-pyrollidone (NMP) at 60 °C agitating with magnetic stir bar (1 h or more), closed jar
- absorb with syringe
- attach particle filter (0.2 μm) and capped needle to syringe

Bibliography

[AH69] V. Ambegaokar and B. I. Halperin, *Voltage due to thermal noise in the dc Josephson effect*, PRL **22** (1969), 1364.

[AM76] N. W. Ashcroft and N. D. Mermin, *Solid state physics*, Thomson Learning, 1976.

[And64] A. F. Andreev, *The thermal conductivity of the intermediate state in superconductors*, Sov. Phys. JETP **19** (1964), 1228.

[BAS+92] C. Büscher, T. Auerswald, E. Scheer, A. Schröder, H. v. Löhneysen, and H. Claus, *Ferromagnetic transition in dilute Pd-Fe alloys*, Phys. Rev. B **46** (1992), no. 2, 983.

[Bau05] A. Bauer, *Spontaneous magnetic flux induced by ferromagnetic π-junctions*, Ph.D. thesis, Universität Regensburg, 2005.

[BCS57] J. Bardeen, L. N. Cooper, and J. R. Schrieffer, *Theory of superconductivity*, Phys. Rev. **108** (1957), 1175.

[Ben04] J. Bentner, *Zur Strom-Phasen-Relation diffusiver Supraleiter/Normalleiter/Supraleiter Josephson-Kontakte*, Ph.D. thesis, Universität Regensburg, 2004.

[Ber70] L. Berger, *Side-jump mechanism for the Hall effect of ferromagnets*, Phys. Rev. B **2** (1970), 4559.

[Blu01] S. Blundell, *Magnetism in condensed matter*, Oxford University Press, 2001.

[BP82] A. Barone and G. Paternò, *Physics and applications fo the josephson effect*, Whiley, New York, 1982.

[BVE01] F. S. Bergeret, A. F. Vokov, and K. B. Efetov, *Long-range proximity effects in superconductor-ferromagnet structures*, Phys. Rev. Lett. **86** (2001), 4096.

[BVE02] F. S. Bergeret, A. F. Volkov, and K. B. Efetov, *Local density of states in superconductor-strong ferromagnet structures*, Phys. Rev. B **65** (2002), 134505.

[BVE05] F. S. Bergeret, A. F. Vokov, and K. B. Efetov, *Odd triplet superconductivity and related phenomena in superconductor-ferromagnet structures*, Rev. Mod. Phys. **77** (2005), 1321.

[BWvL04] D. Beckmann, H. B. Weber, and H. v. Löhneysen, *Evidence for crossed Andreev reflection in superconductor-ferromagnet hybrid structures*, PRL **93** (2004), 1970031.

[Cla72] J. Clarke, *Experimental observation of pair-quasiparticle potential difference in nonequilibrium superconductors*, PRL **28** (1972), 1363.

[Coo56] L. N. Cooper, *Bound electron pairs in a degenerate electron gas*, Phys. Rev. **104** (1956), 1189.

[CW80] C. L. Chien and C. R. Westgate (eds.), *The Hall effect and its applications*, Plenum Press, New York and London, 1980.

[DCC+00] P. Dubos, P. Charlat, Th. Crozes, P. Paniez, and B. Pannetier, *Thermostable trilayer resist for niobium lift-off*, J. Vac. Sci. Technol. B **18** (2000), 122.

[GAB+03] W. Guichard, M. Aprili, O. Bourgeois, T. Kontos, J. Lesueur, and P. Gandit, *Phase sensitive experiments in ferromagnetic-based josephson junctions*, Phys. Rev. Lett **90** (2003), 167001.

[GL50] V. L. Ginzburg and L. D. Landau, Zh. Eksp. Teor. Fiz. **20** (1950), 1064.

[Gor59] L. P. Gor'kov, *Microscopic derivation of the Ginzburg-Landau equations on the theory of superconductivity*, Sov. Phys. JETP **9** (1959), 1364.

[Gra81] K. E. Gray (ed.), *Nonequilibrium superconductivity, phonons, and Kapitza boundaries*, ch. 13, Plenum Press, New York and London, 1981.

[HPT74] G. L. Harding, A. B. Pippard, and J. R. Tomlinson, *Resistance of superconducting-normal interfaces*, Proc. R. Soc. Lond. **A340** (1974), 1.

[HSSS02] T. Hoss, C. Strunk, C. Sürgers, and C. Schönenberger, *UHV compatible nanostructuring technique for mesoscopic hybrid devices: application to superconductor/ferromagnet Josephson contacts*, Physica E **14** (2002), 341.

[Jos62] B. D. Josephson, *Possible new effects in superconductive tunneling*, Phys. Lett. **1** (1962), 251.

[Jos65] ———, *Supercurrents through barriers*, Adv. Phys. **14** (1965), 419.

[JS85] M. Johnson and R. H. Silsbee, *Interfacial charge spin coupling: Injection and detection of spin magnetization in metals*, Phys. Rev. Lett. **55** (1985), 1790.

[KAL+02] T. Kontos, M. Aprili, J. Lesueur, F. Genet, B. Stephanidis, and R. Boursier, *Josephson junction through a thin ferromagnetic layer: Negative coupling*, Phys. Rev. Lett **89** (2002), 137007.

[Kas56] Tadao Kasuya, *A theory of metallic ferro- and antiferromagnetism on Zener's model*, Prog. Theor. Phys. **16** (1956), 45.

[KGK+06] R. S. Keizer, S. T. B. Goennenwein, T. M. Klapwijk, G. Miao, G. Xiao, and A. Gupta, *A spin triplet supercurrent through the half-metallic ferromagnet $Cr0_2$*, Nature **439** (2006), 825.

[Kim66] D.-J. Kim, *Ferromagnetism in dilute alloys*, Phys. Rev **149** (1966), 434.

[Kit07] M. Kitzinger, *Der magnetische Phasenübergang von verdünnten Eisen-Palladium-Legierungen in Abhängigkeit von der Schichtdicke*, Master's thesis, Universität Regensburg, 2007.

[Kog82] V. G. Kogan, *Coherence length of a normal metal in a proximity system*, Phys. Rev. B **26** (1982), 88.

[Kon02] T. Kontos, *Cohérence et interférences quantiques dans des nanostructures supraconducteur/ferromagnetique*, Ph.D. thesis, Université Paris XI UFR Scientifique d'Orsay, 1 2002.

[Kun86] H.-J. Kunze, *Physikalische Meßmethoden*, Teubner Stuttgart, 1986.

[Lév00] L.-P. Lévy, *Magnetism and superconductivity*, Springer-Verlag Berlin Heidelberg, 2000.

[MGK96] M. Mahel', M. Grajcar, and P. Kúš, *Supravodivosť*, Univerzita Koneského Bratislava, 1996.

[MT94] R. Meservey and P. M. Tedrow, *Spin-polarized electron tunnelinig*, Phys. Rep. **238** (1994), 173.

[Nie75] G. J. Nieuwenhuys, *Magnetic behaviour of cobalt, iron and manganese dissolved in palladium*, Adv. Phys. **24** (1975), 515.

[Ohn98] H. Ohno, *Making nonmagnetic semiconductors ferromagnetic*, Science **281** (1998), 951.

[Pla66] H. Plate, *Die Temperaturabhängigkeit des Halleffektes von Palladium und Silber und ihre Beeinflussung durch Zusatzmetalle im Temperaturbereich von 50° bis 300° K*, Phys. kondens. Mater. **4** (1966), 355.

[PLP69] O. A. Panchenko, P. P. Lutsiskin, and Yu. G. Ptushinskij, *Galvanometric effects in thin films of some transition metals*, Soviet Phys. JETP **29** (1969), 76.

[RK54] M. A. Ruderman and C. Kittel, *Indirect exchange coupling of nuclear magnetic moments by conduction electrons*, Phys. Rev. **96** (1954), 99.

[ROR+01] V. V. Ryazanov, V. A. Oboznov, A. Yu. Rusanov, A. V. Veretennikov, A. A. Golubov, and J. Aarts, *Coupling of two superconductors through a ferromagnet: Evidence for a π junction*, Phys. Rev. Lett. **86** (2001), 2427.

[Smi55] J. Smit, *The spontaneous Hall effect in ferromagnetics I*, Physica **21** (1955), 877.

[Smi58] ———, *The spontaneous Hall effect in ferromagnetics II*, Physica **24** (1958), 39.

[SS75] A. Schmid and G. Schön, *Linearized kinetic equations and relaxation processes of a superconductor near T_C*, J. Low. Temp. Phys **20** (1975), 207.

[SSvL00] M. Schöck, C. Sürgers, and H. v. Löhneysen, *Superconducting and magnetic properties of $Nb/Pd_{1-x}Fe_x/Nb$ triple layers*, Eur. Phys. J. B **14** (2000), 1.

[Sto38] E. C. Stoner, *Collective electron ferromagnetism*, Proc. R. Soc. **A165** (1938), 372.

[Tin96] M. Tinkham, *Introduction to superconductivity*, 2nd ed., McGraw-Hill, Inc., 1996.

[TM71] P. M. Tedrow and R. Meservey, *Spin-dependent tunneling into ferromagnetic nickel*, Phys. Rev. Lett. **26** (1971), 192.

[TM73] ———, *Spin polarization of electrons tunneling from films of fe, co, ni, and gd*, Phys. Rev. B **7** (1973), 318.

[Yos57] Kei Yosida, *Magnetic properties of Cu-Mn alloys*, Phys. Rev. **106** (1957), 893.

Dank

Viele Menschen haben zum Gelingen dieser Doktorarbeit beigetragen. Ich nutze die Gelegenheit, um sie hier einmal alle zu erwähnen.

Ich bedanke mich herzlich bei *Prof. Dr. Christoph Strunk* für sein großes Interesse an meiner Doktorarbeit und den Antrieb, den er mir immer wieder gegeben hat.

Martin Furtmeier, unser technischer Zauberer, hat mich und alle anderen Kollegen bei Problemen und Problemchen unterstützt. Die Sachen waren oft fast schon fertig, bevor man auch nur daran gedacht hatte, sie zu benötigen. Vielen Dank!

Den Herren *Karl Weigert* und *Lothar Rother* und ihren Nachfolgern *Christian Haimerl* und *Thomas Solleder* sage ich Dank für den steten Nachschub an flüssigem Helium und auch die eine oder andere Notkanne. Die kleinen Plaudereien in der Heliumausgabe möchte ich nicht missen.

Matthias Sperl und *Monika Kitzinger* bin ich dankbar, dass sie mit ihren Messungen meine Dünnschichtcharakterisierungen hervorragend ergänzten.

Dr. Ondrej Vavra hatte am Ende meiner Doktorarbeit immer ein offenes Ohr für Fragen und stand mir für Diskussionen bereitwillig zur Verfügung. Ich danke ihm und wünsche ihm viel Erfolg bei der Fortsetzung meiner Arbeit.

Das Doktorandenleben wäre doch ziemlich einsam, hätte man nicht Bürokollegen. *Dr. Bernhard Stojetz* und *Florian Otto* gebührt mein Dank für Gespräche über Physik und über Menschliches und für den ein oder anderen Spaß. Besonders danke ich auch den „Urmitgliedern" der Arbeitsgruppe, den *Dres. Bernhard Stojetz, Johannes Bentner und Andreas Bauer*, dass sie mir den Start in die Reinraumarbeit und an den Anlagen erleichtert haben.

Franziska Rohlfing danke ich besonders. Die kleineren und größeren Wehwehchen, die einem Doktoranden nun mal hin und wieder plagen aber auch Erfolge haben wir miteinander geteilt. Dein Ostriesentee vom Bremer Teekontor hat für so manch entspannendes Stündchen gesorgt.

Allen Mitgliedern der Arbeitsgruppen Strunk und Weiss danke ich für die Unterstützung bei fachlichen Fragen und für die Hilfen im Reinraum und den anderen Labors. Es herrschte stets eine gute Atmosphäre am Lehrstuhl.

Der allergrößte Dank gebührt *meinen Eltern*. Sie haben mich immer unterstützt und zu mir gehalten.

Diese Arbeit wurde von der DFG im Rahmen des Sonderforschungsbereichs 631 untersttützt.